

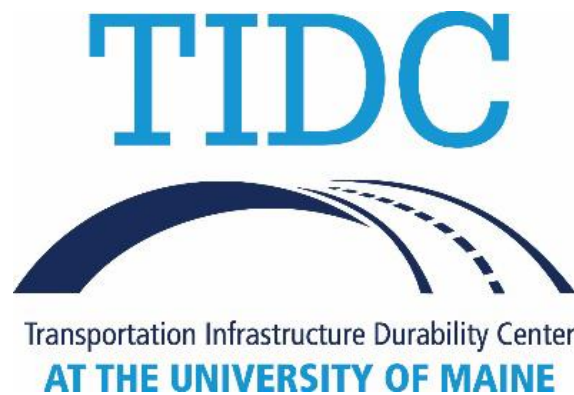
Testing, Monitoring, and Analysis of FRP Girder Bridge with Concrete Deck

Final Project Report

06/30/2021

Andrew Schanck EI, MS
Research Engineer & PhD Candidate, University of Maine Civil Engineering

William Davids PhD, PE
Professor of Civil and Environmental Engineering, University of Maine



ACKNOWLEDGEMENTS

Support for this research was provided by the Transportation Infrastructure Durability Center (TIDC) at the University of Maine under grant 69A3551847101 from the U.S. Department of Transportation's University Transportation Centers Program. Additional financial and logistical support was provided by the Maine Department of Transportation and AIT Bridges, whose assistance is greatly appreciated. The results and opinions reported here are solely those of the authors and do not constitute a design guide or specification.

DISCLAIMER

The contents of this report reflect the views of the authors, who are responsible for the facts and the accuracy of the information presented herein. This document is disseminated in the interest of information exchange. The report is funded, partially or entirely, by a grant from the U.S. Department of Transportation's University Transportation Centers Program. However, the U.S. Government assumes no liability for the contents or use thereof.

Table of Contents

Index of Figures	3
Index of Tables	4
1 Introduction	6
2 Observations of Manufacture and Construction	7
2.1 <i>Introduction</i>	7
2.2 <i>Girder Manufacturing</i>	7
2.3 <i>Bridge Construction</i>	14
2.4 <i>Encountered Challenges and Proposed Solutions</i>	17
3 Non-Destructive Live-Load Testing	20
3.1 <i>Introduction</i>	20
3.2 <i>Loading</i>	20
3.3 <i>Instrumentation</i>	22
3.4 <i>Results</i>	24
3.5 <i>Analysis of Test Data and Girder Behavior</i>	27
4 Finite Element Analysis	38
4.1 <i>Introduction</i>	38
4.2 <i>Modeling</i>	38
4.3 <i>Model Calibration</i>	41
4.4 <i>Results</i>	48
4.5 <i>Behavior Inferred from FE Models</i>	53
5 Conclusions	55
6 References	57
A.1 Live-Load Test Strain Histories	59
A.1.1 <i>SBS_2_1</i>	59
A.1.2 <i>SBS_2_2</i>	64
A.1.3 <i>MAX_1_1</i>	69
A.1.4 <i>MAX_2_1</i>	74
A.1.5 <i>MAX_2_2</i>	79
A.1.6 <i>MAX_3_1</i>	84
A.1.7 <i>ALT_2_1</i>	89
A.2 Concrete Cylinder Test Reports from the Hampden Grist Mill Bridge Deck Pour	94

Index of Figures

Figure 1: Test Panel Infusion to Calibrate Part Wet-out (Left: Panel Top; Right; Panel Bottom).	8
Figure 2: Male Mock-Up Girder Mold	9
Figure 3: Infusion of Initial Girder Mock-Up on Male Mold.....	9

Figure 4: Full-Size Female Girder Mold	10
Figure 5: Second Girder Mock-up under Vacuum Consolidation	11
Figure 6: Infused, Cured Second Girder Mock-Up	11
Figure 7: Layup of Girder Reinforcement in Process	12
Figure 8: Consolidated Girder with Flow Media and Vacuum/Resin Feed Lines Visible	13
Figure 9: Infusion of Resin into Vacuum Consolidated Reinforcement.....	13
Figure 10: Demonstration of Girder Post-Processing.....	14
Figure 11: Girders Arriving at Bridge Site	15
Figure 12: Utility Hangers (Left: Installation; Right: In Place).....	15
Figure 13: Two-Girder Unit Being Lifted into Place.....	15
Figure 14: Girder Ends Placed on Bearing Pads.....	16
Figure 15: Reinforced Concrete Deck Pour.....	17
Figure 16: Right: Minor “Dry Spot” Surface Imperfection Left: Secondary Repair Infusion	18
Figure 17: Debulked Structural Defect	19
Figure 18: Repair of Structural Defect: Left: Removal of Affected Laminae, Center: Layup of New Fabric, Right: Re-Infusion	19
Figure 19: Wheeler Type Dump Trucks Used for Loading.....	21
Figure 20: Aerial Photo of MAX_1_1 Test (Courtesy of Advanced Infrastructure Technologies)	22
Figure 21: Strain Transducer Mounted to the Bottom Flange of a Girder.....	23
Figure 22: BDI STS-Wi-Fi Network Setup	23
Figure 23: Midspan Sensor Arrangement	24
Figure 24: Plan View of Sensor Layout.....	24
Figure 25: As-designed Girder Ends with Approach Slab.....	29
Figure 26: End-to-Midspan Strain Ratios – East End.....	31
Figure 27: End-to-Midspan Strain Ratios – West End	32
Figure 28: Comparison of predicted and Measured Deflections	35
Figure 29: Meshed FE Model	39
Figure 30: Mesh Refinement Convergence Study	40
Figure 31: FE Predicted Minor Rotational Restraint from Backwall	41
Figure 32: Locations of Spring Elements – Bottom View.....	43
Figure 33: Locations of Spring Elements – Side View.....	43
Figure 34: Error in Strain Prediction with Single, Discrete Type 1 Spring Elements	45
Figure 35: Error in Strain Prediction with Equal, Paired, Discrete Spring Elements.....	46
Figure 36: Error in Strain Prediction with Distributed Spring Elements.....	47

Index of Tables

Table 1: Explanation of Test Series	21
---	----

Table 2: Comparison of Initial and Updated Flexural RFs.....	26
Table 3: Comparison of Theoretical and Inferred Neutral Axis Heights.....	28
Table 4: Comparison of Measured and Restraint-Corrected Mid-Span Strain.....	33
Table 5: Extreme Tension Fiber Flexural Rigidities.....	34
Table 6: Comparison of AASHTO DFs and Test Computed GLFs	37
Table 7: Description of Restraining Spring Elements	44
Table 8: Comparison of Measured, Un-calibrated, and Calibrated Strains – SBS_2_1	49
Table 9: Comparison of Measured, Un-calibrated, and Calibrated Strains – SBS_2_2.....	49
Table 10: Comparison of Measured, Un-calibrated, and Calibrated Strains – MAX_1_1.....	50
Table 11: Comparison of Measured, Un-calibrated, and Calibrated Strains – MAX_2_1.....	50
Table 12: Comparison of Measured, Un-calibrated, and Calibrated Strains – MAX_2_2.....	51
Table 13: Comparison of Measured, Un-calibrated, and Calibrated Strains – MAX_3_1.....	51
Table 14: Comparison of Measured, Un-calibrated, and Calibrated Strains – ALT_2_1	52
Table 15: Summary of Error in FE Predicted Strains	52
Table 16: FE Predicted Neutral Axis Heights.....	53
Table 17: Effect of Reducing Wearing Surface Stiffness on Neutral Axis Heights.....	54
Table 18: FE Predicted Midspan Deflection.....	54
Table 19: FE Predicted GLFs	55

1 Introduction

The Hampden Grist Mill Bridge (HGMB) – Maine Department of Transportation bridge number 2334 - is a 75 ft simple-span bridge in Hampden, Maine carrying U.S. Rte. 1A/Maine Rte. 9 across Souadabscook Stream. As part of a larger project to reconstruct U.S. 1A between mid-2019 and mid-2021, an existing reinforced concrete T-beam bridge was removed and replaced with a new structure, which is the first in the United States to use the fiber reinforced polymer (FRP) composite tub (CT) girders developed by the University of Maine (UMaine) as its main structural members. This type of girder was developed by UMaine [1,2] as an alternative to medium span girders made from steel or concrete. Relative to these conventional materials, CT girders are light, easily transported, and highly durable.

Owing to the novelty of the CT girder system and limited previous full-scale testing [1, 2], more information on its in-service performance is desired. Although basic mechanics principals, design guidance for conventional materials [3], and design guidance for other FRP components [4, 5] allowed a reasonable, conservative design to be produced, the system's actual behavior and the accuracy of the assumptions made remained uncertain. Due to its hand in the development of the CT girder system and experience in the spheres of research of FRP materials and bridge live-load behavior, UMaine was enlisted to help fill the knowledge gap between design and reality, and inform the design, manufacture, and construction of future bridges.

Four main tasks were given to UMaine to help improve understanding of the CT girder system in general and the HGMB in particular. First, UMaine facilitated the bridge's design using advanced numerical modeling of shear stress distribution, lateral-torsional buckling during construction, and effects of impact loading. This task was the subject of a previous project and will not be discussed here further. Once the final design of the HGMB had been approved, the second task began. From first tests of CT girder manufacturing procedures to pouring of the bridge's main deck, manufacture and construction of the HGMB's superstructure was observed and documented. This served the purpose of informing subsequent tasks of the superstructure's structural history, and allowed the challenges encountered and their proposed solutions to be documented to inform the design and construction of future structures.

Once substantial construction of the HGMB had been completed and in parallel with readiness for bridge opening, the third of UMaine's tasks was conducted. Non-destructive live-load testing (NDLLT) was conducted on the HGMB in its near-virgin state under a high level of service loading. Four overloaded dump trucks were driven onto the bridge and positioned at several critical locations while the bridge's longitudinal strain response was simultaneously measured. The data collected during this testing was used to assess the bridge's actual stiffness and live-load distribution for comparison with original design assumptions, to update its capacity rating factor based on its actual response relative to theory, and as a benchmark for future behavior predictions, including those made as part of task 4. Task 4 itself involved creating high-fidelity, linear finite element (FE) models of the HGMB, calibrating them based on the results of NDLLT, and using

them to further understanding of the bridge and CT girder system's service-level behavior. The results of these tasks were intended to be used to help avoid future challenges in design and construction, optimize design, inform future investigation, and increase knowledge of the structural behavior of this promising structural system.

This report is organized into five sections including this introductory section and four additional sections describing testing, analysis and broader conclusions. These are:

- Section 2: Observations of the manufacture and construction of the HGMB
- Section 3: Non-destructive live-load testing of the HGMB and analysis of the results
- Section 4: Finite element modeling and analysis of the HGMB load tests
- Section 5: Conclusions drawn

Relevant calculations, data, and external contractor's reports are provided in appendices, which are preceded by a short list of references.

2 Observations of Manufacture and Construction

2.1 Introduction

As was mentioned above, the HGMB is the first of its kind, and as such there was very little available information and experience upon which to base its design, manufacture, and construction. This meant that, along with being a test case for behavior and efficacy once constructed, the HGMB was also an experiment in manufacture and construction of CT girder bridges. For this reason, periodic observations were made from the time of first trial resin infusions through laying the initial, temporary wearing surface – any manufacturing and construction activity relating to the bridge's superstructure. These observations, and continued communication with the designer/manufacturer revealed a number of unpredicted challenges and proposed or implemented solutions.

2.2 Girder Manufacturing

The HGMB's girders were designed and manufactured by AIT Bridges, a division of Advanced Infrastructure Technologies (who will from now on be referred to simply as "AIT"). Although AIT has significant experience with FRP composites for infrastructure applications, manufacturing the CT girder represented a significant advancement of its capabilities. For this reason, and due to some of the challenges it faced as discussed later, manufacture tended to proceed at a cautious pace, with numerous tests and mock-ups made for proofs-of-concept. These proofs-of-concept, while slowing the manufacture process, allowed many of the unforeseen difficulties to be discovered beforehand, rather than being incorporated into the full-scale product.

Initial test infusions and mock-ups were made at a temporary work-space in Bangor, Maine in early 2019. These first trials were conducted primarily to calibrate resin properties in order to

tailor them for manufacture. Specifically, the resin's viscosity was tuned to ensure full part wet-out before gelation with minimal resin waste. Figure 1 shows a test panel infusion in process, with contours drawn on the top of the vacuum bag and on the bottom of the glass infusion table to indicate resin flow-front at certain elapsed times after initiation of infusion. Infusion of similar test panels had the additional benefit of allowing test coupons to be collected, from which the layup's mechanical properties could be verified.



Figure 1: Test Panel Infusion to Calibrate Part Wet-out (Left: Panel Top; Right: Panel Bottom)

In addition to the initial test panels, a small-scale mock-up of the full girder was laid-up, consolidated, and infused, again to verify assumptions of part wet-out time and gain experience before manufacturing full girders. This initial mock-up infusion was again performed in the temporary Bangor facility in April 2019. For this mock-up, a male mold was used, as seen in Figure 2. Infusion of the mock-up, a 6 ft section of girder, can be seen in Figure 3. The use of a male mold greatly facilitated layup, with mold sides easily accessible. Unfortunately the outside of the part (the side that would be visible on the full-scale girders) developed unsightly wrinkling on transition radii and a generally poor surface finish as compared with the inside surface which was laid directly on the mold. The radial wrinkling can be seen in Figure 3 at the transition between bottom flange and web. For this reason, all future mock-ups and the actual girders were laid up onto a female mold.



Figure 2: Male Mock-Up Girder Mold

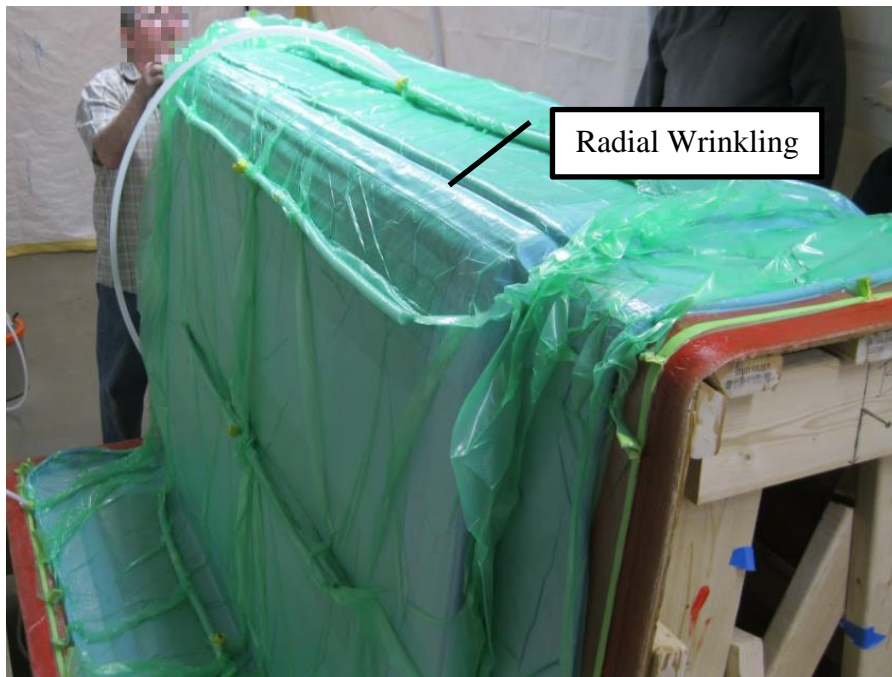


Figure 3: Infusion of Initial Girder Mock-Up on Male Mold

After the initial test infusions and small-scale mock-up, production was moved to AIT's permanent production facility in Brewer, Maine. There, a full-size female mold, seen in Figure 4 was constructed, faired, and seasoned before a second small-scale mock-up girder was infused. The second mockup, much like the first, consisted of a 6 ft section of full girder layup. For this mock-up, a HDPE caul plate was applied to one of the top flange to web transition radii, intended

to help prevent the radial wrinkling seen in the first mock-up infusion. In addition, the remainder of the mold was laid up with a very thin layer of glass for a resin-rich seasoning infusion. The mock-up under vacuum consolidation and caul plate can be seen in Figure 5, with the finished mock-up seen in Figure 6.



Figure 4: Full-Size Female Girder Mold

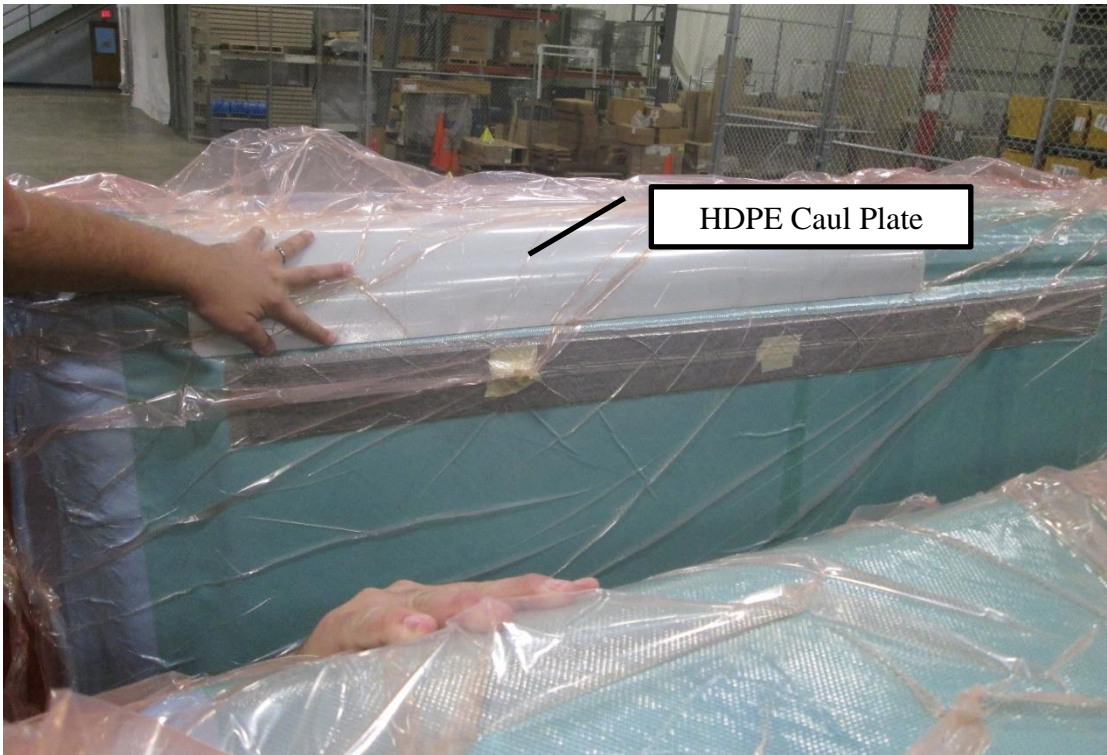


Figure 5: Second Girder Mock-up under Vacuum Consolidation



Figure 6: Infused, Cured Second Girder Mock-Up

Once mock-ups had been infused and the mold repaired (as discussed later), layup and infusion of the full, final girders commenced. In general, the workflow for manufacturing a girder was as follows:

1. Prepare mold by repairing any defects from the previous infusion, and apply wax and release agents
2. Place reinforcement into the mold according to the lay-up schedule using spray adhesives to temporarily tack them in place (Figure 7)
3. Install infusion consumables (resin feed lines, vacuum lines, flow improvement media, vacuum consolidation bagging, etc.) (Figure 8)
4. Consolidate part by drawing high vacuum pressure beneath the vacuum bag
5. Infuse the consolidated part with initiated, catalyzed resin and allow to cure (Figure 9)
6. Remove the cured part from the mold and perform post-processing (Figure 10)



Figure 7: Layup of Girder Reinforcement in Process



Figure 8: Consolidated Girder with Flow Media and Vacuum/Resin Feed Lines Visible

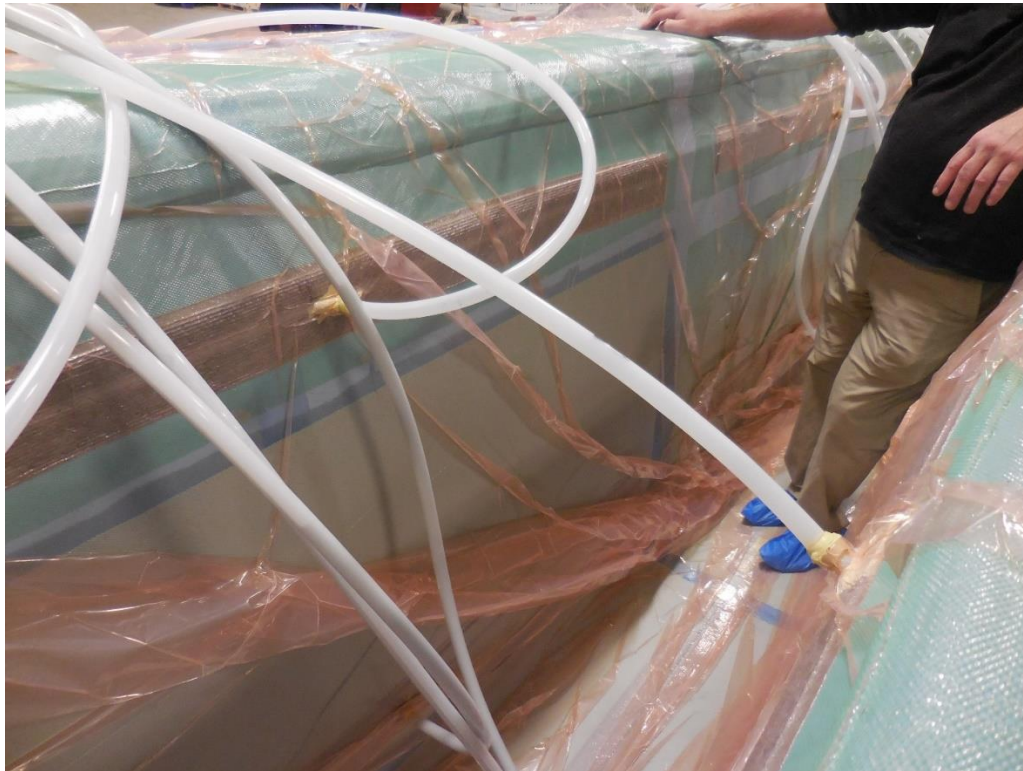


Figure 9: Infusion of Resin into Vacuum Consolidated Reinforcement

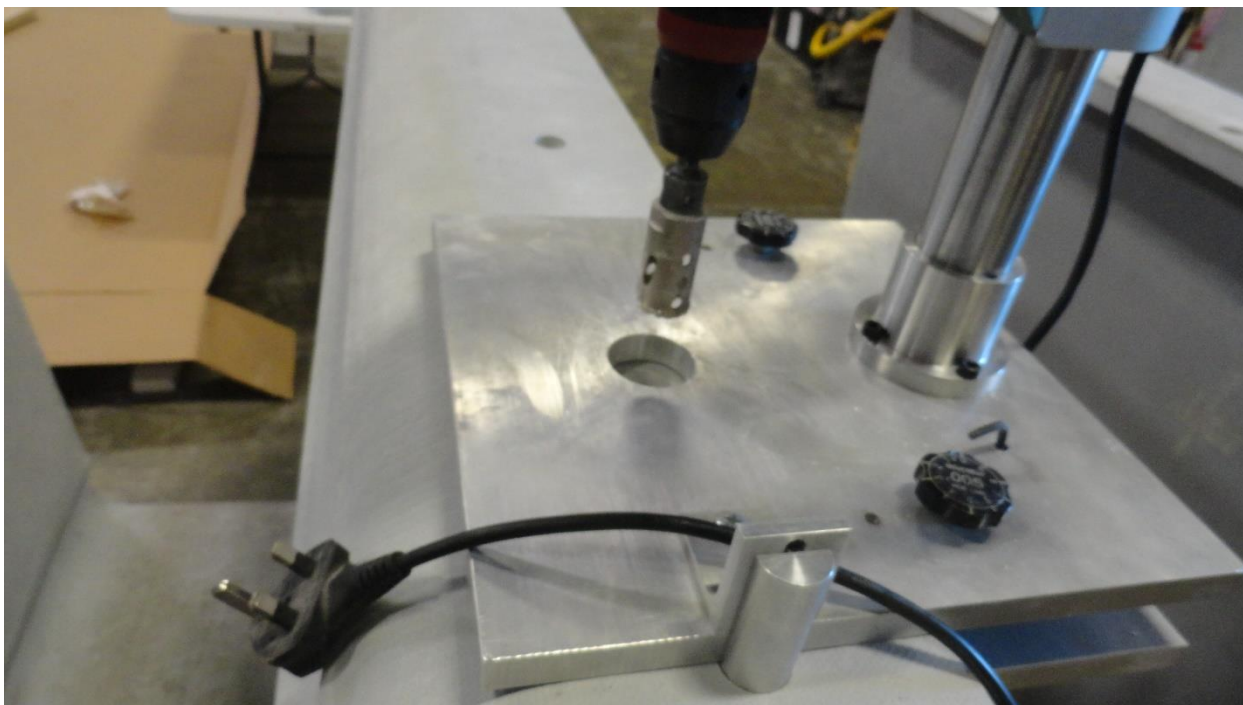


Figure 10: Demonstration of Girder Post-Processing

From mold preparation to final post-processing, each girder took approximately one month to fully manufacture, not including additional time for repair of damages and defects. However, from the first to the fifth girder, processing time and delays tended to decrease due to increasing experience, and girder fabrication is now much faster.

2.3 Bridge Construction

Replacement of the original HGMB began in early spring of 2020. However, due to numerous factors, chief among them the onset of the COVID-19 global pandemic, the project was delayed many times. In fact, whereas bridge opening had initially been scheduled for late summer or early autumn of 2020, traffic was not allowed to cross the replaced bridge until December 24, 2020. However, these delays tended not to result from the construction of the bridge's superstructure, nor as a result of using CT girders.

After the original structure had been removed, the site-work completed, and the substructure constructed, the superstructure construction commenced. The five CT girders were transported from AIT to the site on November 5, 2020 and placed November 5 and 6, 2020. Figure 11 shows the first two girders being delivered to the site by extended flatbed truck. Transport of multiple CT girders at a time exemplifies one of the advantages of CT girders over comparable prestressed concrete girders for which they are designed to compete. Once arrived, girders were lifted from the truck and placed on temporary supports for staging and preparation work. Where present, utility hangers were installed while girders were staged which spanned between girders transversely and from which utilities (municipal water and sewer lines) were hung. The fact that

two girders could be placed at a time with a single crane is a direct benefit of their light weight, and also simplified utility installation. This process and the resulting hanger system can be seen in Figure 12. Girders were then lifted into place by crane, with hanger-connected girders being lifted together as a unit. This can be seen in Figure 13, with girder ends sitting on bearings in Figure 14.



Figure 11: Girders Arriving at Bridge Site



Figure 12: Utility Hangers (Left: Installation; Right: In Place)



Figure 13: Two-Girder Unit Being Lifted into Place



Figure 14: Girder Ends Placed on Bearing Pads

After girder placement, the concrete elements of the bridge were formed, reinforced, and cast. In general, the concrete used was a standard DOT mix with nominal compressive strength of 4 ksi and was reinforced with ASTM A955 stainless reinforcing bar. Three separate concrete pours were carried out, with construction joints at the interface and reinforcing bars providing dowel action. First, the backwalls were poured which encased the ends of the girders and against which the roadway base was backfilled once sufficiently cured. After this, the bridge's deck was formed and poured. This pour took place December 8, 2020, with concrete placed by pump truck as seen in Figure 15. Due to the cold temperature experienced during the pour and predicted freeze-thaw cycling over the deck's lifetime, air entraining admixtures were incorporated which raised the air entrainment to about 8.5%. Finally, during the final pour, the bridge's curbs and sidewalks were cast. Once all concrete elements had cured sufficiently, a temporary asphalt wearing surface was laid, which was subsequently replaced with a permanent wearing surface the following spring.



Figure 15: Reinforced Concrete Deck Pour

2.4 Encountered Challenges and Proposed Solutions

With any prototype structure, the use of new materials, designs, or construction techniques reveal new, unforeseen challenges, which require solutions to be proposed and implemented. The HGMB is no exception. Through the girder manufacture process and bridge construction, a number of challenges arose and required immediate solutions for progress to continue. In general, the challenges associated with the novelty of the CT girder bridge system were encountered during manufacture of the girders themselves and resulted from general inexperience and lack of adequate personnel training and quality assurance.

The first major challenge arising from girder manufacture was touched upon previously. The original plans for the CT girder system called for construction of a male mold onto which fabric reinforcement would be laid and parts infused. This plan persisted until after infusion of the first mock-up part, again seen in Figure 3. The relatively tight transition radii between top flange and webs and webs and bottom flange caused reinforcement to either bunch or overstretch which, when vacuum was pulled, caused wrinkling (again seen in Figure 3). This wrinkling was not a structural concern and persisted into the final girders. On the contrary, the wrinkles were determined to be an aesthetic and public confidence concern. The use of a male mold caused these wrinkles to form on the part's exterior and thus visible from beneath the final structure. This would not only prove unsightly, but also may have reduced the public's confidence in the system, although such a lack of confidence would have been unfounded.

To improve the girders' visible finishes after construction, it was decided to transition from using a male mold to using a female mold. This put the mold finish side of the part – the side that conformed to the smooth surface of the mold – on the outside, with the inside, non-visible side

face taking surface imperfections and wrinkling. This solved the problem of poor surface finish, but led to additional manufacturing difficulties. When using the male mold, all portions of the girder were easily accessible from either side of the mold without the need to step onto the mold itself. On the contrary, nearly all operations performed when using a female mold required stepping into the mold itself and thus required stringent cleanliness procedures and heightened spatial awareness to prevent contamination and damage to the part, mold, and vacuum bag. This also slowed the already laborious lay-up and bagging process by limiting the number of workers able to participate at any one time and by limiting their mobility. As the mold for the HGMB's girders represented a significant investment in time and resources to construct and considering that the mold would not be used again after, it was not justifiable to develop a method to improve part surface finish and construct a new, full-size male mold. However, if additional bridges of a similar type are to be built, a method allowing use of a male mold, or more efficient manufacturing procedures with a female mold should be developed.

After infusion and curing, inspection of each of the girders revealed imperfections and defects requiring remedial actions to be taken. Most of these imperfections were minor and aesthetic in nature, requiring straightforward repairs. These minor imperfections consisted mainly of small areas of incomplete resin wet-out (so-called "dry spots") on the girder's surface a few laminae deep. An example of one of these dry spots is shown in Figure 16. In general, dry spot imperfections tend to result from inadequate mold surface preparation, overuse of temporary adhesive during layup, or air bubbles in the feed resin. Repairing these imperfections required straightforward secondary surface infusions, as can also be seen in Figure 16, which could be completed relatively quickly. However, because multiple dry-spots were present on each of the five girders, significant post-processing time was added to the overall manufacturing schedule, and required a significant amount of additional hand labor.



Figure 16: Right: Minor "Dry Spot" Surface Imperfection Left: Secondary Repair Infusion

In addition to the minor surface imperfections present after infusion of each of the girders, the inside face of one of Girder 5's webs was found to have a significant area of improper resin cure and debulking, seen in Figure 17, which required extensive structural repairs. In contrast to the dry spot imperfections found elsewhere on the girder and on others, this defect was quite large

in area and extended through the web's entire interior facesheet to the core. In addition, whereas dry spot imperfections are devoid of resin, this defect was saturated with uncured resin. Repair of this imperfection required removal and replacement of the spoiled fabric in the affected area, followed by thorough cleaning, layup of new fabric, and reinfusion and curing. This process can be seen in Figure 18.



Figure 17: Debulked Structural Defect



Figure 18: Repair of Structural Defect: Left: Removal of Affected Laminae, Center: Layup of New Fabric, Right: Re-Infusion

Based on analysis of the defect and the observation that it was localized to the area of a resin feed-line, it was determined that this defect was caused by contamination of resin with water, which infused the area local to the feed line. To prevent excessive heat build-up during infusion, catalyzed feed resin was kept in thin bucket-liners, which were in turn placed in buckets of water. It is possible that some of this cooling water spilled into the feeder resin, contaminating it and inhibiting its proper curing. This resin was infused into the girder in the location of the eventual defect. The fiber debulking in the area infused by contaminated resin was due to re-exposure to atmospheric pressure after vacuum was released.

The imperfections and defects discovered on each of the HGMB's girders point to an overall need for more stringent quality assurance procedures during future manufacturing efforts for future bridges. Although they were simply aesthetic in nature, the multiple dry spot imperfections discovered on each of the infused girders point to a need for improved mold surface preparation, employee training, and intermediate inspection. This could not only improve the quality of the girders, but also eliminate expenditure of time and labor to repair them. These preventative measures could also help prevent future occurrences of large defects like the one that occurred on Girder 5. It was fortunate that the defect occurred in a web near midspan where shear stresses are lowest, reducing the severity of strength and stability impacts. However, had a similar defect occurred in a more critical location, the structural effect might have been more significant, requiring more substantial repairs or even rejection and re-manufacture.

3 Non-Destructive Live-Load Testing

3.1 Introduction

NDLLT is a method by which the in-situ behavior of a bridge can be inferred and compared with the behavior assumed in design and analysis. It is a well-established practice in bridge engineering which has been codified in the *Manual for Bridge Evaluation* [6] for the purpose of improvement of capacity load rating. In the case of newly constructed bridges, NDLLT can also be used to establish a behavioral base-line for future evaluation, and to verify assumptions made in design. NDLLT was conducted on the HGMB on December 30 and 31, 2020 under a high degree of vehicular live-load. The data collected from this testing were used both to improve the as-designed rating factor (RF) of the bridge, and to examine its behavior relative to design assumptions. The results of testing allowed the bridge's flexural RF to be significantly increased, its load distributive properties to be examined, and its overall stiffness to be compared with the stiffness assumed in design.

3.2 Loading

As in previous NDLLT conducted in previous studies [7,8] the HGMB was loaded by two or four overloaded wheeler-type dump trucks positioned in one of five loading scenarios. These dump trucks were furnished by MaineDOT, and their individual wheel weights, tire contact areas, and wheel bases were measured on site. Each truck had an average gross vehicle weight of 65.6 kip, for a total applied load of 262.5 kip with all trucks on the bridge. Two of these trucks can be seen in Figure 19. The specified truck positions and test runs were selected to maximize moment applied to different parts of the bridge and to examine the bridge's response to differing load levels. Test naming convention follows the pattern: "Test Series_Load Position_Repetition", where "Test Series" denotes the type of test ("SBS", "MAX", or "ALT" as explained below), "Load Position" denotes transverse truck position (1 = downstream, 2 = centered, and 3 = upstream), and "Repetition" denotes the repetition number when multiples of the same test configuration were conducted. In the "SBS" series of tests, two trucks were placed on the bridge with their tandem

back wheels straddling the midspan line. In the “MAX” series of tests, all four trucks were positioned on the bridge such that they were roughly equidistant from midspan in each lane, as close to midspan as possible. Finally, in the “ALT” test, two trucks were positioned identically to the “SBS” configuration, with the remaining two trucks backed as close as possible to the first two. Table 1 shows each of these configurations graphically and lists the Positions and repetitions for each series, and Figure 20 presents an aerial photo of the MAX_1_1 test in progress.

Table 1: Explanation of Test Series

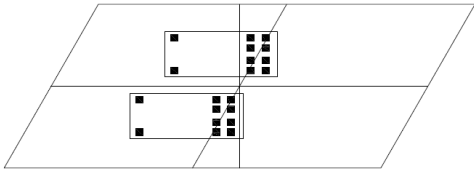
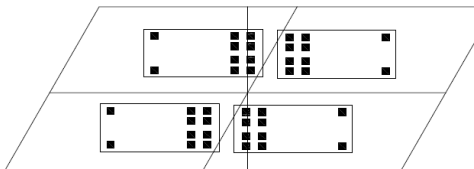
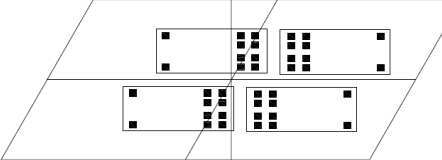
Test Series	Positions Run	Number of Tests	Graphical Representation
SBS	2	2	
MAX	1	1	
	2	2	
	3	1	
ALT	2	1	



Figure 19: Wheeler Type Dump Trucks Used for Loading



Figure 20: Aerial Photo of MAX_1_1 Test (Courtesy of Advanced Infrastructure Technologies)

3.3 Instrumentation

Instrumentation used to monitor bridge response during loading was again very similar to that used in NDLLT performed in previous studies [7,8]. The response of the bridge to loading was measured as strain using the Wireless Structural Testing System (STS-Wi-Fi) produced by Bridge Diagnostics Inc. [9]. This system uses a mobile base station to communicate with six nodes, with four, full-bridge strain transducers connected to each node. Strain transducers measure strain continuously during tests at a sampling rate of 10 Hz. The system communicates with a dedicated laptop running BDI-specific WinSTS data acquisition software, which automatically performs analog to digital signal conversion and rectification of voltage to strain data using built-in calibration factors. One of the 24 transducers used during testing is shown in Figure 21 mounted under the bridge at mid-span. A schematic of the entire network is shown in Figure 22 including strain and displacement sensors, wireless nodes, and the data recording laptop.



Figure 21: Strain Transducer Mounted to the Bottom Flange of a Girder

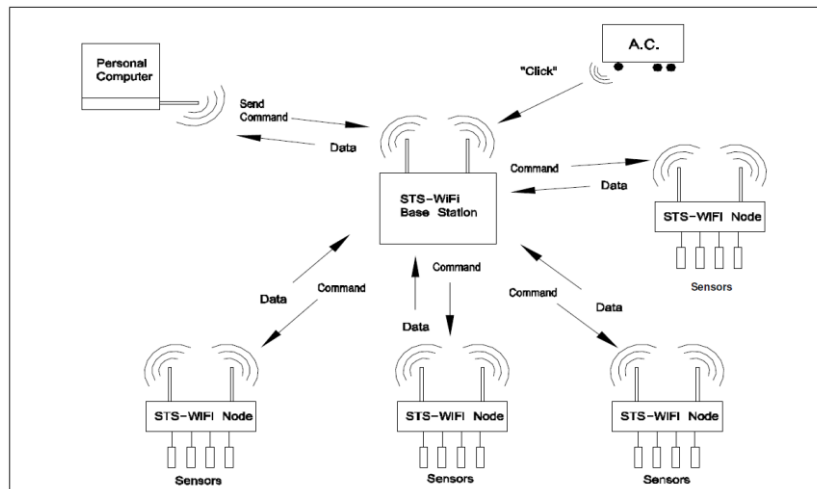


Figure 22: BDI STS-Wi-Fi Network Setup

Strain transducers were mounted under the bridge with the aid of a MaineDOT Under-Bridge Inspection Truck. The sensors were adhered to the girders using LOCTITE 410 toughened instant adhesive with LOCTITE SF7453 accelerator. This forms a strong bond between the sensor mounting tabs and girders within approximately 30 seconds, and achieves full cure within 24 hours. It should be noted that because of the cold temperature (around 30°F) and smooth surface of the girders, more hold-time was needed to ensure secure adhesion than in previous applications [7,8]. Despite this, the majority of the sensors provided reliable data throughout testing, suggesting a strong bond had been achieved. Figure 23 shows the arrangement of sensors applied to each girder at its midspan cross-section. One sensor was located at the bottom flange, one was located on the web 20.25 in. above the bottom, and one on the web 40.5 in. above the bottom. Using three sensors in this arrangement allowed linear distribution of strains through the cross section to be verified, and allowed calculation of each girder's neutral axis height with redundancy. With the

exception of Girder 1, which was instrumented only at midspan, each of the girders also had at least one sensor applied to its bottom flange near the support. These sensors were applied to identify unintended end fixity, manifested as large negative girder end strains. Figure 24 presents a plan-view schematic of the bridge showing the location of each sensor, with the terms “BOT”, “MID”, and “TOP” referring to the same vertical positions shown in Figure 23.

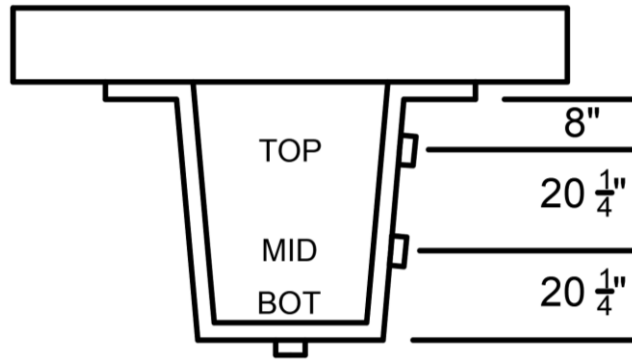


Figure 23: Midspan Sensor Arrangement

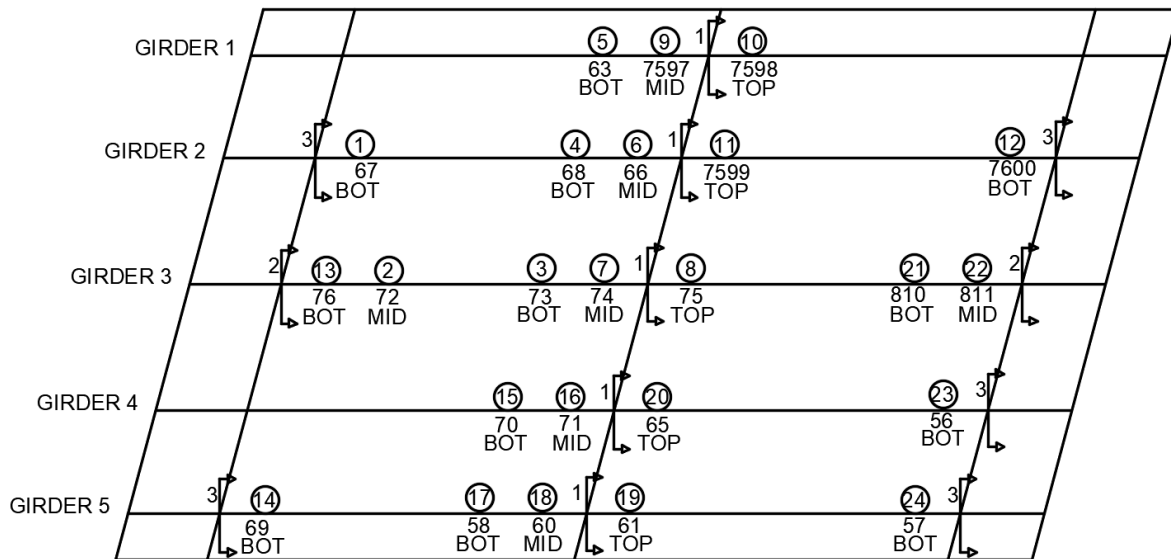


Figure 24: Plan View of Sensor Layout

3.4 Results

From the strains measured during NDLLT (and described in greater detail below), updates to the flexural RFs for each of the girders can be computed. These load-test updated RFs are specified by the *Manual for Bridge Evaluation* [6] as shown in Equation 1.

$$RF_t = RF_c \left(1 + K_b \left(\frac{\varepsilon_c}{\varepsilon_t} - 1 \right) \right) \quad \text{Equation 1}$$

where RF_c is the nominal RF (independently calculated based on the bridge's design drawings and calculation package), K_b is a factor accounting for the ability to extrapolate the results of live-load testing to higher loads, ε_c is the predicted strain for a given test, and ε_t is the strain recorded during testing (corrected to eliminate unintended fixity as discussed later). K_b is taken equal to 0.5 to account for the high degree of load applied, but uncertainty that the results can be extrapolated to an applied load of 1.33 times HL-93. This value of K_b is conservative, but higher values (up to a maximum of 1.0) may be justifiable due to FRP's linear-elastic behavior to failure.

The bridge's nominal rating factors (RF_c in Eq. 1) were calculated on a girder-by-girder basis using nominal geometric and material properties. The controlling flexural failure mode was determined to be rupture of the bottom flange in tension. Rather than using a first-ply failure criterion, wherein the bottom flange would be considered "failed" as soon as any ply reaches a limit state, the girder's flexural strength was based on the bottom flange carbon plies reaching their ultimate tensile strain. This results in a somewhat higher resistance than would be available using first-ply-failure as the glass fiber laminae do not drive down the failure strain of the entire laminate. However, this is more than adequately offset by the high degree of strength reduction AASHTO requires for FRP bridge components. In this case, the nominal resistance of the girder is reduced by 62%. In addition, during previous structural testing [2], a similarly designed girder was able to withstand moment equivalent to 2.65 times AASHTO Strength 1 loading using the Maine Modified HL93 truck. This compares quite well with the reciprocal of the product of strength reduction factors, which equals 2.61.

To incorporate the effects of staged construction into the bridge's initial, nominal rating factors, both the girder's resistance and the loads placed upon it were converted to equivalent strains in the bare girders or composite sections as appropriate. This is demonstrated in Equation 2. Eq. 2a gives the standard AASHTO [6] RF equation for flexural members, where ϕ is the appropriate strength reduction factor for bending, M_n is the member's nominal flexural capacity, γ_{DC} , γ_{DW} , and γ_{LL} are the load factors for dead-load from structural components, dead-load from non-structural components, and live-load, respectively, M_{DC} , M_{DW} , and M_{LL} are the dead-load moment from structural components, the dead-load moment from non-structural components, and live-load moment, respectively, and g is the live-load distribution factor. Using Euler-Bernoulli beam theory and assuming linear elasticity, the moment applied to a beam can be expressed as the curvature in the beam (computed as strain divided by the distance to the neutral axis (y)) multiplied by the girder's flexural rigidity, EI . This is done separately for loads applied to the bare, pre-composite girder prior to curing and participation by the deck (including girder self-weight, hanging utilities, and weight of uncured concrete), and those applied to the composite girder (including dead-load from curbs, sidewalk, railings, and wearing surface, and live-load). Additionally, in anticipation of concrete shrinkage, a distinction is made between the long-term

and short-term composite section, wherein the deck effective width for the long-term section is reduced and applied to composite dead-loads. This is the same procedure as is used for composite steel girder bridges [6] and leads to somewhat more conservative rating factors in comparison to those for which this distinction is not made. It should be noted however, that the reduction in deck effective width used here was calibrated specifically to steel girder bridges, and additional study is needed to determine if the same reduction is appropriate for CT girders.

Equation 2b presents the final rating factor equation after moments have been transformed to strains with appropriate flexural rigidities, where ϵ'_{1t} is the reduced ultimate tensile strain of the carbon laminae in the girder's bottom flange, ϵ_{DC-NC} and ϵ_{DC-C} are the dead-load strains from structural components before and after the deck curing, respectively, ϵ_{DW-NC} and ϵ_{DW-C} are the dead-load strains from non-structural components before and after the deck curing, respectively, and ϵ_{LL} is the extreme tension flange strain from live-loading. For live-loading, the Maine Modified HL93 truck (which is similar to the standard HL93 with the truck/tandem load increased by 25%) was used for inventory-level rating and the standard HL93 loading for operating-level rating. To be consistent with standard load rating practice, AASHTO distribution factors (DFs) were used for distribution of live load (as explained further below), and nonstructural fixtures (i.e. sidewalks, curbs, and railings) were assumed not to contribute any resistance.

$$RF = \frac{\phi M_n - \gamma_{DC} M_{DC} - \gamma_{DW} M_{DW}}{\gamma_{LL} g M_{LL}} \quad \text{Equation 2a}$$

$$RF = \frac{\phi \epsilon'_{1t} - \gamma_{DC} (\epsilon_{DC-NC} + \epsilon_{DC-C}) - \gamma_{DW} (\epsilon_{DW-NC} + \epsilon_{DW-C})}{\gamma_{LL} g \epsilon_{LL}} \quad \text{b}$$

Table 2 presents the nominal and updated flexural RFs for each girder at both the operating (using the AASHTO HL93 truck and operating load factors) and inventory (using the Maine modified HL93 truck and inventory level load factors) levels. Although the nominal rating factors discounted them, calculated strains (ϵ_c in Eq. 1) for exterior girders included the stiffening effects of sidewalks and curbs for consistency with the bridge's observed stiffness. As is immediately apparent, the increases in RF are significant, with percent increases of 23%, 45%, and 60% for Girder 1, the interior girders, and Girder 5, respectively.

Table 2: Comparison of Initial and Updated Flexural RFs

Rating Level	Initial/Updated	Girder 1	Girder 2, 3, 4	Girder 5
Inventory (Maine Modified HL93 Loading)	Initial	1.58	1.17	1.03
	Updated	1.94	1.70	1.64
Operating (HL93 Loading)	Initial	2.54	1.86	1.64
	Updated	3.12	2.69	2.61

3.5 Analysis of Test Data and Girder Behavior

The strains recorded during live-load testing were analyzed to examine the bridge's behavior under loading, to update its flexural RF, and as a benchmark for subsequent finite element analyses. Strain data were recorded continuously throughout the course of each test. Plots of these strain histories are provided in Appendix A. However, for these analyses the maximum strain recorded in any girder by any sensor was selected as the representative point of interest, and the corresponding strains from other sensors at this point taken to complete the data set for the particular test. The points of maximum strain are noted on the strain histories in Appendix A, as well as the corresponding data sets.

Apart from some notable exceptions that will be thoroughly discussed later, trends in the recorded strain data suggest that the bridge behaved much as would be expected under the applied loading. When trucks were positioned closer to a particular girder, that girder was strained to a greater degree than when trucks were positioned further away. In repeated tests (e.g. SBS_2_1 and SBS_2_2, MAX_2_1 and MAX_2_2), measured strains were practically identical, with small observed differences likely reflecting minor variation of truck position. In cases of similar truck position and increased load (e.g. the SBS_2 and MAX_2 tests), the increased recorded strains were roughly proportional to the increase in load. Finally, the midspan strains measured through the depth of each girder tended to confirm a linear distribution of strain. The exception to this was Girder 2, for which the mid-height sensor consistently measured higher-than-expected strain. This is assumed to result from either improper sensor bonding or sensor malfunction, as the girder did not display any other behavior that deviated from that of the other girders.

The linear distribution of strains measured during testing allowed girder neutral axis heights to be inferred and compared with theoretical heights based on transformed section analysis. For this analysis, the integral sidewalk and curb were assumed to act compositely with their respective girders. Additionally, neutral axis heights were calculated for each girder: one assuming a concrete elastic modulus corresponding to the nominal compressive strength (4.0 ksi), and one using the modulus corresponding to the cylinder test-confirmed average concrete compressive strength measured at 28 days (6.55 ksi). With the exception of Girder 2, the inferred neutral axis heights from testing were taken as the average height determined using the top and bottom, top and middle, and bottom and middle sensor's strain readings. These were then averaged across all tests to determine final, inferred neutral axis heights. These values are presented and compared with the theoretical values in Table 3. As can be seen, in all cases the inferred neutral axis was close to, but slightly higher than the corresponding theoretical neutral axis height using the measured concrete strength. This indicates either that the deck was stiffer than expected, or that the girder was more compliant than expected. As seen later, the second option is quite unlikely, considering the inferred increase in flexural rigidity relative to the theoretical value. This stiffer-than-expected deck may result partially from the concrete having a higher elastic modulus than expected, but may also be attributed in part to participation by non-structural fixtures (for instance, the wearing surface and guardrails).

Table 3: Comparison of Theoretical and Inferred Neutral Axis Heights

Calculation Method	Neutral Axis Height above Bottom of Girder (in.)					
	Girder 1	Girder 2	Girder 3	Girder 4	Girder 5	
Theoretical, $f'_c = 4.0$ ksi	57.1	49.6	49.6	49.6	52.8	
Theoretical, $f'_c = 6.55$ ksi	57.5	50.4	50.4	50.4	53.5	
Inferred from Strains	Top and Mid	77.6	138.2	48.8	48.4	61.4
	Top and Bot	61.8	54.7	54.3	53.9	52.8
	Mid and Bot	58.3	49.6	55.9	55.9	51.2
	Average	65.7	52.0	53.1	52.8	55.1

Although the bridge’s behavior as represented by measured strains generally tended to align with expectations, one significant observed deviation was the negative bottom flange strains measured near girder ends. As can be seen in the data sets provided in Appendix A, significant negative strains were measured at the girder ends with magnitudes tending to be between 20% and 40% of the strains measured at midspan, and up to 54% in some cases. These negative strains suggest partial end fixity – that is, girder ends were somewhat rotationally restrained but not perfectly restrained as would be provided by ideal clamped boundary conditions. Despite this restraint being obviously present from the recorded strains, the bridge was designed assuming ideal pin-roller boundary conditions. As this behavior is a major aberration from expected, the causes and effects were investigated.

One possible cause of the apparent partial end restraint measured during live-load testing is the buried approach slabs that are present at both ends of the bridge. These are shown in Figure 25 from the bridge’s original design drawings, which are shown resting on the abutment backwall into which the girders are embedded. The slabs are also connected to the backwall with inclined dowels, indicating that at least some moment can be transferred between the integral backwall and slab. Despite being a real, measureable phenomenon during live-load testing, this end restraint cannot be assumed to be present under all loading and environmental conditions, or to remain over the full course of the bridge’s lifespan. Additionally, rotational restraint tends to reduce strains at midspan leading to higher ratios of computed to measured strains and thus greater increases to RFs when modified based on nondestructive load testing, which is unconservative. For this reason, a method was developed by which the effects of apparent rotational restraint could be eliminated from the measured mid-span strains to better represent simply-supported conditions.

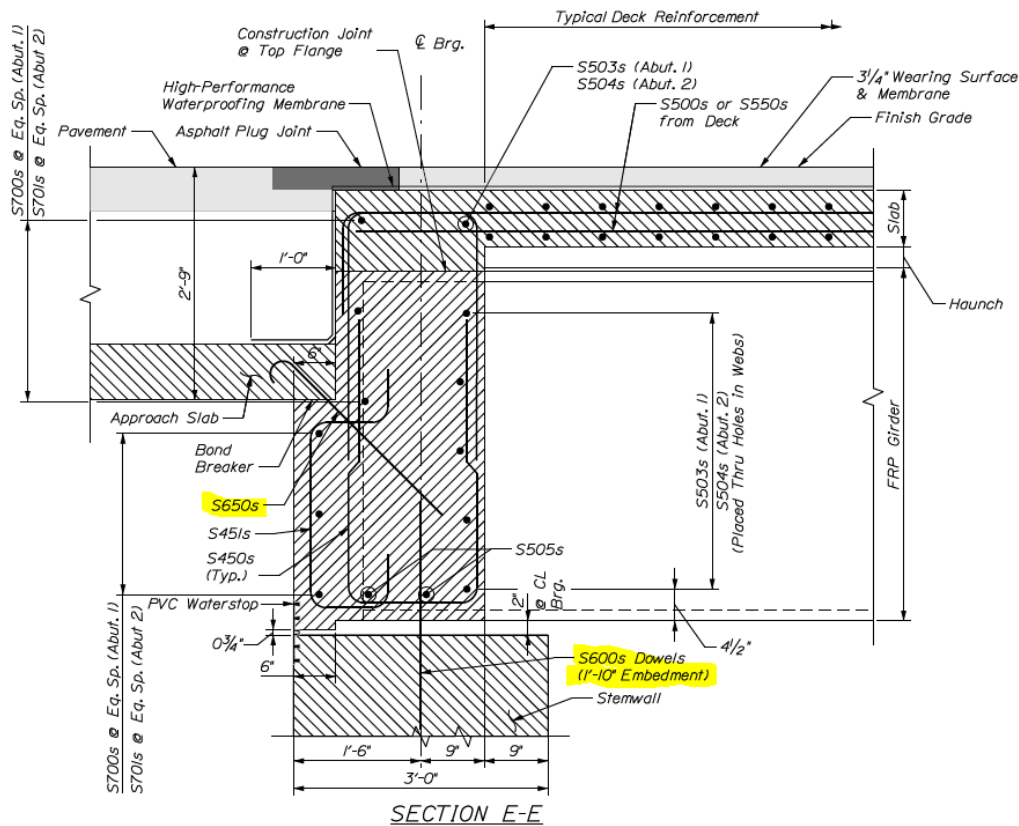


Figure 25: As-designed Girder Ends with Approach Slab

The strains measured were assumed to be a superposition of negative end moments from the restraint onto the structure's simple span behavior. In theory therefore, the bridge's simply supported mid-span strains could be recovered by adding each girder's average end restraint moments to their midspan moments. However, three problems exist which prevent this technique from being implemented directly. First, although the total moment applied to the bridge in each test (assuming simple supports) could be calculated from the bridge span and known truck dimensions and wheel weights, the proportion of total moment carried by each girder was not equivalent to the proportion of total strain measured, and so the individual observed girder mid-span moments (and end moments) were unknown. Said differently, it was not necessarily true that a girder strained twice as much as another carried twice the moment as the other. Second, although the theoretical flexural rigidity of each girder could be calculated, the girders' actual flexural stiffnesses likely differed from the theoretical stiffnesses, and so test moments could not be directly inferred from measured strains using nominal section properties. Finally, because the flexural rigidity of each girder was not constant along its length due to bottom flange ply-drops, measured end strains could not be directly added to mid-span strains to eliminate them. Despite these difficulties, the basic concept of adding end moments to mid-span moment to find the simply-supported midspan moment could still be applied per the analysis detailed next.

From basic, linearly elastic Euler-Bernoulli beam theory, the strain ε in a linearly elastic beam under a certain moment M , can be calculated as

$$\varepsilon = \frac{My}{EI} \quad \text{Equation 3}$$

where y is the distance from the neutral axis (taken as the distance to the extreme tension fiber for maximum strain), and EI is the beam's flexural rigidity. By rearranging Eq. 3, the midspan and average end moments due to test loads, M_m and M_e can be calculated as

$$M_m = \varepsilon_m \left(\frac{EI}{y} \right)_m \quad \text{Equation 4}$$

$$M_e = |\varepsilon_e| \left(\frac{EI}{y} \right)_e \quad \text{Equation 5}$$

where $|\varepsilon_e|$ is the absolute value of the average of two measured negative end strains in one girder and ε_m is the measured positive midspan strain.

At this point, it is assumed that the ratio of flexural rigidity at a girder's ends to the flexural rigidity at midspan is the same for the girder under nominal design conditions as for measured, in-situ conditions during live-load testing. That is,

$$\left(\frac{(EI/y)_e}{(EI/y)_m} \right)^{actual} = \left(\frac{(EI/y)_e}{(EI/y)_m} \right)^{nominal} = r \quad \text{Equation 6}$$

This definition of the ratio r allows Eqs. 4 and 5 to be combined as

$$M_e = rM_m \frac{|\varepsilon_e|}{\varepsilon_m} \quad \text{Equation 7}$$

and the simply-supported mid-span moment to be expressed as

$$M_{ss} = M_m + M_e = M_m \left(1 + r \frac{|\varepsilon_e|}{\varepsilon_m} \right) \quad \text{Equation 8}$$

Assuming the ratio of simply-supported to measured mid-span strain equals the ratio of simply-supported to "measured" mid-span moment, the expected strain at midspan under simply-supported conditions (that is, eliminating the observed rotational restraint) is determined as

$$\varepsilon_{ss} = \varepsilon_m \left(1 + r \frac{|\varepsilon_e|}{\varepsilon_m} \right) \quad \text{Equation 9}$$

It should be noted that in a few cases, the measured girder end strains were slightly positive, in which case they were assumed equal to zero as they did not represent any effective end restraint. Additionally, as will be seen later, preliminary finite element analyses indicate that the monolithic backwall into which the girders were cast may provide some rotational fixity, although the amount is unknown. If this is the case, this fixity might be reliable upon through the bridge's life span, proving this method of eliminating all fixity to be conservative.

Although this method is rational, it does require that strains at both ends of all girders be known. However, strains were only measured at the West end of Girder 4, and no strains were measured at either end of Girder 1. It was observed that the ratios of end strain to midspan strains for each end of the bridge were roughly parabolically distributed across the bridge's width. To predict the missing end strains for Girders 1 and 4, parabolic functions were fit to the ratios $\varepsilon_e/\varepsilon_m$ and plotted as shown in Figures 26 and 27 for the east and west ends of the bridge, respectively. Using these projected ratios, the missing end strains were calculated, again taking positive end strains equal to zero.

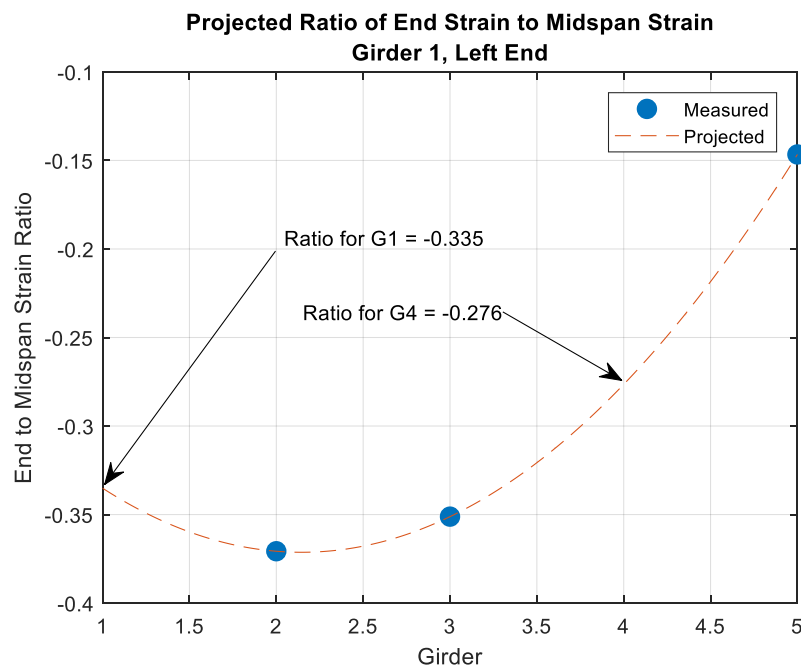


Figure 26: End-to-Midspan Strain Ratios – East End

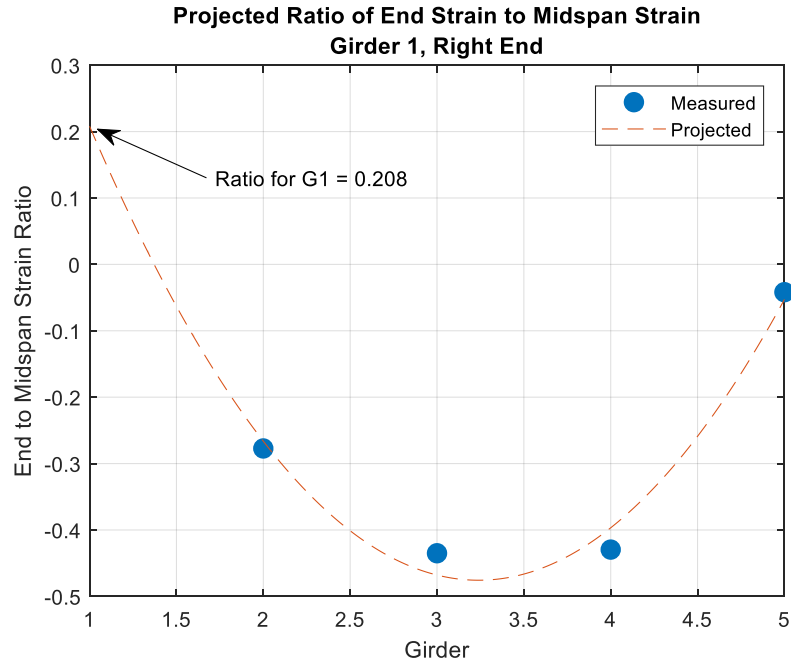


Figure 27: End-to-Midspan Strain Ratios – West End

Table 4 compares the strains measured at the bottom of girders at midspan with those corrected to eliminate end restraint. As can be seen, the corrected strains are generally much larger than the strains measured with the effect of rotational end restraint by up to a factor of two. This increase in test strains helps to increase the conservatism in RF updates by significantly reducing the ratio of predicted to measured strains. This also increases confidence in the resulting RF increase by eliminating the effects of end fixity, the reliable degree of which is unknown and cannot necessarily be relied upon at higher loads or through the bridge’s entire service life.

Table 4: Comparison of Measured and Restraint-Corrected Mid-Span Strain

Test		Midspan Strain ($\mu\epsilon$)				
		Girder 1	Girder 2	Girder 3	Girder 4	Girder 5
SBS_2_1	Measured	72.33	113.8	174.8	136.6	118.6
	Corrected	94.99	226.5	364.1	253.1	178.0
SBS_2_2	Measured	69.69	112.0	176.2	138.8	119.6
	Corrected	91.51	221.0	365.4	263.5	177.0
MAX_1_1	Measured	80.24	153.0	304.4	279.8	345.3
	Corrected	105.4	223.0	536.6	501.9	458.7
MAX_2_1	Measured	125.0	198.4	318.0	237.7	208.0
	Corrected	169.2	349.8	612.2	435.2	249.0
MAX_2_2	Measured	134.4	202.1	309.6	229.8	202.0
	Corrected	176.6	354.1	583.5	412.9	240.8
MAX_3_1	Measured	206.6	251.1	303.3	164.6	103.6
	Corrected	271.4	457.2	560.3	273.5	103.6
ALT_2_1	Measured	124.9	202.4	321.4	239.2	206.0
	Corrected	147.5	328.8	600.8	451.7	235.4

The *Manual for Bridge Evaluation* [6] allows a bridge’s RF to be updated based on the results of nondestructive live-load testing as was performed on the Hampden Grist Mill Bridge. To accomplish this, the strains measured under a given loading are compared with the expected strains under the same moment, using the AASHTO (2012) recommended live-load distribution factors (DFs). However, the expected strains must be calculated based on the structure’s as-built or observed stiffness. Therefore, in order to calculate the expected strain, the bridge’s actual mid-span flexural rigidity needed to be determined. The total simply-supported moment M^T applied to the bridge during each test can be calculated by simple statics, and can then be expressed as the sum of the moment carried by each individual girder or the corresponding strain multiplied by the girder’s flexural rigidity at the extreme tension fiber

$$M^T = \sum_{i=1}^5 \epsilon_i \left(\frac{EI}{y} \right)_i^{actual} \quad \text{Equation 10}$$

where i is the girder number, counted from North to South. Because they are designed to be identical, the flexural rigidities of the interior girders ($i = 2,3,4$) are assumed equal. Additionally, it can be assumed that the ratio of the flexural rigidities of exterior girders to interior girders using nominal dimensions and moduli are equal to the ratios for the actual girders. These ratios, denoted N_1 and N_5 , respectively can be inserted into Eq. 10 and the equation rearranged to give the actual flexural rigidity at the extreme tension fiber of the interior girders

$$\left(\frac{EI}{y}\right)_{interior}^{actual} = \frac{M^T}{N_1\varepsilon_1 + \varepsilon_2 + \varepsilon_3 + \varepsilon_4 + N_5\varepsilon_5} \quad \text{Equation 11}$$

Table 5 compares the flexural rigidity of each girder determined through standard transformed section analysis using nominal girder properties with the actual rigidities determined by Eq. 11. It is apparent that all girders of the bridge are much stiffer than they were designed to be, despite the elimination of apparent end restraint. Increased girder rigidity reduces computed strains, which will in turn reduce the corresponding updated RF.

Table 5: Extreme Tension Fiber Flexural Rigidities

Analysis Method	$\frac{EI}{y} * 10^7 (kip * in)$			
	f'_c or Test	Girder 1	Girder 2,3,4	Girder 5
Transformed Section	$f'_c = 4.0 \text{ ksi}$	1.83	1.33	1.54
	$f'_c = 6.55 \text{ ksi}$	1.93	1.34	1.59
Equation 11	SBS_2_1	2.99	2.17	2.51
	SBS_2_2	2.98	2.16	2.51
	MAX_1_1	3.09	2.24	2.60
	MAX_2_1	3.14	2.27	2.64
	MAX_2_2	3.21	2.32	2.70
	MAX_3_1	3.35	2.42	2.81
	ALT_2_1	3.12	2.26	2.62

To assess the realism of the large increases in girder rigidity, additional analyses were performed to predict bridge deflections under test live-load which could be compared with the deflections of the bridge measured during the live load tests. Before testing and during two specific tests, SBS_2_2 and MAX_1_1, engineers from AIT took elevation measurements of the bridge deck above the girders with a transit level and leveling rod. This allowed rough estimates of the bridge's average deflection to be computed and compared to predictions. Although it was preferable to compare predictions for measured deflections under higher loads (such as those produced during tests using four trucks instead of two), the transverse positioning of trucks to one side of the bridge during the MAX_1_1 test made comparison more complicated. Therefore, deflection predictions were compared with the measured deflections during the SBS_2_2 test.

The deflection of the bridge under SBS_2_2 loading was predicted by solving

$$\frac{d^2v}{dx^2} = \frac{M(x)}{EI(x)} + M^- \quad \text{Equation 12}$$

as a boundary value problem using a finite difference approximation, where $v(x)$ is the average deflection of the bridge at a distance x from the support, $M(x)$ is the moment at the point x produced by SBS_2_2 loading, and M^- is the negative moment resulting from the rotational fixity

observed during testing. The flexural rigidity, $EI(x)$, of the bridge is taken as the sum of the flexural rigidities of each girder, and is a function of x to account for ply drops in the girder's bottom flange 10 ft from either support. Simple boundary conditions were enforced at the supports, and the problem was formulated and solved in MATLAB [10], using its built-in boundary value problem solver, *bvp4c*.

For comparison with measured deflections, the bridge's deflections under SBS_2_2 loading were predicted both with and without the consideration of observed rotational fixity, and using both the nominal (4.0 ksi) and measured (6.55 ksi) concrete compressive strength, for a total of four analyses. The effect of rotational fixity was included using the average end strains recorded in each girder and the nominal flexural rigidity of each corresponding girder at its end. When summed, these moments give M^- in Eq. 12, which was assumed independent of x . To neglect the effects of observed rotational fixity M^- was simply taken as zero with the remainder of the analysis identical. Figure 28 presents the results of these analyses and compares them with the average deflection measured by AIT at midspan. As can be seen, the maximum deflections from each of the predictions significantly exceeded the measured average deflection, even when the effects of rotational restraint were considered. This suggests that the overall bridge system is significantly stiffer than nominal properties would indicate.

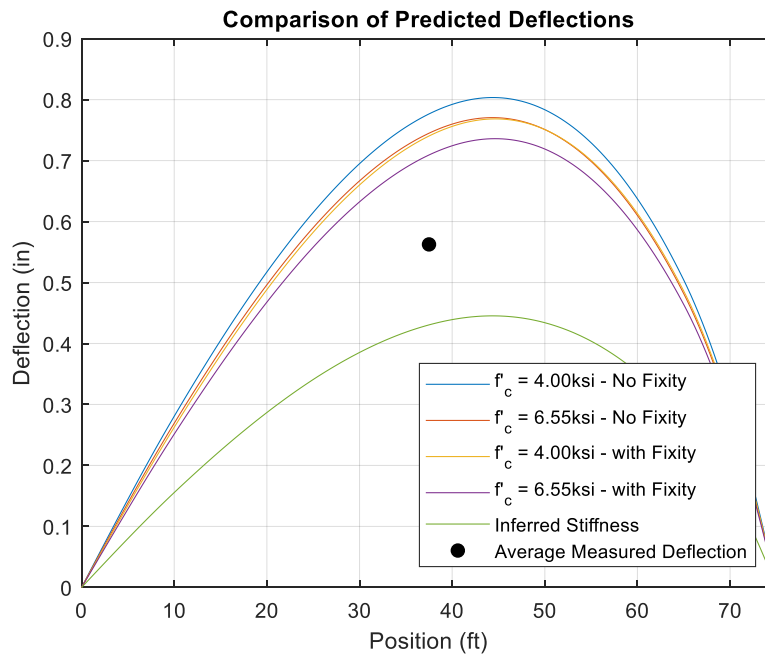


Figure 28: Comparison of predicted and Measured Deflections

In addition to predicting overall deflections using the bridge's nominal sectional properties, an analysis was performed using the flexural rigidities inferred from testing and calculated with Eq. 11 and given in Table 5. For this analysis, rotational fixity was neglected (as the flexural rigidities were computed after elimination of fixity from the measured mid-span strains), and the

ratio of girder end flexural rigidity to midspan flexural rigidity was assumed constant (as stated by Eq. 6). The results of this analysis are also presented in Figure 28. As can be seen, the average measured deflection is under-predicted in this analysis. However, the difference between the measured and maximum predicted deflections for this analysis is smaller (in an absolute sense) than the same difference for any of the predictions using nominal properties. Additionally, the average measured deflection is based on only two measurements, one being from the center girder, the girder that would presumably have the highest deflection. With additional measurements, the average measured deflection would likely decrease, further aligning the maximum predicted and measured deflections. It must be mentioned that the measured deflections and the prediction methods used are relatively crude, and so caution must be taken before using the numeric results presented. However, in terms of general trends and comparisons, these results suggest that using flexural rigidities that significantly exceed nominal values is reasonable. Additionally, the use of greater flexural rigidity reduces the increase to the girder RF inferred from non-destructive live load testing per the *Manual for Bridge Evaluation* [6]).

Using the inferred flexural rigidities calculated in Eq. 11 and additionally justified by comparing predicted and measured deflections, the expected strain ε_c in each girder resulting from test loading (and assuming simple boundary conditions) can then be determined as

$$(\varepsilon_c)_i = \frac{g_i M^T}{N_i \left(\frac{EI}{y} \right)_{interior}^{actual}} \quad \text{Equation 13}$$

where g_i is the AASHTO [3] DF calculated for the girder and $N_i = 1$ for $i = 2, 3, 4$.

In addition to updates in RF, the results of live-load testing can be used to estimate live-load distribution. AASHTO's DFs represent the highest fraction of one lane of live-load that can be applied to a particular girder. During testing, trucks were positioned in discrete positions, which may or may not have caused the absolute maximum live-load to be carried by a particular girder. For this reason, the estimation of live-load implied by the results of testing are not DFs in the strictest sense and so have been called "Girder Lane Fractions" (GLFs) to avoid confusion. GLFs are the number of lanes of loading carried by a particular girder under a particular loading scenario and, when multiple loading scenarios are run along the width of a bridge, can reveal trends in live-load distribution that can be used to assess the accuracy of AASHTO DFs. A girder's true DF is equal to or greater than the largest GLF observed for that girder. For the i^{th} girder, the GLF is calculated as

$$GLF_i = \frac{2N_i \varepsilon_i}{\sum_{i=1}^5 N_i \varepsilon_i} \quad \text{Equation 14}$$

where the "2" in the numerator accounts for the two lanes of loading used during testing. Table 6 compares the AASHTO calculated DFs for each girder with the GLFs calculated in each test, with

the girder’s maximum GLF in bold face. As is immediately apparent, the maximum GLFs of two of the five girders exceeded the AASHTO specified DFs, indicating that the DFs used in design were unconservative. For the remaining girders, the test GLFs are smaller than the specified DFs. However, as the difference is not very large, this does not preclude the true DF from being larger than that specified. For the most heavily loaded interior girder, the AASHTO DF is 7.1% less than the value inferred from testing, which indicates that the AASHTO DFs are reasonable for interior girder design, but somewhat unconservative. It should be noted that the bridge’s AASHTO DFs were calculated assuming it to behave as a concrete type “c” superstructure as shown in AASHTO Table 4.6.2.2.1-1 (cast-in-place concrete slab on precast concrete box beams) and with the corresponding equations from Tables 4.6.2.2.2b-1 and 4.6.2.2.2d-1 [2]. Presumably, the girders’ stiffness would align more closely with that of a steel type “c” superstructure (cast-in-place concrete slab on steel box beams), but the bridge’s details (specifically the ratio of number of design lanes to number of girders) precludes the use of the corresponding equations from AASHTO Tables 4.6.2.2.2b-1 and 4.6.2.2.2d-1.

Table 6: Comparison of AASHTO DFs and Test Computed GLFs

Test	Girder 1	Girder 2	Girder 3	Girder 4	Girder 5
<i>AASHTO</i>	<i>0.286</i>	<i>0.601</i>	<i>0.601</i>	<i>0.601</i>	<i>0.609</i>
SBS_2_1	0.222	0.383	0.616	0.429	0.350
SBS_2_2	0.214	0.374	0.619	0.446	0.347
MAX_1_1	0.150	0.230	0.554	0.518	0.549
MAX_2_1	0.243	0.364	0.638	0.453	0.301
MAX_2_2	0.260	0.378	0.623	0.441	0.298
MAX_3_1	0.420	0.512	0.628	0.306	0.135
ALT_2_1	0.219	0.354	0.647	0.486	0.294

As seen in Table 6, the predicted AASHTO [3] DF for Girder 1 was much smaller than the corresponding GLF computed for the MAX_3_1 test. Without additional context, this brings into question this girder’s rating and design. However, additional information can help temper this concern. The distance between the center of Girder 1’s exterior web and the inside face of the sidewalk (denoted d_e by AASHTO) is slightly over 4 ft, taken as negative because the face of the curb is inboard of the exterior web. Using AASHTO Table 4.6.2.2.1-1, this bridge most closely resembles a type “c” superstructure (“concrete deck on spread box beams”). According to Table 4.6.2.2.2d-1, a negative d_e eliminates this girder from being described by the corresponding AASHTO exterior DF equations, meaning that DF must be calculated by the lever rule with the hinge placed at Girder 2. Accordingly, and due to the relatively close girder spacing, only a single wheel line (half of a lane) of load is applied, leading to a low calculated DF, even when the 1-lane multiple presence factor is applied.

During the MAX_3_1 test, trucks were positioned transversely to maximize the load applied to Girders 1 and 2. The center of the wheel line placed nearest to Girder 1 was about 22 in. from the inside edge of the sidewalk, 2 in. closer than the minimum specified by AASHTO and

slightly increasing the lever-rule-calculated DF. More importantly however, the hinge at Girder 2 assumed in the lever-rule is fictitious and far from the actual behavior exhibited by the bridge. A significant portion of the load applied over Girder 2 was also distributed to Girder 1, increasing the GLF above that which it would have carried if the hinge did actually exist. A final consideration is that in the design documentation, a single DF was calculated for use on both Girders 1 and 5. This DF, reported as 0.613 exceeds the maximum GLF for Girder 1 and confirms that the girder's design is in fact adequate. This being said, a more thorough review of the bridge's load distribution is warranted, and will be addressed with subsequent finite element analyses.

4 Finite Element Analysis

4.1 Introduction

The finite element (FE) method is a powerful numerical technique that allows the efficient analysis of complex structures. It considers a structure as an assemblage of discrete, finite elements, and, by minimizing their total potential energy (in a linearly elastic analysis) or through satisfying virtual work principles (linear or nonlinear analysis), can be used to predict internal and external load effects with a high degree of accuracy depending on the level of detail a model uses. In practice, bridge FE analyses tend to be simplistic, providing the primary benefit of improving the prediction of load distribution. However, as the complexity of a FE model increases, a bridge's behavior can be represented more closely, to the point at which behavior measured during live-load testing can be accurately emulated and so investigated further. The HGMB was modeled and analyzed using the FE method for the purpose of increasing understanding of its behavior.

4.2 Modeling

The FE models used in this study were constructed in, and analyzed with the commercial FE software, ABAQUS [11] to take advantage of its sophisticated modeling and analysis environments, its availability, and the authors' familiarity. The models were highly detailed, explicitly incorporating most of the components that could be reasonably assumed to contribute to the structure's response in a significant way. These components included the bridge's girders, FRP top plates (which span the girders top flanges, creating a closed section), concrete backwalls, deck, wearing surface, curb and sidewalk, and railings.

Concrete components (deck, sidewalk and curb, and backwalls), as well as asphalt components (wearing surface) were modeled with C3DR20 three-dimensional, quadratic, 20-node, reduced integration brick elements with three degrees of freedom per node. These were assigned isotropic, linearly elastic constitutive behavior with appropriate elastic moduli and Poisson's ratio and uniform mass density. FRP components (girder and top plates) and the steel components making up the bridge's railings were modeled with S8R three-dimensional, quadratic, 8-node, reduced integration shell elements with six degrees of freedom per node. Like the concrete components, the steel components were modeled as linear elastic and isotropic. However, the

constitutive models of the FRP components were much more complex due to their inherent orthotropy. The top plates were given a single, uniform orthotropic constitutive model based on properties reported by the manufacturer, with material coordinates assumed to be aligned with the plates' axes. The girders were much more complex, owing to the multiple plies of differing materials, thicknesses, and orientations, with each ply being orthotropic relative to its own material axes. Fortunately, ABAQUS allows most shell elements to be assigned laminate lay-ups, which explicitly incorporate a lamina's constitutive properties, material orientation, and thickness, and assembles them together when assigning an element's constitutive behavior. Using this constitutive definition, the elements making up girders' top flanges, webs, transition fillets, and bottom flanges were assigned their own specific laminate properties. In addition, two separate laminates were defined for and assigned to bottom flanges (for the ends and for the center portion of the girder) to account for ply drops incorporated into the actual girders' layups. Finally, the reinforcing bar embedded within the deck was explicitly modeled as B31 three-dimensional, linear, 2-node beam elements with six degrees of freedom per node. These were assigned geometric properties corresponding to the particular rebar section and elastic constitutive behavior. A fully meshed model can be seen in Figure 29.

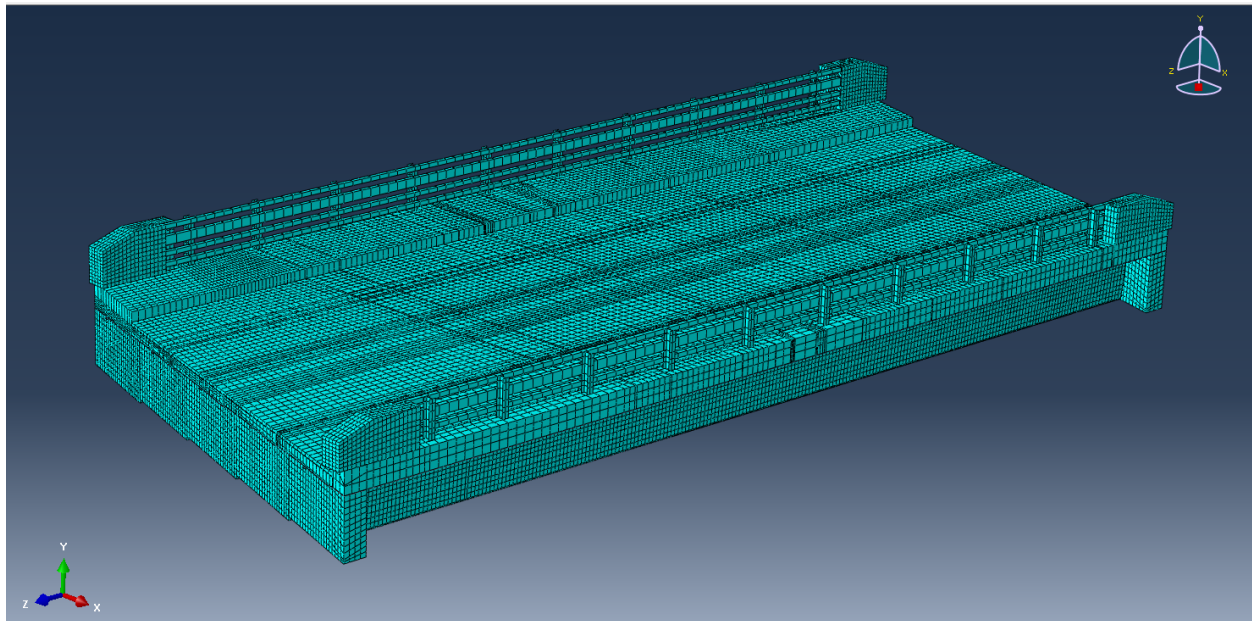


Figure 29: Meshed FE Model

In total, the models each contained around 160,000 elements and 339,000 nodes. The mesh density of different components was determined by a convergence study, which tracked maximum vertical deflection as a function of number of elements. The results of this study can be seen in Figure 30. It should be noted that the number of elements determined from this convergence study did not include the elements making up the wearing surface, deck reinforcement, or rails, which contribute the remaining elements. Additionally, although it appears that deflection does not converge when increasing the number of elements in the backwalls, a large number of data points

exist at the end with very little increase in deflection, and the scale of the plot makes these hard to see.

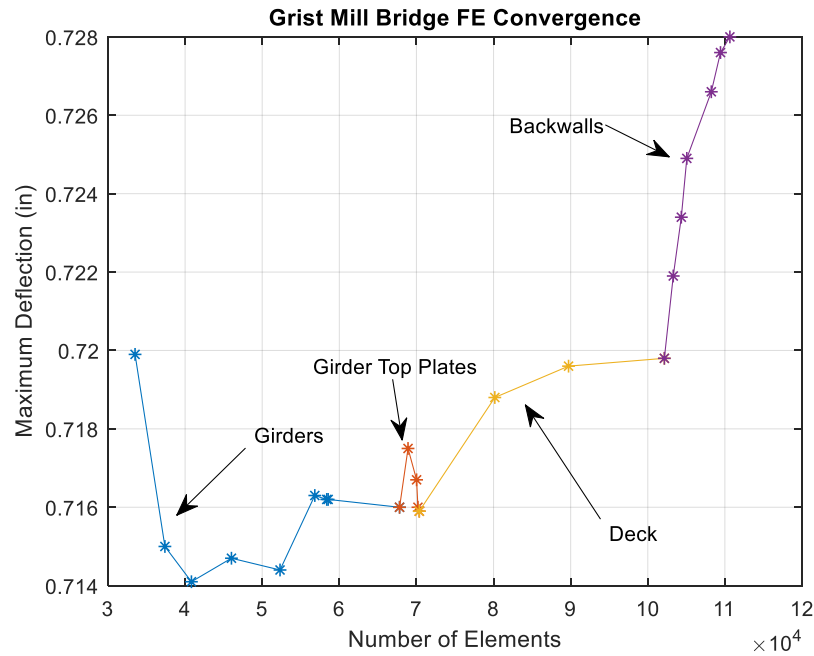


Figure 30: Mesh Refinement Convergence Study

In general, the various components of the models were connected rigidly using tie constraints. These constraints kinematically couple the degrees of freedom of the nodes on adjacent surfaces such that they act perfectly adhered. The exception to this was the connection between the girders and the backwall, and the rebar within the deck. These connections used an “embedding” constraint, which mimics the behavior of one material encased within another (such as reinforcing bar encased within concrete). Global stability was enforced by assigning appropriate boundary conditions along the girders’ bearing centerline. The bearing line of one side of the bridge was assigned translational restraint in all directions, whereas the opposite side was assigned translational restraint in the transverse and vertical directions. This effectively produced the simple-support conditions for which the bridge was designed.

Load was applied in two separate load-steps; a dead-load and a live-load step. In the dead-load step, uniform gravitational acceleration was applied to the entire model which, when acting on individual materials’ mass density applied an accurate representation of dead-load weight. In the subsequent live-loading step, load was applied to mimic that from the load applied during individual live-load tests. Using trucks’ measured wheel weights, axle spacings, tire contact areas, and positions on the bridge, the areas of the wearing surface components were partitioned and appropriate surface tractions were applied and given magnitudes equivalent to the trucks’ applied tire contact pressure. Both load steps were solved with a standard Newton-Raphson solution algorithm, with the results of the first load-step propagating to the beginning of the next. Separate

load-steps were used because the analyses considered geometric nonlinearity, and thus the principle of superposition could not be applied. Geometric nonlinearity was considered to better account for the bridge's actual conditions and uncertainty of its overall behavior, although deformations were small and the response was likely not significantly impacted by geometric nonlinearities. It is possible that additional accuracy could be achieved by explicitly considering the effects of staged construction within the model formulation. However, incorporating these effects would be quite complex and would likely increase solution time and probability of non-convergence.

4.3 Model Calibration

After having created the FE models, developed an appropriate mesh, and verified their basic functionality and solution, the process of calibration against the measured behavior of the HGMB began. In its initial state, the model predicted live-load strains which significantly exceeded those measured during load testing. In addition, the base models predicted some rotational fixity at girder ends as indicated by small, negative longitudinal strains. These negative strains were likely a result of restraint from the backwall. The area at which these negative strains were detected, as well as its proximity to the backwall can be seen in Figure 31. However, these negative strains were smaller than those measured during live-load testing, suggesting additional factors and sources needed to be included in the models. For these reasons, calibration focused mainly on factors that could lead to an increase in overall stiffness and/or add rotational restraint to girder ends.

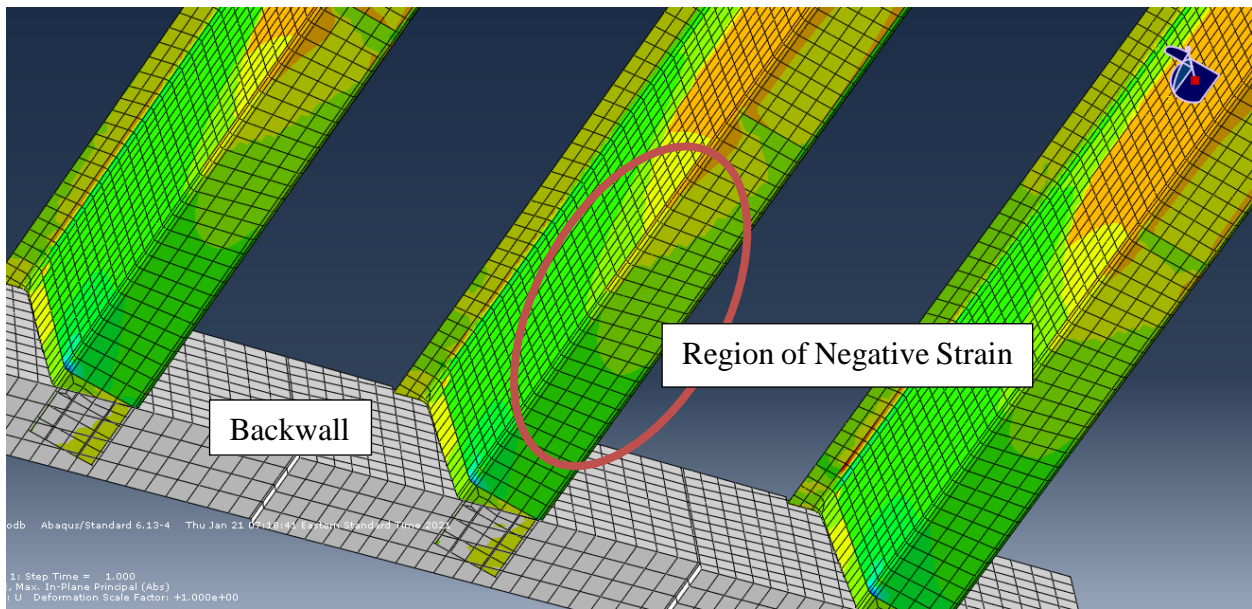


Figure 31: FE Predicted Minor Rotational Restraint from Backwall

The initial changes made to the model focused on increasing its overall stiffness so as to bring predicted strains into closer alignment with measured strains before examining end fixity. This began by updating some of the nominal elastic moduli used to reflect measured, more realistic

values. The initial longitudinal modulus used for the uniaxial carbon for the girders' bottom flanges was 14,400 ksi as reported by the manufacturer [12]. However, coupon testing of infused samples of the same material yielded longitudinal moduli of up to 15,000 ksi [13], and so this modulus was used. In addition, concrete cylinders cast concurrently with the bridge's deck were tested periodically for concrete quality control. At 28 days after casting, these cylinders' compressive strengths ranged between 5.87 and 7.85 ksi, corresponding with elastic moduli ranging between 4,410 and 5,090 ksi [3], significantly greater than the nominal 4 ksi and 3,640 ksi compressive strength and elastic modulus, respectively. To maximize the stiffening effect, an elastic modulus of 5,090 ksi was used. These changes led to a reduction in predicted longitudinal strain as desired, but additional calibration was required to further reduce them and to address girder end strains.

As previously mentioned, a possible source of some of the measured end fixity was the approach slab bearing on the bridge's girder end-walls, which could have applied load eccentrically to the girder ends, inducing a negative end moment. This was incorporated by discretely modeling the backwall's ledge and applying a surface traction to simulate load from the slab and overlying soil and pavement. Because the approach slab would be continuously supported (by either the backwall ledge or underlying soil), the magnitude of the applied traction was unknown. Therefore, initially, two extreme cases were examined: the minimum case of the ledge carrying only the force from the material directly above it, and the case of all load being carried. However, neither case resulted in neither a significant decrease in midspan strains, nor an increase in negative girder end strains. Therefore, alternative methods of incorporating end fixity were explored.

The next possibility explored for simulating the end fixity measured during live-load testing was the incorporation of discrete spring elements into the model. Initially, linear translational spring elements were added to the girders' ends coincident with the center of the roller support. These elements added axial restraint to the girders, which could be varied from no restraint to near complete translational fixity (e.g. pin-roller boundary conditions to pin-pin conditions). Each girder's spring was assigned identical spring stiffness to facilitate modeling, and several analyses were performed with increasing values of spring stiffness. Figures 32 and 33 present the locations of springs in these and subsequent analyses where they were applied to the model. Here, the girders, deck, and backwall are colored green, red, and blue respectively and springs are represented as triangles. These are further described in Table 7. In these first analyses, only Type 1 springs were used.

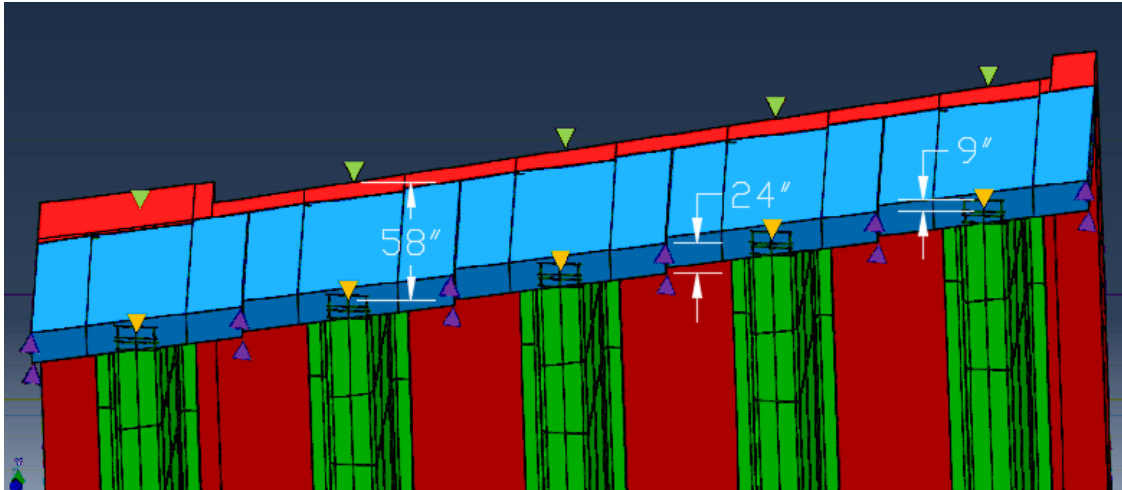


Figure 32: Locations of Spring Elements – Bottom View

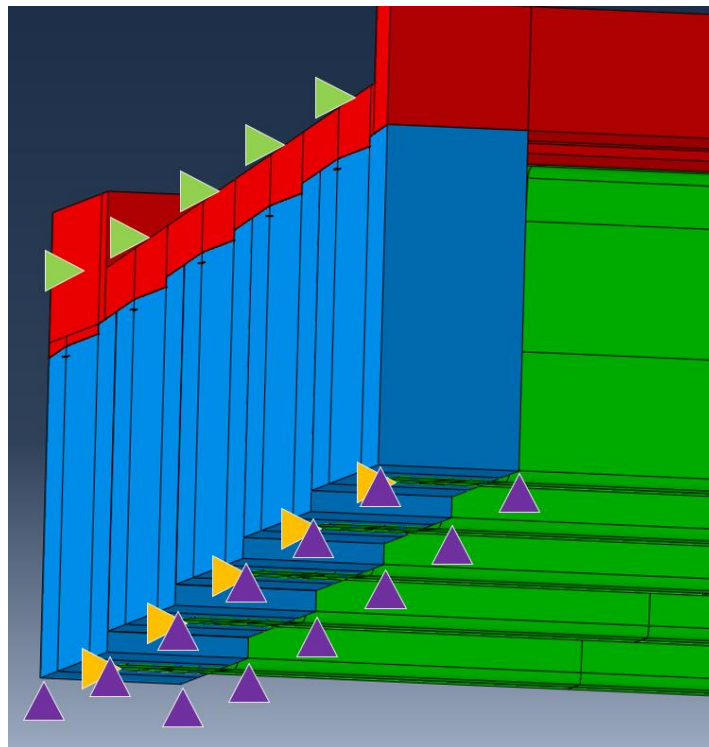


Figure 33: Locations of Spring Elements – Side View

Table 7: Description of Restraining Spring Elements

Name	Description & Location	Symbol in Figures 32 & 33
Type 1	Linear spring at girder ends, centered on bottom flange at support, resists longitudinal motion of girder	Orange triangle
Type 2	Linear spring at girder ends, centered on top of deck above girder centerline, resists longitudinal motion of girder	Green triangle
Type 3	Springs on backwall base, in pairs resisting rotation of the backwall	Purple triangle

Figure 34 presents the error between predicted and measured strains using increasing spring stiffness for midspan strains, girders end strains, and a combination of the two for spring stiffnesses ranging from zero to effectively infinite. These were determined as

$$Error = |\varepsilon_{Predicted} - \varepsilon_{Measured}| \quad \text{Equation 15}$$

where $\varepsilon_{Predicted}$ is the strain predicted by the FE model, $\varepsilon_{Measured}$ is the corresponding strain measured during live-load testing, and the double bars indicate the Euclidian norm (2-norm). As can be seen, each increase in spring stiffness led to a corresponding increase in accuracy for predicted midspan strains, while a minimum error exists at girder ends and for the model as a whole. This minimum error occurs for a spring stiffness of around 731 kip/in, roughly midway between negligible and (effectively) full restraint. This behavior can possibly be attributed to the effects of shear-lag, as the locations of measured girder end strain were quite close to the locations of longitudinal springs.

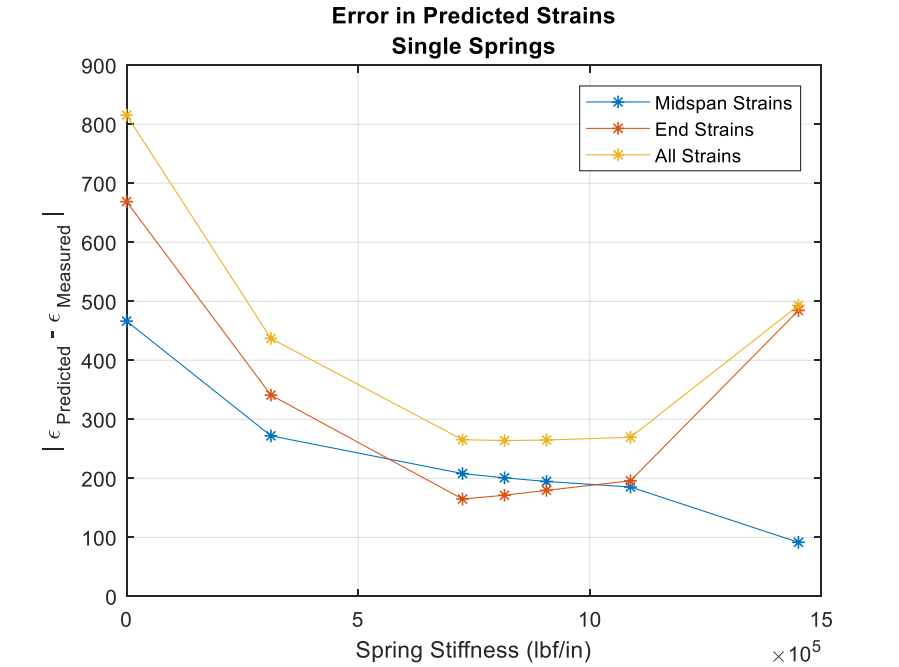


Figure 34: Error in Strain Prediction with Single, Discrete Type 1 Spring Elements

While the addition and manual tuning of single, linear spring elements to girder bottom flanges resulted in improvements to the model’s strain predictions both at midspan and at girder ends, the error remained relatively high. Therefore, alternative methods of incorporating partial girder end fixity were investigated which had the potential to further improve these predictions. Initially, it was hypothesized that the previously used linear springs at girder bottom flanges could be replaced with rotational springs arranged to act at girders’ neutral axes. These were meant to provide rotational restraint without inducing shear-lag effects or placing undue additional strain on girders’ bottom flanges. The location of neutral axes corresponded roughly to the girders’ top flanges, so rotational springs were applied in these locations. However, this method proved either detrimental for the solver, or simply unsuccessful. Because of the various constraint functions used to kinematically couple the girders, top plates, and backwalls, the introduction of additional constraints to the degrees of freedom of the top flanges at girder ends led to solution errors and simulation termination. The over-constraint problems could not be solved by moving the springs to less highly restrained regions of the upper flange. However, because of its relatively flexible behavior, the upper flange was only affected locally by the rotational springs, with negligible effects felt throughout the rest of the girder. For this reason, two additional alternatives were sought and tested.

Although introducing discrete rotational springs did not provide the desired restraining effects, the concept itself was not immediately abandoned. Rather, the concept was modified such that its effect could still be used. To this end, rather than using discrete rotational springs at the neutral axis, tandem springs were incorporated, one at girder’s bottom flange and one at the top of the

deck above each girder which could produce a couple. This scheme used both Type 1 and Type 2 springs which were assigned equal stiffnesses. Although this restraint method could not fully eliminate the shear-lag effect, its severity was reduced by inducing a more even distribution of stress into the girders. As before, all springs were assigned a uniform stiffness, which was varied across numerous simulation runs from zero to essentially infinite stiffness to find the most appropriate stiffness value. In addition, the horizontal restraint boundary conditions initially placed at one end of each girder were removed, as placing spring elements at both sides of a girder ensured adequate horizontal stability. Figure 35 presents the error calculated with Eq. 15 between measured and predicted strains using this restraint method for strains at midspan, girder ends, and girders as a whole.

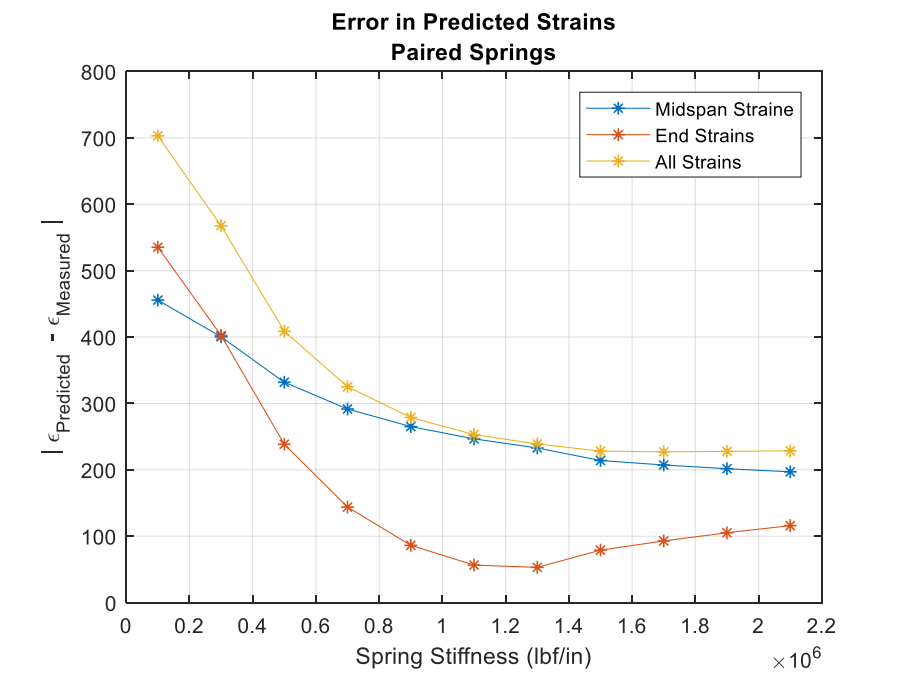


Figure 35: Error in Strain Prediction with Equal, Paired, Discrete Spring Elements

An additional method explored for introducing partial end restraint into the models' girders was to simulate rotational restraint from the girders' bottoms. This was accomplished by adding Type 3 springs, linear spring elements to the bottom of the backwalls, which acted in the vertical direction. These are represented by the purple triangles in Figures 32 and 33. The springs forward of the centerline-of-bearing would apply upward forces to the backwall (and by extension the girders), and the springs behind would apply downward forces, both proportional to their distance from centerline-of-bearing. Again, springs were provided uniform stiffnesses, with stiffness changed across numerous analysis runs. Figure 36 presents the error calculated with Eq. 15 resulting from each of these increases in spring stiffness. As can be seen from Figures 35 and 36, addition of pairs of rotational springs and distributed backwall springs resulted in similar minimum

total error between FEA predicted and measured strains, 227 $\mu\epsilon$ with 1,700 kip/in springs and 240 $\mu\epsilon$ with 2,250 kip/in springs respectively.

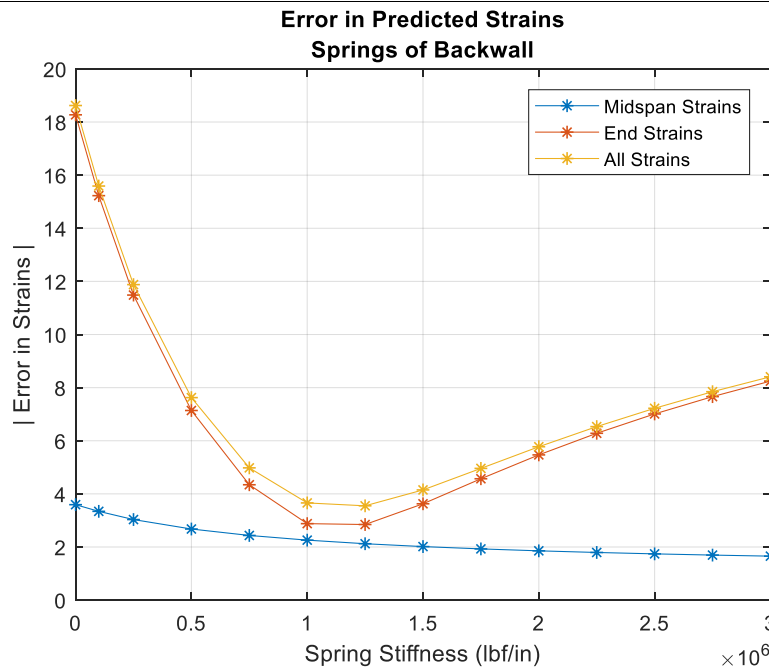


Figure 36: Error in Strain Prediction with Distributed Spring Elements

As a final attempt to reduce the error in predicted strain relative to measured strain, the use of Type 1 and 2 springs was again investigated. However, rather than remaining equal, the stiffness of both types were allowed to vary from one another. This was done so that both the magnitude and vertical position of the couple formed could be tuned simultaneously. Rather than adjusting the two variables (upper and lower spring stiffness) manually, a nonlinear optimization algorithm was employed. This algorithm, a gradient-free, interior-point trust-region method [14], was implemented within MATLAB [10] with its built-in function *fminsearch*. The algorithm was configured to run simulations automatically, altering the spring stiffnesses used in each run by updating the pre-written input file, and used as its objective function the minimization of the square root of the sum of the errors between predicted and measured strains. The initial values were based on stiffnesses leading to low midspan and girder-end strains as shown in Figure 35. However, after several iterations of the algorithm, it became clear that this particular optimization implementation was unlikely to lead to significant increases in accuracy of predicted strains. The algorithm converged (to within a practical level of precision) to a constant total error equal to that of the best-case implementation of equal springs (around 227 $\mu\epsilon$) and little significant further improvement seemed likely. Therefore, the final, calibrated model was taken as the one using Type 1 and 2 springs with a stiffness of 1,700 kip/in. This configuration and stiffness of springs was then applied to the models whose loadings represented the other tests conducted on the HGMB, with all other parameters and previous calibration variables kept constant.

4.4 Results

With the final calibration efforts applied to the models representing each live-load test conducted on the HGMB, the analyses were conducted and the resulting strains (at the locations they were recorded during testing) were recovered. Because calibration focused on the results of one test (MAX_2_1), the resulting accuracies are varied, but in general, the agreement between tests and models increased significantly between base, un-calibrated models and calibrated models. Tables 8 through 14 compare the strains measured during each test to those predicted by the corresponding un-calibrated and calibrated FE models. In addition, Table 15 summarizes the sum-of-squares error between measured and predicted strains for each test before and after calibration.

Table 8: Comparison of Measured, FE Un-calibrated, and FE Calibrated Strains – SBS_2_1

Measured ($\mu\epsilon$)					
Location	Girder 1	Girder 2	Girder 3	Girder 4	Girder 5
Top	25.6	33.6	49.0	38.1	28.5
Mid	54.1	101.7	105.3	82.1	79.5
Bot	72.3	113.8	174.8	136.6	118.6
Left End	-	-61.6	-79.6	-	-39.3
Right End	-	-34.2	-81.2	-67.3	-17.6
FE – Un-calibrated ($\mu\epsilon$)					
Location	Girder 1	Girder 2	Girder 3	Girder 4	Girder 5
Top	44.4	62.0	69.6	60.6	37.6
Mid	95.6	144.5	170.8	165.6	105.8
Bot	140.8	209.4	264.9	259.1	182.0
Left End	-	-66.1	-90.3	-	-1.74
Right End	-	-62.7	-102.5	-98.6	-21.7
FE – Calibrated ($\mu\epsilon$)					
Location	Girder 1	Girder 2	Girder 3	Girder 4	Girder 5
Top	41.6	57.3	64.2	57.5	38.6
Mid	84.2	121.4	143.1	138.3	94.6
Bot	122.3	172.9	215.3	210.9	155.7
Left End	-	-52.4	-82.0	-	-40.7
Right End	-	-50.9	-81.1	-80.0	-42.6

Table 9: Comparison of Measured, Un-calibrated, and Calibrated Strains – SBS_2_2

Measured ($\mu\epsilon$)					
Location	Girder 1	Girder 2	Girder 3	Girder 4	Girder 5
Top	24.3	32.3	49.7	39.2	29.0
Mid	52.3	99.9	106.8	83.6	80.9
Bot	69.7	112.0	176.2	138.8	119.6
Left End	-	-59.2	-79.6	-	-37.9
Right End	-	-33.4	-81.1	-67.6	-17.0
FE – Un-calibrated ($\mu\epsilon$)					
Location	Girder 1	Girder 2	Girder 3	Girder 4	Girder 5
Top	43.8	62.2	69.9	62.8	37.3
Mid	94.8	147.0	173.8	166.7	105.2
Bot	139.5	213.1	269.6	260.4	180.6
Left End	-	-66.8	-95.7	-	0.9
Right End	-	-51.9	-106.1	-99.2	-22.1
FE – Calibrated ($\mu\epsilon$)					
Location	Girder 1	Girder 2	Girder 3	Girder 4	Girder 5
Top	39.6	56.7	63.7	57.3	38.8
Mid	79.9	120.9	143.8	138.3	95.2
Bot	115.6	170.8	217.4	212.0	156.5
Left End	-	-50.4	-83.4	-	-41.0
Right End	-	-49.1	-83.2	-80.3	-42.6

Table 10: Comparison of Measured, Un-calibrated, and Calibrated Strains – MAX_1_1

Measured ($\mu\epsilon$)					
Location	Girder 1	Girder 2	Girder 3	Girder 4	Girder 5
Top	26.0	32.0	73.7	64.7	78.9
Mid	57.6	117.9	167.2	159.6	226.5
Bot	80.2	153.0	304.4	279.8	345.3
Left End	-	-24.0	-84.0	-	-67.6
Right End	-	-35.4	-113.3	-111.3	-40.3
FE – Un-calibrated ($\mu\epsilon$)					
Location	Girder 1	Girder 2	Girder 3	Girder 4	Girder 5
Top	51.9	65.3	87.2	99.5	96.9
Mid	111.1	173.4	257.7	291.0	273.7
Bot	165.9	267.9	417.5	478.7	448.6
Left End	-	1.1	-158.8	-	-168.1
Right End	-	-24.0	-153.4	-207.2	-139.9
FE – Calibrated ($\mu\epsilon$)					
Location	Girder 1	Girder 2	Girder 3	Girder 4	Girder 5
Top	42.8	59.0	82.0	92.8	102.8
Mid	90.2	144.3	214.0	243.8	251.3
Bot	133.6	219.8	336.1	395.2	395.0
Left End	-	-33.6	-112.1	-	-121.2
Right End	-	-54.0	-130.8	-168.9	-160.4

Table 11: Comparison of Measured, Un-calibrated, and Calibrated Strains – MAX_2_1

Measured ($\mu\epsilon$)					
Location	Girder 1	Girder 2	Girder 3	Girder 4	Girder 5
Top	42.6	49.9	77.4	55.3	47.4
Mid	92.9	166.9	185.9	136.0	139.9
Bot	125.0	198.4	318.0	237.7	208.0
Left End	-	-73.6	-111.7	-	-30.5
Right End	-	-55.0	-138.3	-102.1	-8.7
FE – Un-calibrated ($\mu\epsilon$)					
Location	Girder 1	Girder 2	Girder 3	Girder 4	Girder 5
Top	70.4	85.2	100.3	82.2	369.7
Mid	155.7	226.0	282.0	256.9	174.8
Bot	233.2	348.4	458.2	423.6	293.2
Left End	-	-118.8	-212.1	-	39.6
Right End	-	-87.55	-19.0	-184.6	-23.95
FE – Calibrated ($\mu\epsilon$)					
Location	Girder 1	Girder 2	Girder 3	Girder 4	Girder 5
Top	72.2	83.2	87.2	73.5	59.0
Mid	148.8	195.0	224.0	204.6	151.7
Bot	219.4	296.5	356.0	332.1	244.6
Left End	-	-80.7	-138.0	-	-48.3
Right End	-	-94.1	-147.2	-140.3	-61.2

Table 12: Comparison of Measured, Un-calibrated, and Calibrated Strains – MAX_2_2

Measured ($\mu\epsilon$)					
Location	Girder 1	Girder 2	Girder 3	Girder 4	Girder 5
Top	46.4	53.0	75.6	54.1	46.5
Mid	99.3	170.1	181.0	131.7	136.2
Bot	134.4	202.1	309.6	229.8	202.0
Left End	-	-76.5	-106.0	-	-30.5
Right End	-	-52.7	-126.6	-92.1	-6.6
FE – Un-calibrated ($\mu\epsilon$)					
Location	Girder 1	Girder 2	Girder 3	Girder 4	Girder 5
Top	76.6	84.8	95.9	78.0	58.3
Mid	168.2	226.9	271.4	245.3	169.6
Bot	250.7	355.4	441.8	406.0	283.7
Left End	-	-128.2	-197.7	-	48.5
Right End	-	-90.9	-186.5	-171.5	-18.8
FE – Calibrated ($\mu\epsilon$)					
Location	Girder 1	Girder 2	Girder 3	Girder 4	Girder 5
Top	73.8	81.3	88.8	75.0	59.1
Mid	151.5	195.8	228.0	207.5	152.1
Bot	222.6	300.4	361.8	335.4	245.3
Left End	-	-85.2	-142.4	-	-49.6
Right End	-	-92.1	-145.9	-140.7	-60.1

Table 13: Comparison of Measured, Un-calibrated, and Calibrated Strains – MAX_3_1

Measured ($\mu\epsilon$)					
Location	Girder 1	Girder 2	Girder 3	Girder 4	Girder 5
Top	71.6	67.5	72.3	41.9	22.8
Mid	153.9	214.4	180.3	95.2	71.4
Bot	206.6	251.1	303.3	164.6	103.6
Left End	-	-117.6	-110.0	-	3.0
Right End	-	-57.5	-108.3	-47.0	17.9
FE – Un-calibrated ($\mu\epsilon$)					
Location	Girder 1	Girder 2	Girder 3	Girder 4	Girder 5
Top	94.2	102.2	113.2	89.1	37.1
Mid	211.7	261.0	286.9	226.6	112.3
Bot	318.4	407.4	450.0	350.3	192.8
Left End	-	199.0	-213.2	-	173.1
Right End	-	-133.7	-199.3	-119.4	39.8
FE – Calibrated ($\mu\epsilon$)					
Location	Girder 1	Girder 2	Girder 3	Girder 4	Girder 5
Top	80.6	87.3	101.5	77.0	44.8
Mid	167.1	206.0	235.4	197.4	120.8
Bot	246.8	316.8	360.5	311.9	199.0
Left End	-	-95.6	-145.9	-	-21.8
Right End	-	-101.8	-148.4	-125.8	-35.4

Table 14: Comparison of Measured, Un-calibrated, and Calibrated Strains – ALT_2_1

Measured ($\mu\epsilon$)					
Location	Girder 1	Girder 2	Girder 3	Girder 4	Girder 5
Top	43.3	46.2	76.6	55.6	45.6
Mid	91.2	164.3	183.8	136.9	135.4
Bot	124.9	202.4	321.4	239.2	206.0
Left End	-	-53.3	-93.0	-	-14.5
Right End	-	-54.0	-144.4	-114.4	-13.7
FE – Un-calibrated ($\mu\epsilon$)					
Location	Girder 1	Girder 2	Girder 3	Girder 4	Girder 5
Top	83.3	104.8	-79.3	103.6	68.3
Mid	180.4	252.9	307.7	280.1	189.9
Bot	270.0	378.6	479.6	447.9	317.2
Left End	-	-127.3	-226.9	-	60.4
Right End	-	-145.1	-222.3	-197.5	-54.2
FE – Calibrated ($\mu\epsilon$)					
Location	Girder 1	Girder 2	Girder 3	Girder 4	Girder 5
Top	63.7	82.6	98.8	83.9	58.8
Mid	131.9	183.4	225.7	209.9	150.4
Bot	195.7	270.0	342.8	329.1	243.3
Left End	-	-42.1	-103.6	-	-22.7
Right End	-	-105.5	-163.8	-154.5	-81.0

Table 15: Summary of Error in FE Predicted Strains

Test	Error Before Calibration ($\mu\epsilon$)	Error After Calibration ($\mu\epsilon$)
SBS_2_1	252.8	48.3
SBS_2_2	257.4	48.3
MAX_1_1	412.4	252.0
MAX_2_1	536.2	227.2
MAX_2_2	406.2	241.3
MAX_3_1	559.2	275.1
ALT_2_1	539.9	206.9

The comparisons presented in the preceding tables clearly demonstrate that the final calibration scheme used resulted in a significant improvement in the model's ability to predict strains accurately when compared against live-load test measurements. Errors in predicted strains were reduced by a minimum of 39%, with the largest improvements occurring for the strains predicted at girder ends. This suggests that not only was the rotational restraint measured at girder ends significant and due to more factors than the presence of the integral backwall alone, but also that inclusion of tandem spring elements at girder ends in a FE model reasonably and consistently accounts for this restraint.

4.5 Behavior Inferred from FE Models

The midspan strains predicted by the calibrated models allowed girders' neutral axis heights (relative to the bottom of the section) to be calculated. For each girder and each test, three heights were calculated using the predicted strains corresponding to those measured at the bottom and mid-height, bottom and top, and mid-height and top of the girders, and then averaged to get their final values. These are presented in Table 16, along with the overall average height for each girder. Interestingly, Girder 5 was predicted to have the lowest average neutral axis height, despite the presence of the overlying curb. This is also stands in contrast to the neutral axis heights predicted by theoretical calculations and inferred from measured strains as presented in Table 3, in which Girder 5's neutral axis was consistently higher in the section than the interior girders.

Table 16: FE Predicted Neutral Axis Heights

Test	Neutral Axis Height above Bottom of Girder (in.)				
	Girder 1	Girder 2	Girder 3	Girder 4	Girder 5
SBS_2_1	62.2	62.4	58.3	56.5	53.3
SBS_2_2	62.5	62.8	57.9	56.2	53.3
MAX_1_1	60.3	56.3	54.1	52.9	55.0
MAX_2_1	61.0	57.0	53.9	52.2	53.4
MAX_2_2	61.2	56.2	53.9	52.4	53.3
MAX_3_1	62.2	62.4	58.3	56.5	53.3
ALT_2_1	60.5	59.5	57.5	54.7	53.3
Average	61.4	59.5	56.3	54.5	53.6
Relative to:	Percent Error				
Theoretical, $f'_c = 6.55$ ksi	6.9	18.1	11.7	8.1	0.0
NA Inferred from Strains	2.6	14.5	5.9	3.3	-2.8

Numerically, the neutral axis height predicted for Girder 5 was close to that inferred from live-load test strains, and practically identical to the theoretical height using a concrete compressive strength of 6.55 ksi as seen in Table 16. Additionally, the neutral axis height for Girder 1 is also numerically accurate. This suggests that some factor has been introduced into the models, which has raised the predicted neutral axis heights of the interior girders unrealistically. A possible cause is the wearing surface, which was assumed to act fully compositely with the deck, with an elastic modulus of 2,000 ksi considering the ambient temperature during live-load testing around 30°F [15]. As the wearing surface spans across the full effective width of the interior girders and not the exterior girders, any stiffening effect it may have had would affect the interior girders more than the exterior girders, possibly raising their neutral axes artificially high. This was tested by significantly reducing the wearing surface's elastic modulus to nearly zero (it was kept at a small, non-zero value to avoid numerical problems) and rerunning an analysis. Table 17 presents the neutral axis heights calculated from this analysis, along with the percent error relative to those from live-load testing. As can be seen, this change had significant beneficial effects for the predicted neutral axis heights of Girders 1, 2, and 3, and detrimental effects for Girders 4 and 5.

This suggests that the wearing surface may play a part in the differences in between measured and predicted neutral axis height, but that simply reducing its stiffness will not lead to a uniform improvement in prediction. However, a thorough investigation of this would fall outside the scope of this study.

Table 17: Effect of Reducing Wearing Surface Stiffness on Neutral Axis Heights

Neutral Axis Height (in.)				
Girder 1	Girder 2	Girder 3	Girder 4	Girder 5
60.4	56.0	52.5	50.9	51.3
Percent Error Relative to Inferred Strains				
Girder 1	Girder 2	Girder 3	Girder 4	Girder 5
0.96	7.67	-1.22	-3.48	-6.96

In addition to strains, many other measures of bridge and girder behavior could be extracted directly from the results of FE analyses. For instance, Table 18 presents the midspan live-load deflection predicted for each girder during each test. In a similar way to the calculated neutral axis heights, these deflections describe a stiffer response than predicted by theoretical analysis or measured during live-load testing. This stiffer-than measured response is likely due to a combination of factors, among them the use of spring elements to improve the overall accuracy of predicted strains, and the remaining uncertain overall contribution of the wearing surface and elastic moduli of individual components.

Table 18: FE Predicted Midspan Deflection

Test	Midspan Deflection (in.)				
	Girder 1	Girder 2	Girder 3	Girder 4	Girder 5
SBS_2_1	0.185	0.254	0.307	0.304	0.246
SBS_2_2	0.177	0.252	0.310	0.306	0.245
MAX_1_1	0.211	0.358	0.532	0.630	0.642
MAX_2_1	0.342	0.468	0.559	0.535	0.416
MAX_2_2	0.347	0.474	0.565	0.539	0.417
MAX_3_1	0.385	0.502	0.568	0.499	0.343
ALT_2_1	0.317	0.446	0.550	0.530	0.411

An important result of FE bridge analysis is a more realistic prediction of load distribution than is available through conventional 1-dimensional analysis. The results available from the final, calibrated FE models allowed moment distribution to be assessed and compared with the results of live-load testing. The midspan curvature in each girder resulting from live-loading was inferred from its calculated neutral axis height and the strain in the bottom flange and used to calculate the moment carried. In this case, neutral axis heights were determined based on strains from the girder's bottom flange and top layer of reinforcing steel within the deck to ensure that the curvature of the entire section was included. These were consistent with the neutral axis heights calculated

using strains in the girder only as presented in Table 16. This method of calculating individual girder moments allows Eq. 14 to be modified as

$$GLF_i = \frac{2\phi_i EI_i}{\sum_{i=1}^n \phi_i EI_i} \quad \text{Equation 16}$$

with ϕ_i equal to a girder's midspan flexural curvature and EI_i equal to its calculated flexural rigidity, accounting for the updates to model stiffness incorporated during calibration. GLFs calculated from the results of FE analyses for each girder during each test are presented in Table 19 along with the average GLF for each girder. The GLFs predicted by FE analyses indicate a much more uniform distribution of moment than was inferred from live-load testing as presented in Table 6. In general, live-load testing indicated that Girder 3, the central, interior girder, carried significantly more load than other girders regardless of the testing configuration and that the bridge experienced a high sensitivity to horizontal load position. In contrast, the FE predicted GLF for Girder 3 is much less dominant, with GLFs 29% smaller on average than had been inferred. The opposite was true for Girder 1, for which FE analyses predicted 12 to 72% higher GLFs than were inferred from live-load testing. However, the general trends in distribution were similar. For cases in which load was concentrated to one side of the bridge (MAX_1_1 and MAX_3_1), the GLFs from that side of the bridge tended to increase. This indicates that the model gives reasonable prediction of live-load distribution in general, but distributes too much moment to Girder 1 and too little to Girder 3. It is also useful to note that the average predicted GLFs show the AASHTO design DFs to be very conservative for interior girders, reasonably accurate for Girder 5, and unconservative for Girder 1.

Table 19: FE Predicted GLFs

Test	GLF				
	Girder 1	Girder 2	Girder 3	Girder 4	Girder 5
SBS_2_1	0.381	0.343	0.438	0.432	0.405
SBS_2_2	0.364	0.342	0.446	0.438	0.410
MAX_1_1	0.254	0.262	0.406	0.479	0.599
MAX_2_1	0.415	0.353	0.434	0.410	0.387
MAX_2_2	0.416	0.354	0.437	0.409	0.384
MAX_3_1	0.469	0.379	0.443	0.389	0.321
ALT_2_1	0.385	0.334	0.459	0.422	0.399
Average	0.383	0.338	0.438	0.426	0.415
AASHTO DFs	0.286	0.601	0.601	0.601	0.609

5 Conclusions

As a newly built structure, the Hampden Grist Mill Bridge offered a unique opportunity to capture data from before, during, and after construction. These data can act as a baseline for future load tests conducted to identify long-term deterioration or damage. However, as the first of its kind in the nation, these data can also be used to inform the design, manufacture, and construction of

future CT girder bridges. Through observation of manufacturing and construction, challenges that arose were identified that can be avoided or fixed during future design and construction.

The amount of time and effort used in form design and manufacture, layup, and defect repair show that standardization is important for the CT girder bridges' future economic viability. One way to mitigate these costs would be the creation of a catalog of standard-sized girders laid on standardized molds, or adjustable molds for semi-bespoke girders, thus reducing this effort on each bridge. Additional methods of cambering girders for specific geometries might also be required, and cambering techniques that employ girder self-weight, post-tensioning, or application of external loads during deck casting are worthy of exploration. Additionally, the time taken for manufacture of each girder and the defects found on each highlight the need for more efficient, standardized manufacturing processes to be put into place. From observations of construction of the HGMB, it can be concluded that the CT girder system is well suited to the construction practices used for conventional superstructures. Neglecting the extenuating circumstances of the project due to the COVID-19 global pandemic and resulting delays, construction of the superstructure proceeded rapidly and without incident. The construction contractor worked with the system quite efficiently despite its novelty. This suggests that the CT girder can easily replace conventional superstructures with little change or special consideration on the construction side.

The results of live-load testing indicate that the HGMB specifically, and perhaps CT-girder superstructure bridges in general, behave differently from equivalent, conventional superstructure bridges. This leads to some particular conclusions that highlight these differences. First, as evidenced by the girders' inferred neutral axis heights and flexural rigidities, the HGMB's CT girders are much stiffer than theoretical analysis would suggest. The high, inferred flexural rigidities cannot be attributed to one specific cause such as a higher-modulus FRP girder or deck. However, the higher-than-expected neutral axis heights would tend to suggest that the stiffness of the deck relative to the girder is higher than expected.

The second conclusion drawn from live-load testing and subsequent analysis is that distribution factor formulae should be developed for these girders that mimic those presented by AASHTO [3] for other superstructure types. The GLFs calculated from recorded strains and inferred, corrected flexural rigidities are not DFs in the strictest sense. However, because multiple live-load tests were conducted with trucks placed at various transverse positions across the deck, they tend to envelope the "worst-case" loadings required for DFs and thus the highest GLF from a particular girder from any test can be considered its effective DF. Using this distinction, it is clear that the DFs used in design (those presented by AASHTO for precast concrete box girders with concrete deck) can lead to un-conservative results. For interior girders, the highest calculated GLF was 0.638, compared with the design DF of 0.601 and an error of 6.2%. For exterior girders, Girder 1 in particular, the highest calculated GLF was 0.420, compared with the design value of 0.286 at an error of 46.9%. Further study is required involving both physical and numerical testing, which can lead to a set of DF formulae that maintain the conservatism and reliability required in design.

Finally, the existence of significant, unexpected girder end fixity highlights the need for continued monitoring of the HGMB to assess the continued presence of this partial fixity. Throughout design, construction, and test planning, it was assumed that the CT girders used on the HGMB would behave much more like simply-supported beams with minimal end fixity. For this reason, only a small portion of the sensing resources were allocated to girder ends during live-load testing, leaving the nature of this fixity an uncertainty. Better understanding of the HGMB specifically, and CT girder bridges in general, justifies additional monitoring of this phenomenon to more accurately locate its cause, determine if it will be maintained over the bridge's life, and whether it should be expected from other CT-girder bridges. Further monitoring may also reveal other behavioral phenomena, which can also help more fully characterize CT girder bridges' behavior.

From the results of finite element analysis of models of the HGMB some additional conclusions to be drawn. The addition of coupled spring elements at the girders' ends significantly improved the prediction of strains both at midspan and at girder ends and was much more effective than the addition of single spring elements at girder bottoms alone. This suggests that the rotational fixity measured during live-load testing and which could not be attributed to restraint by the integral backwall is more likely a result of interaction with backfill behind the backwall and/or the approach slab than rotational or translational restraint at the bearings. Different details could help eliminate the unintended rotational fixity in future bridges and additional experimental and numerical study can help to better characterize it if it is to be relied upon in future analyses.

Finally, the significant differences between measured and FE analysis-predicted load distribution points further to a complicated transverse load behavior warranting additional detailed investigation. As was mentioned above, the FE-predicted load distribution was much more uniform than was inferred from live-load testing, with the difference between the highest and lowest average GLF being only 30%. This is in contrast to the actual, measured load distribution in which load was less evenly distributed to the interior girders, with girders closer to the load seeing more load and a difference between maximum and minimum average GLF of over 150%. As the FE models encapsulated many of the factors traditionally considered to affect load distribution (skew, cross-slope, deck reinforcement, non-structural elements, etc.) and predicted longitudinal strains relatively accurately, it would seem that further investigation is required. This investigation will not only help in increasing understanding of CT girder bridges' behavior, but also help inform the creation of distribution factor formulae for future design.

6 References

1. Diba, A. (2021, In Progress). *Design, Fabrication, and Testing of Optimized Hybrid Composite-Concrete Bridge Girder System*. Master's Thesis, University of Maine, Orono, ME.

2. Diba, A. & Hepler I. (2019). *Milestone 12: Structural testing of first prototype*. University of Maine, Orono, ME.
3. AASHTO (2012). *LRFD Bridge Design Specifications*. Washington, DC: AASHTO.
4. AASHTO (2012). *LRFD Guide Specifications for Design of Concrete-Filled FRP Tubes for Flexural and Axial Members*. Washington, D.C: AASHTO.
5. AASHTO (2012). *Guide Specifications for Design of Bonded FRP Systems for Repair and Strengthening of Concrete Bridge Elements*. Washington, D.C: AASHTO.
6. AASHTO (2011). *The Manual for Bridge Evaluation*. Washington, DC: AASHTO.
7. Schanck A.P. & Davids, W.G. (2020). Capacity assessment of older t-beam bridges by nonlinear proxy finite element analysis. *Structures*. 23(2020): 267-278.
8. Schanck, A. & Davids, W. (2020). *Field Live-Load Testing and Advanced Analysis of Concrete T-Beam Bridges to Extend Service Life*. University of Maine, Orono, ME.
9. Bridge Diagnostics Inc. (2010). *Wireless structural testing system STS-WiFi operations manual*. Boulder, CO.: BDI.
10. MathWorks (2018). *MATLAB R2016a* [Computer software]. MathWorks: Natick, MA.
11. *ABAQUS 6.13* [Computer software]. Vélizy-Villacoublay, France: Dassault Systèmes.
12. Vectorply. (2015). *E-LR 2410*. Vectorply Corporation, Phenix City, AL.
13. Heathcote, S. (2020). *QC Testing AIT Bridges Hampden Project*. University of Maine, Orono, ME.
14. Lagarias, J.C., Reeds, J.A, Wright, M.H., & Wright P.E. (1998). Convergence properties of the Nelder-Mead simplex method in low dimensions. *SIAM Journal on Optimization*. 9(1): 112-147.
15. Newcomb, D., Timm, D., & Mahoney, J. (2002, June). It's still dirt, rocks, and asphalt – right? *Hot Mix Asphalt Technology*, 7(4), 16-22.

A.1 Live-Load Test Strain Histories

A.1.1 SBS_2_1

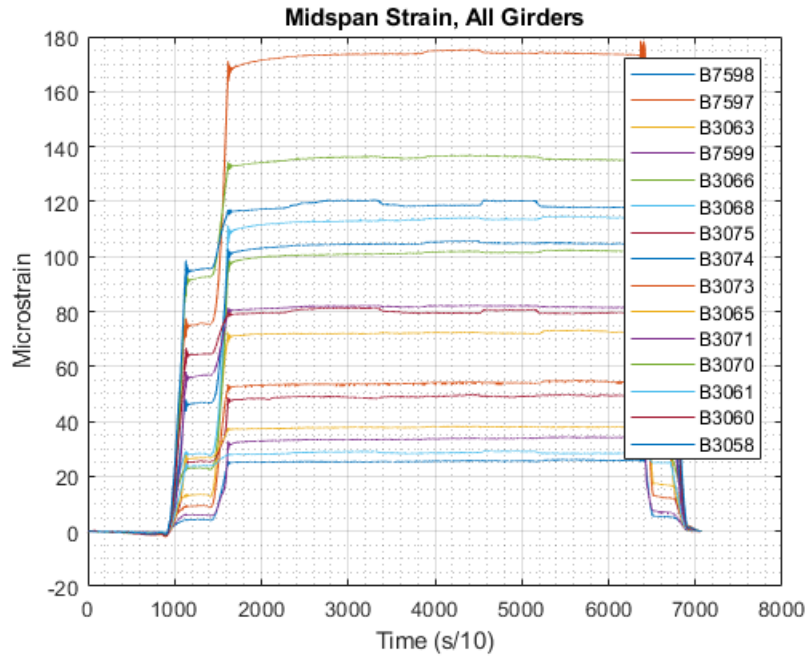


Figure A-1: SBS_2_1 All Midspan Strains

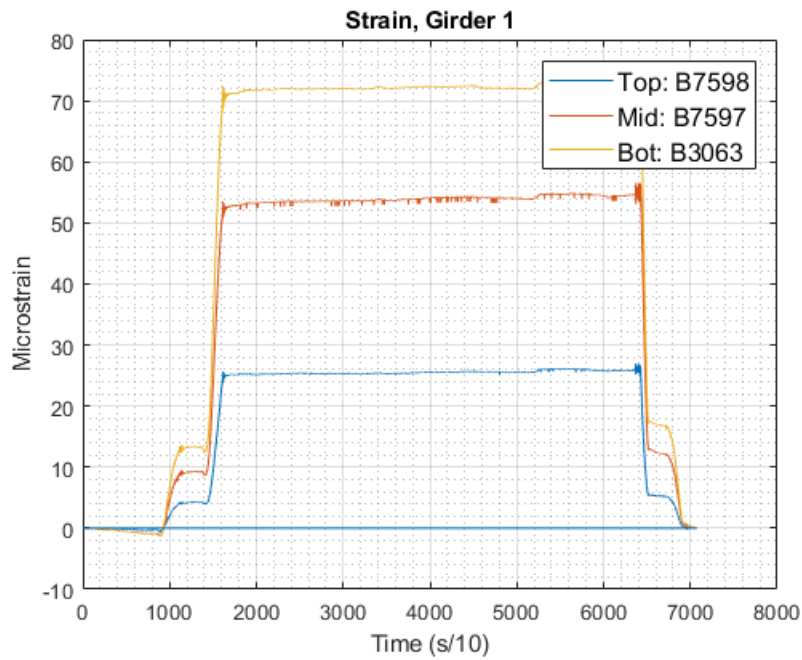


Figure A-2: SBS_2_1 Midspan Strains, Girder 1

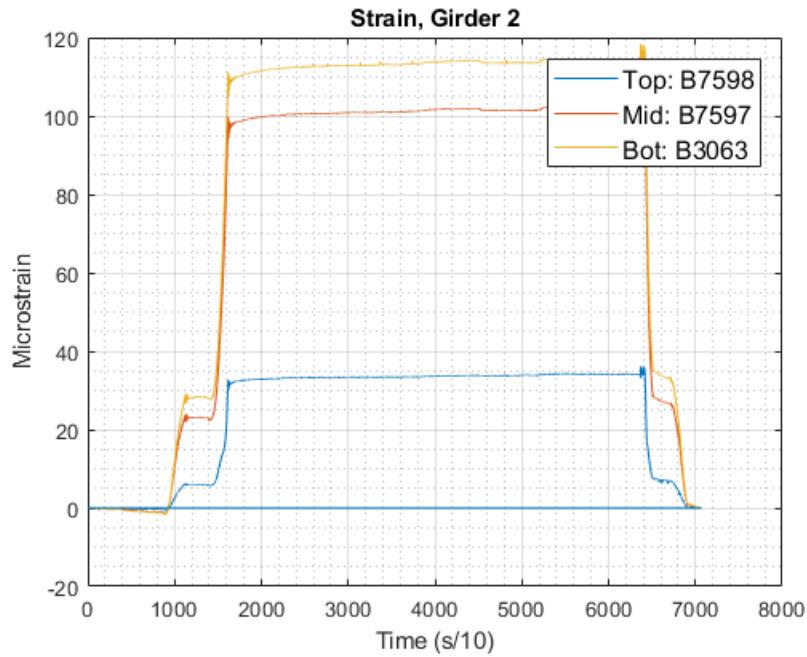


Figure A-3: SBS_2_1 Midspan Strains, Girder 2

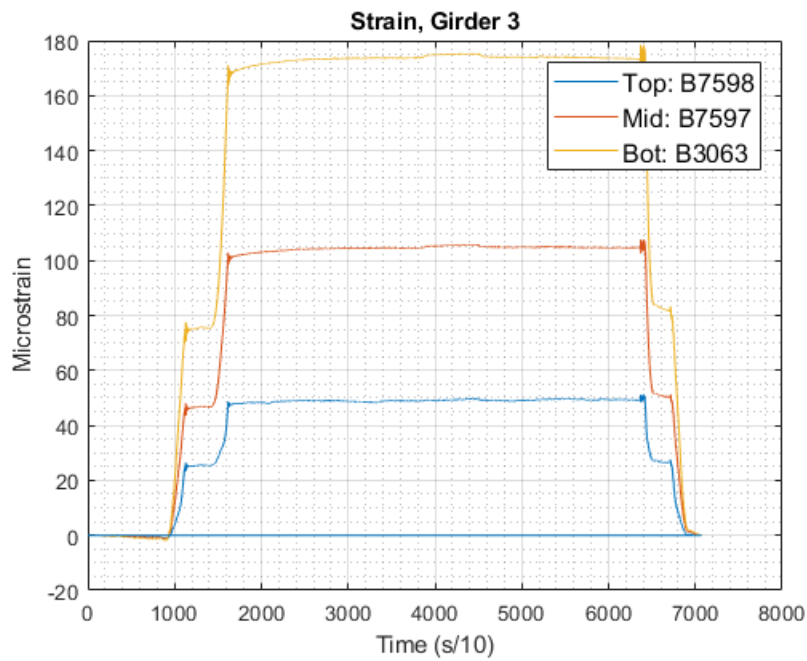


Figure A-4: SBS_2_1 Midspan Strains, Girder 3

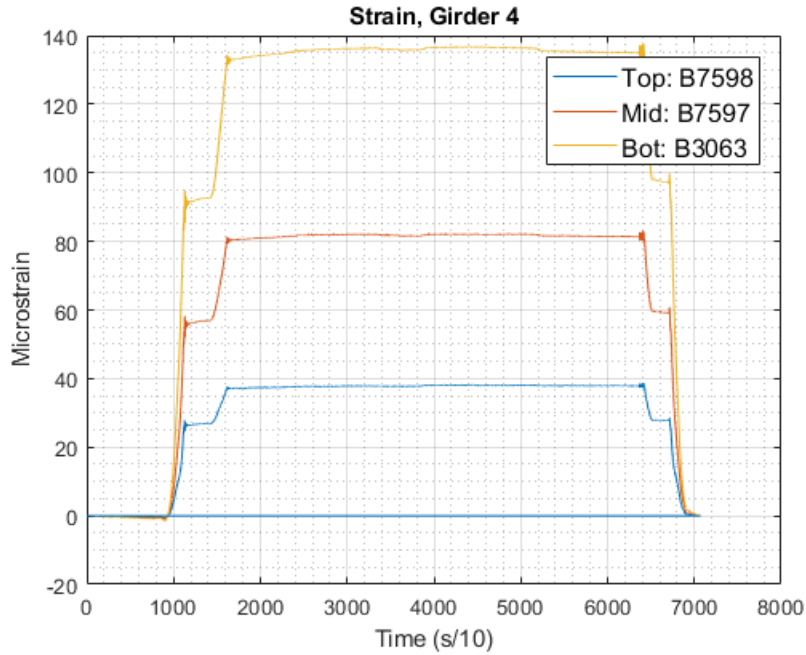


Figure A-5: SBS_2_1 Midspan Strains, Girder 4

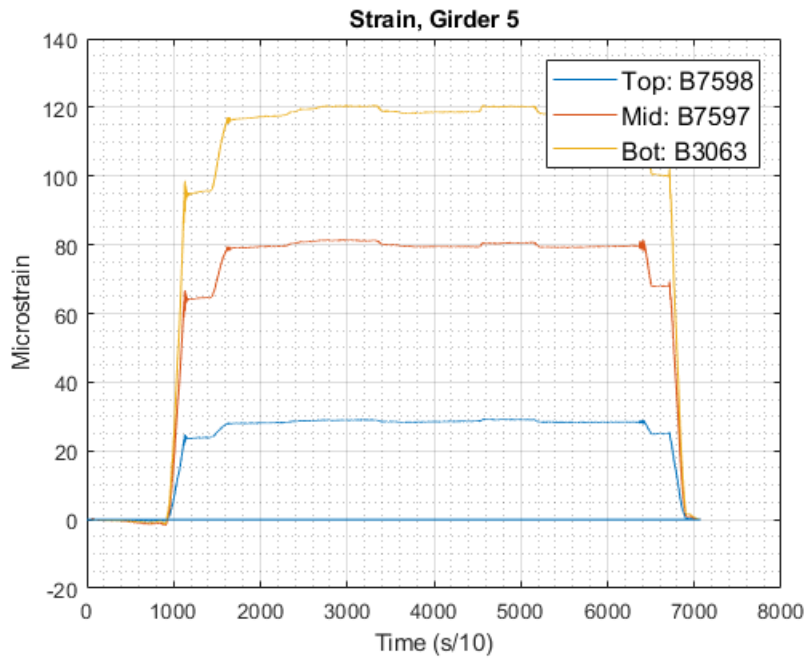


Figure A-6: SBS_2_1 Midspan Strains, Girder 5

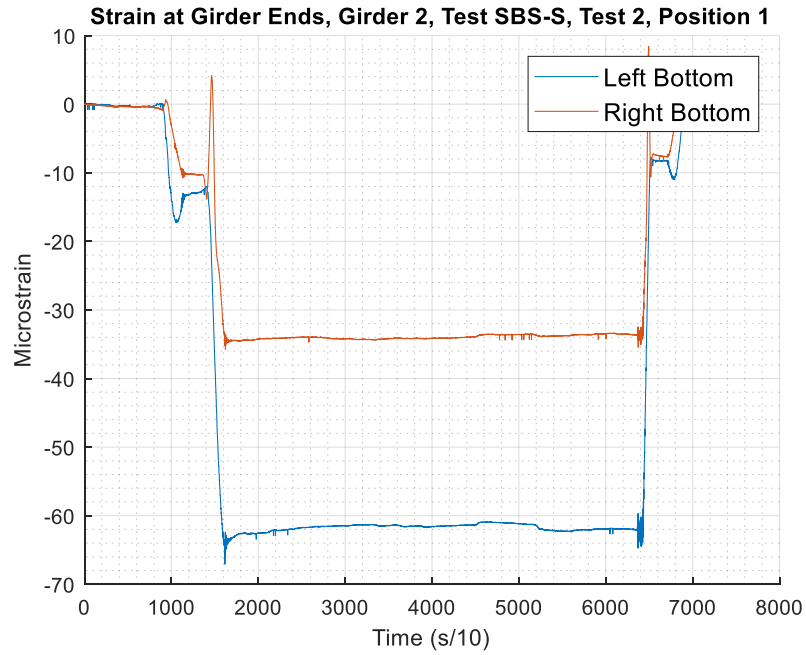


Figure A-7: SBS_2_1 Girder 2 End Strains

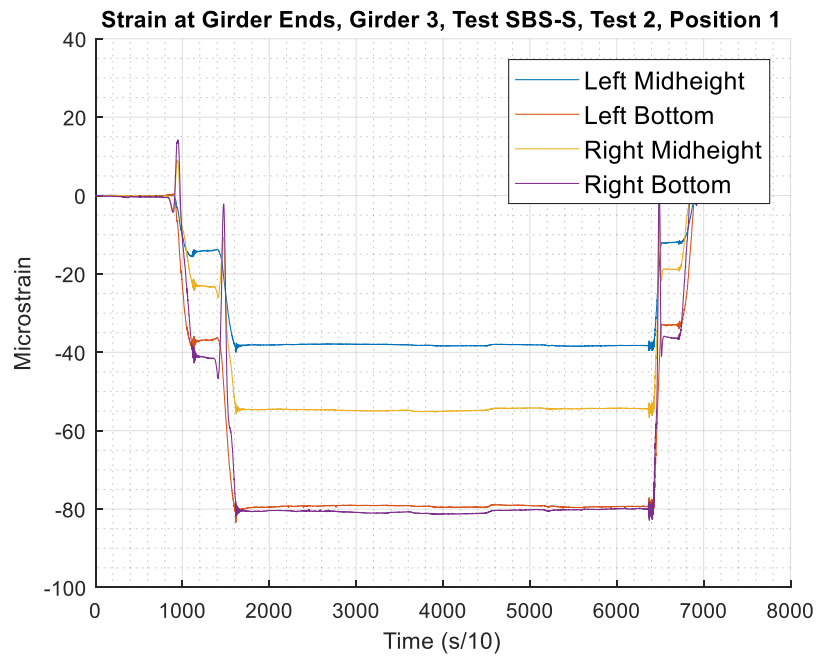


Figure A-8: SBS_2_1 Girder 3 End Strains

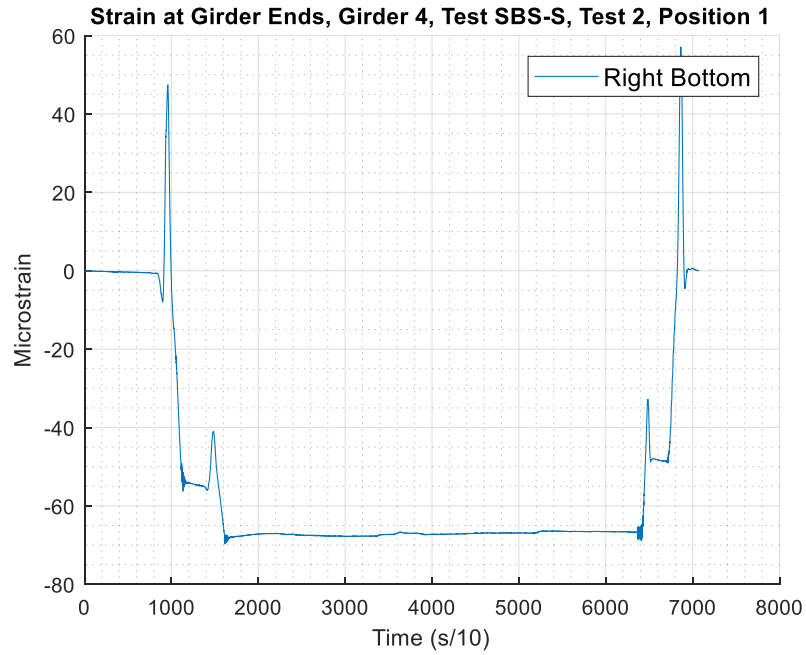


Figure A-9: SBS_2_1 Girder 4 End Strains

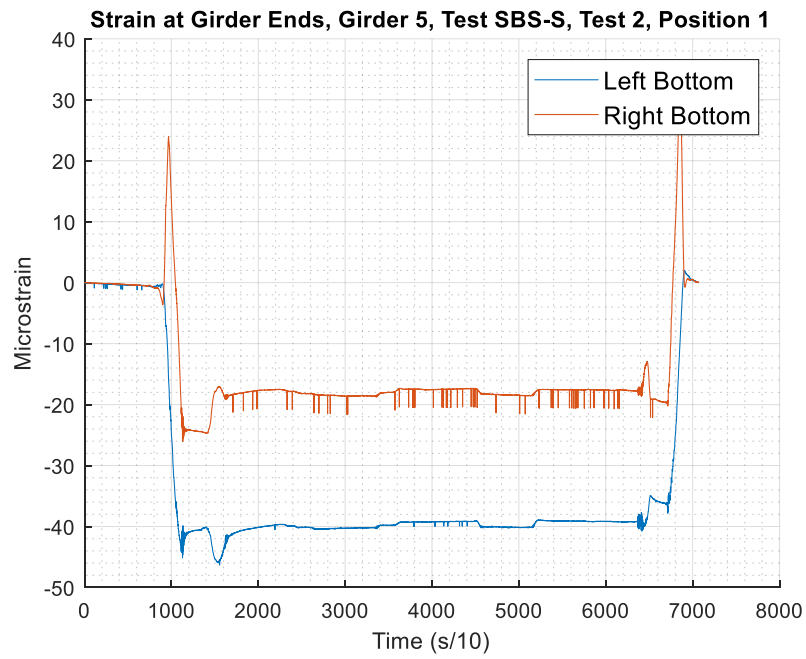


Figure A-10: SBS_2_1 Girder 5 End Strains

A.1.2 SBS_2_2

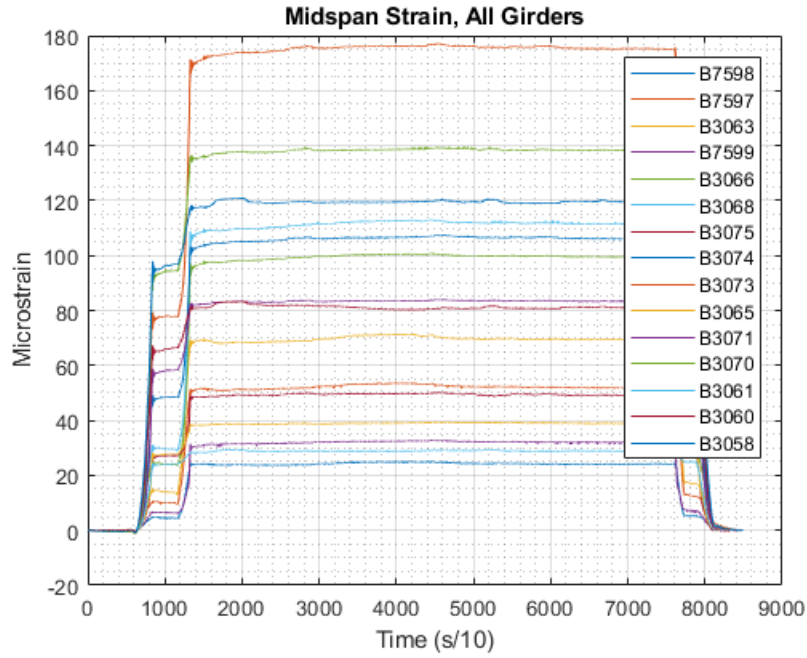


Figure A-11: SBS_2_1 All Midspan Strains

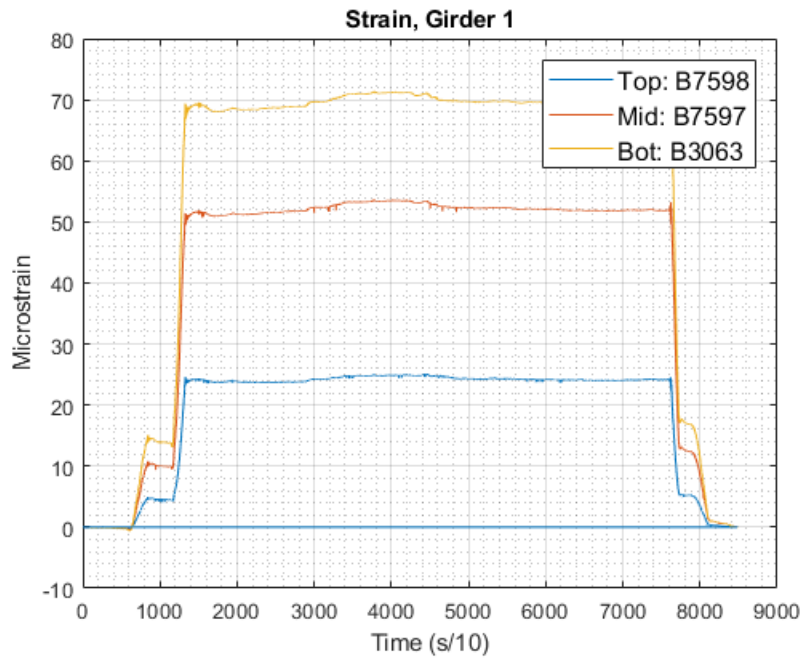


Figure A-12: SBS_2_1 Midspan Strains, Girder 1

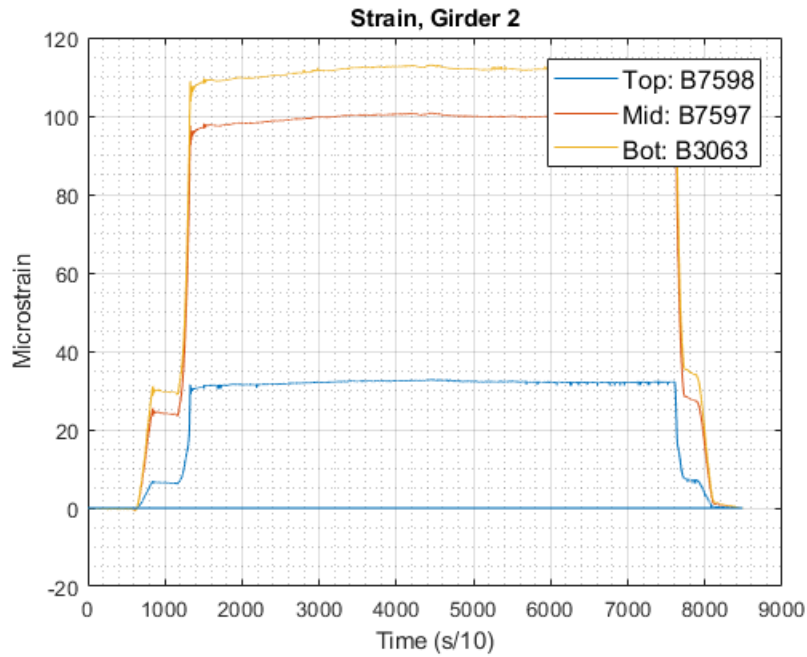


Figure A-13: SBS_2_1 Midspan Strains, Girder 2

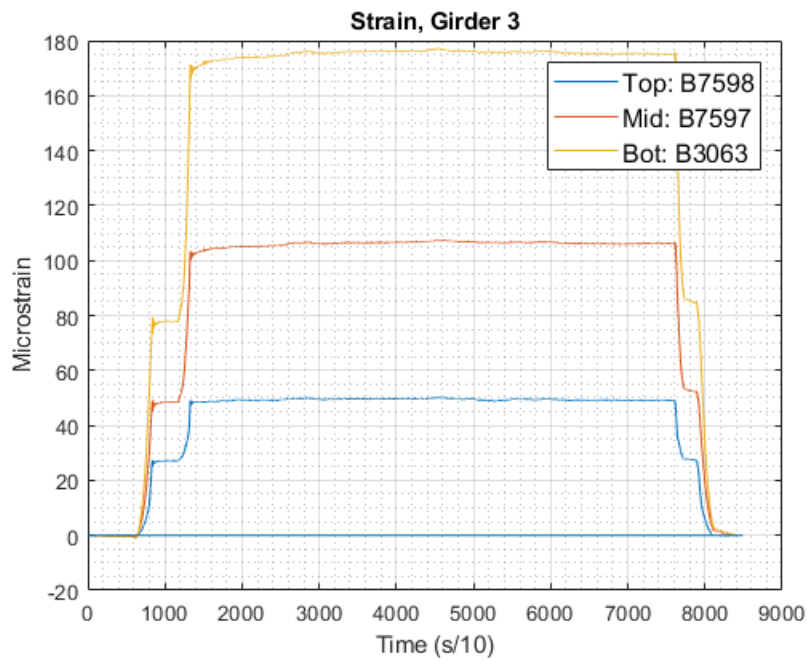


Figure A-14: SBS_2_1 Midspan Strains, Girder 3

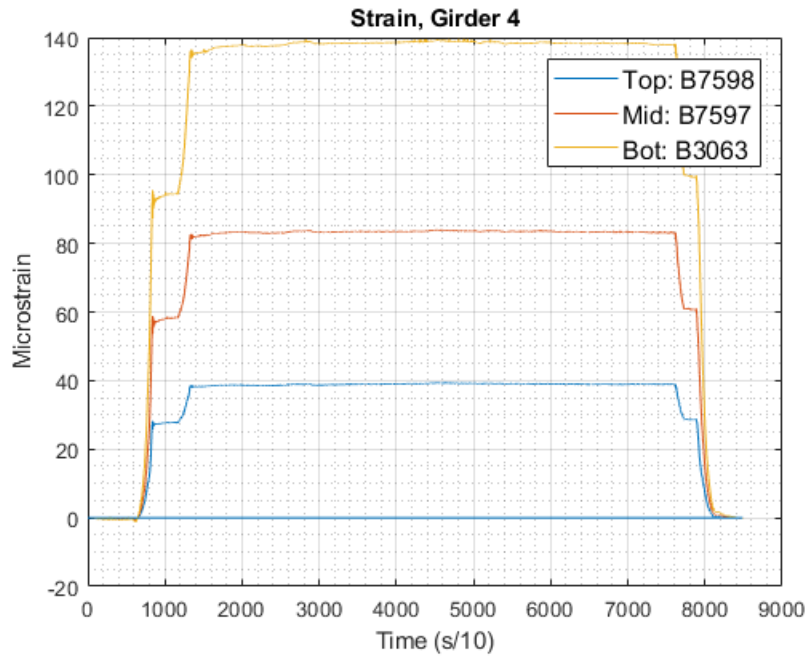


Figure A-15: SBS_2_1 Midspan Strains, Girder 4

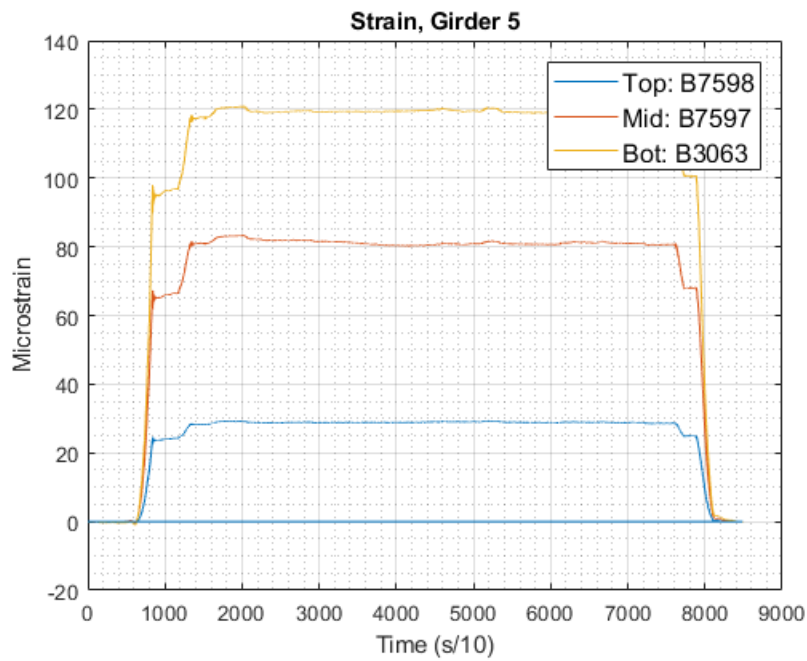


Figure A-16: SBS_2_1 Midspan Strains, Girder 5

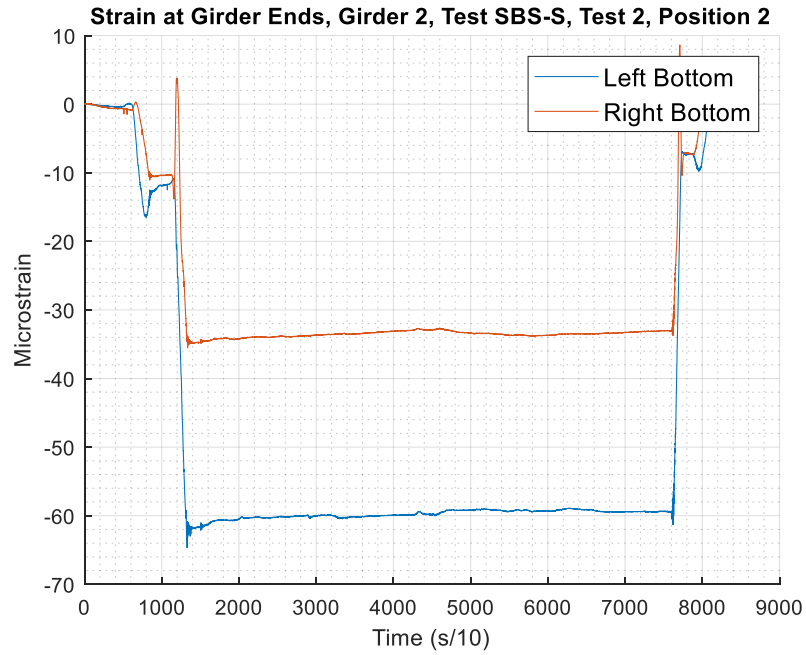


Figure A-17: SBS_2_1 Girder 2 End Strains



Figure A-18: SBS_2_1 Girder 3 End Strains

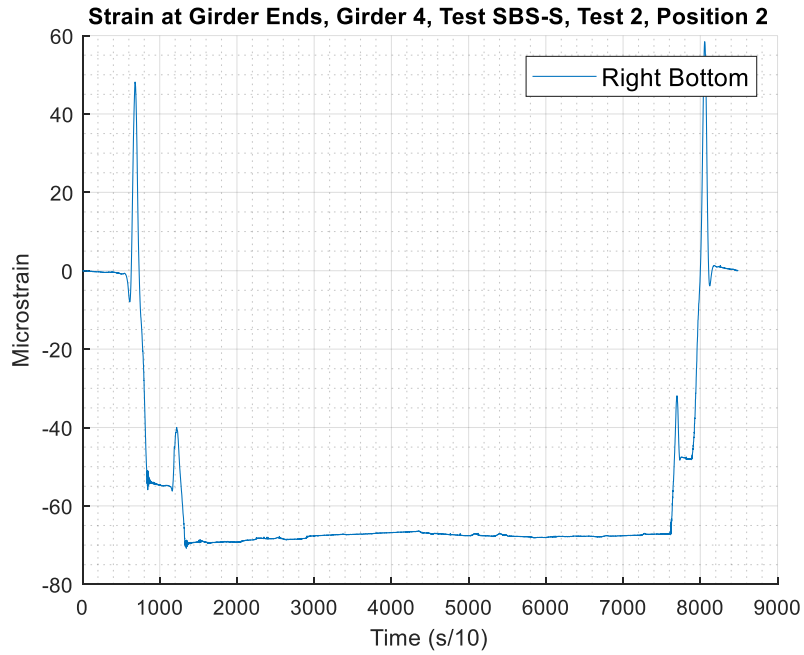


Figure A-19: SBS_2_1 Girder 4 End Strains

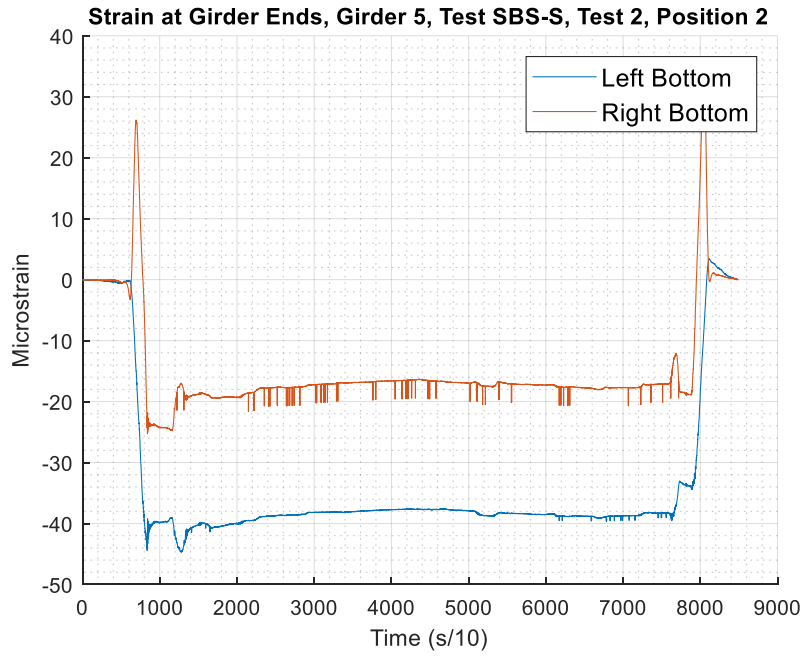


Figure A-20: SBS_2_1 Girder 5 End Strains

A.1.3 MAX_1_1

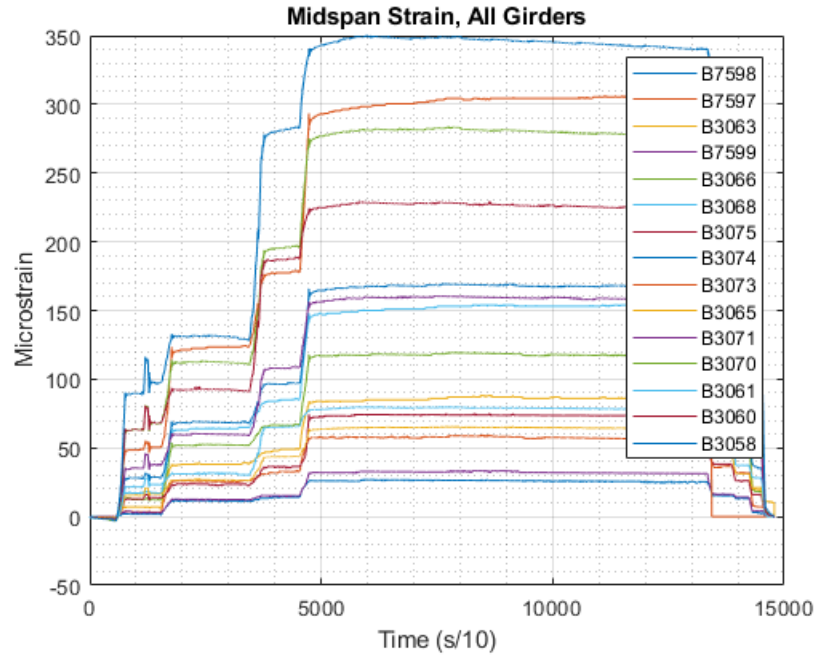


Figure A-21: MAX_1_1 All Midspan Strains

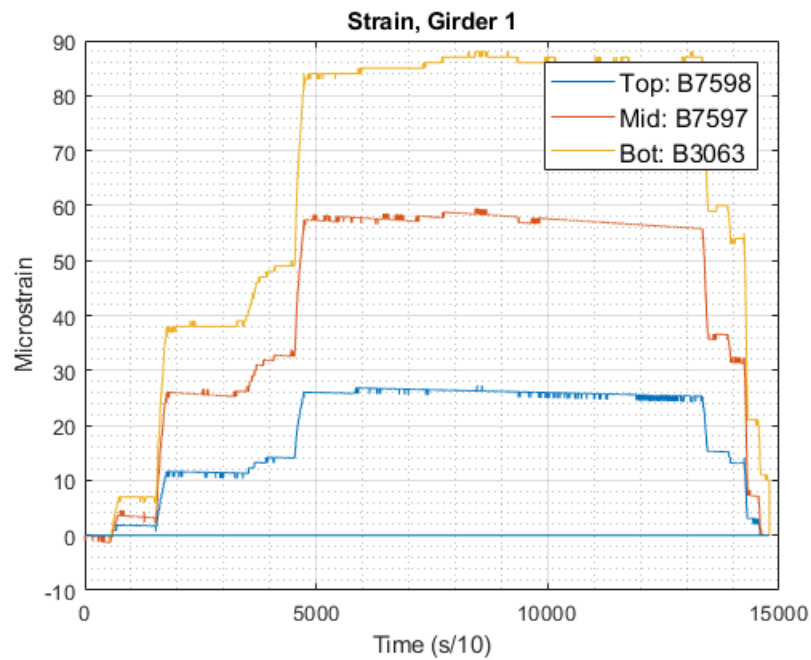


Figure A-22: MAX_1_1 Midspan Strains, Girder 1

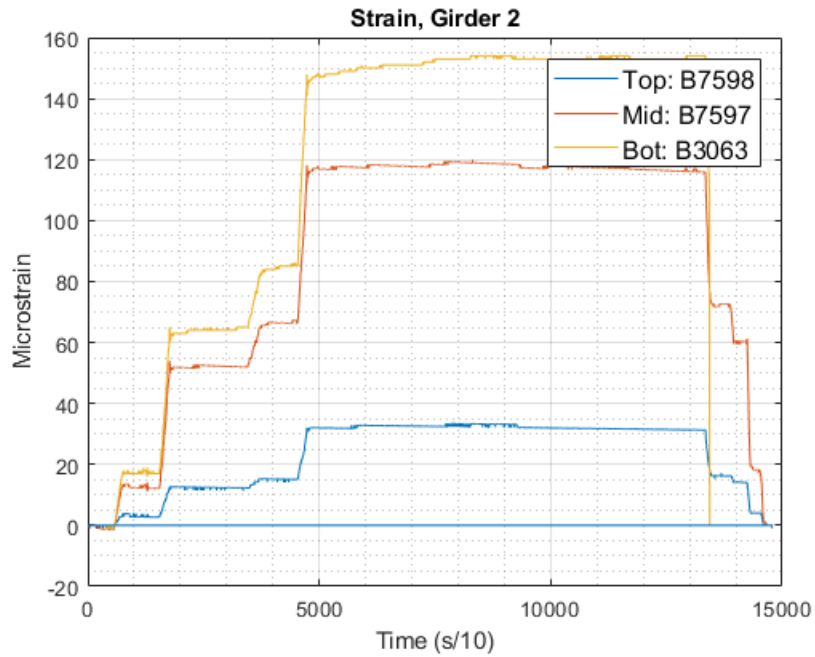


Figure A-23: MAX_1_1 Midspan Strains, Girder 2

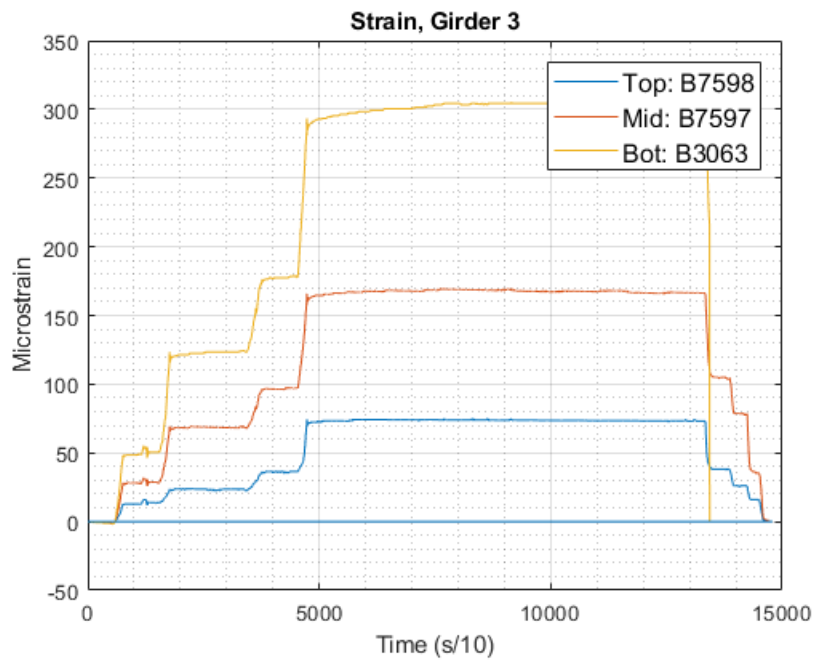


Figure A-24: MAX_1_1 Midspan Strains, Girder 3

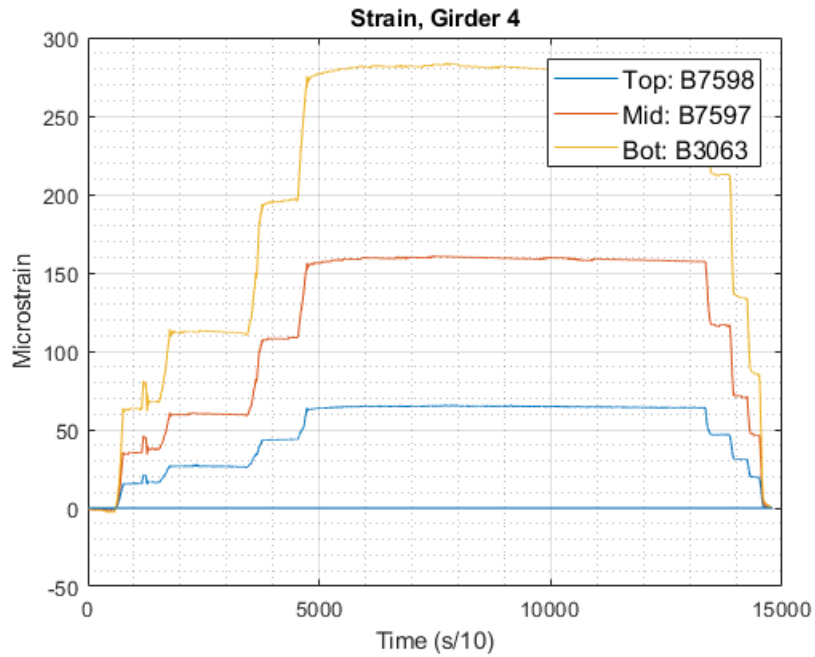


Figure A-25: MAX_1_1 Midspan Strains, Girder 4

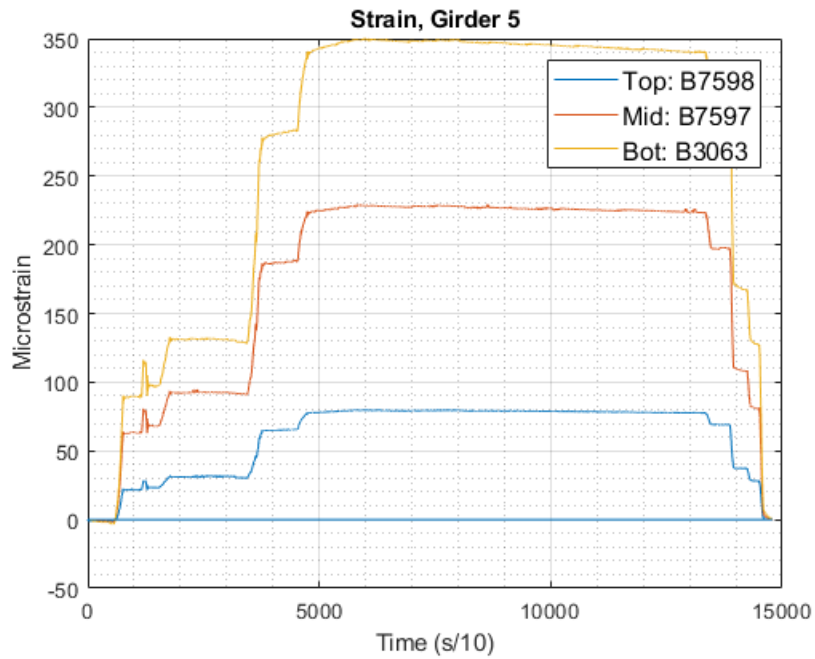


Figure A-26: MAX_1_1 Midspan Strains, Girder 5

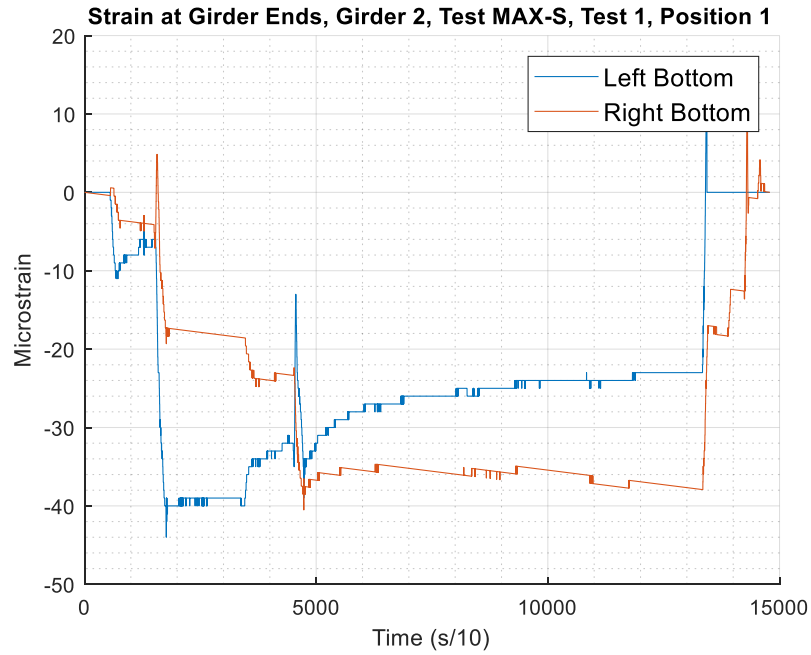


Figure A-27: MAX_1_1 Girder 2 End Strains

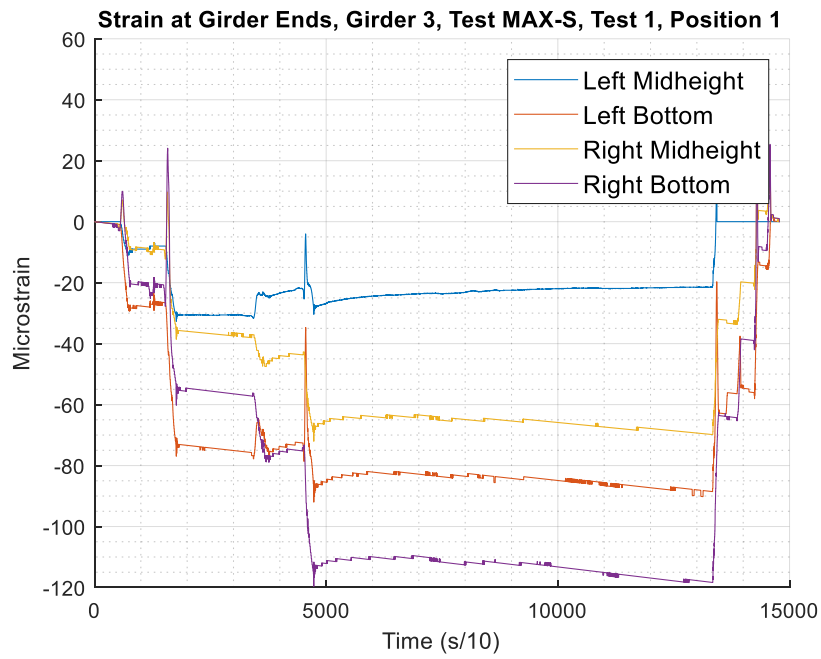


Figure A-28: MAX_1_1 Girder 3 End Strains

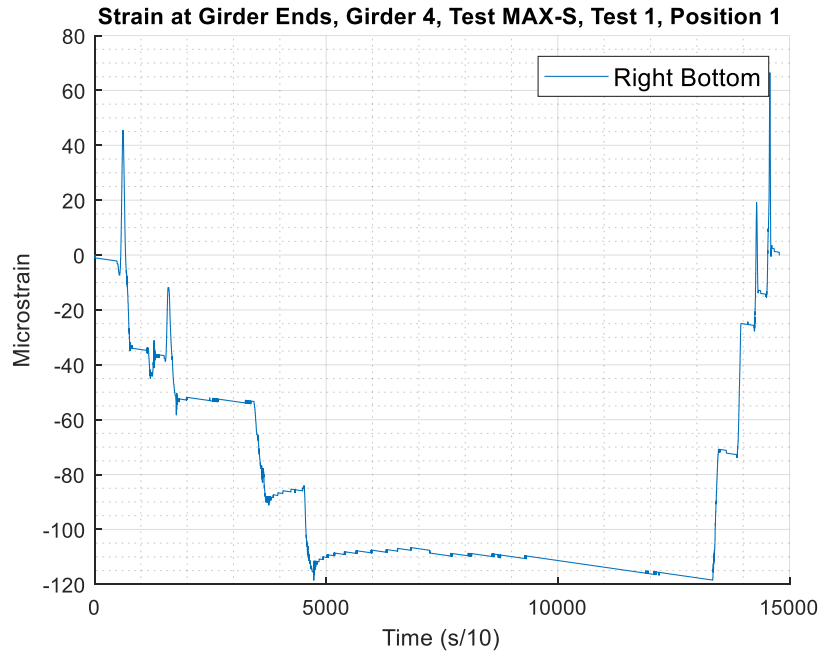


Figure A-29: MAX_1_1 Girder 4 End Strains

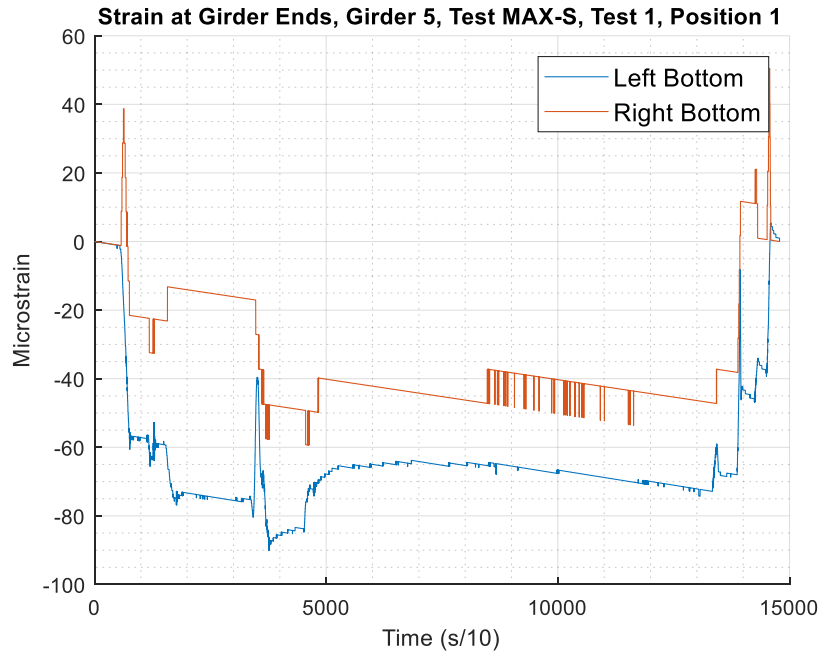


Figure A-30: MAX_1_1 Girder 5 End Strains

A.1.4 MAX_2_1

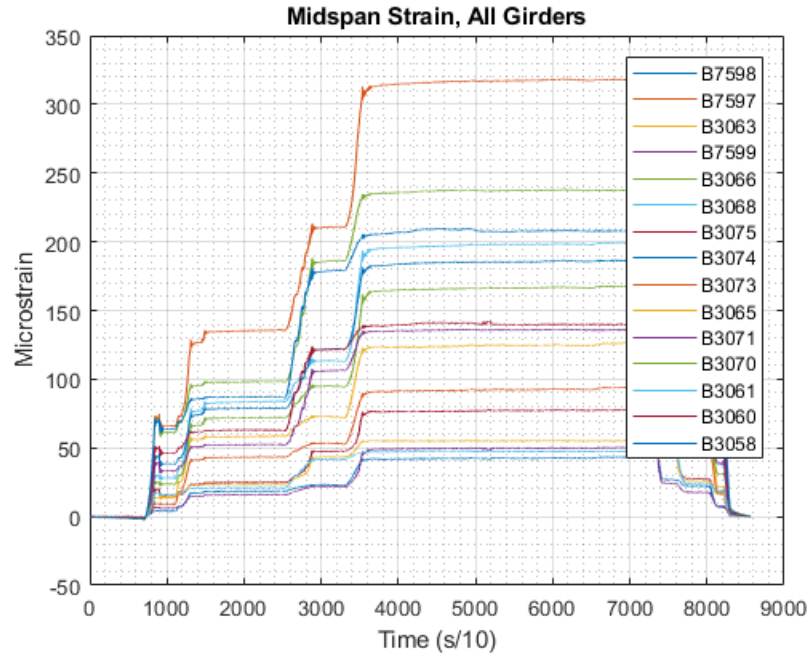


Figure A-31: MAX_2_1 All Midspan Strains

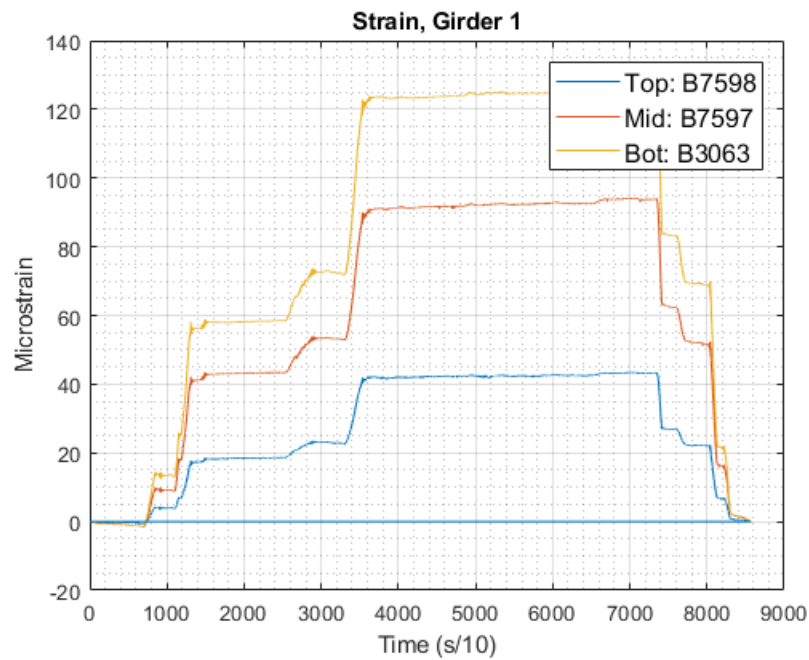


Figure A-32: MAX_2_1 Midspan Strains, Girder 1

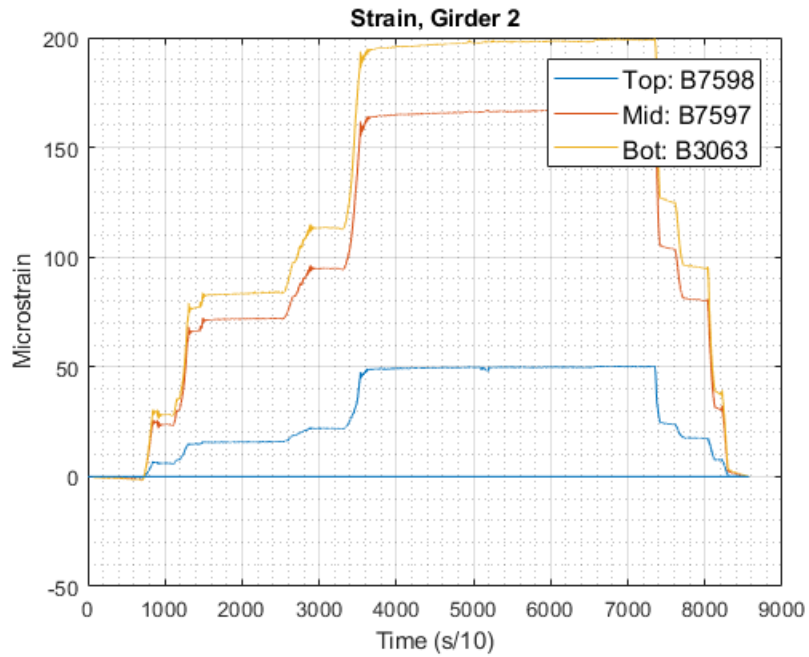


Figure A-33: MAX_2_1 Midspan Strains, Girder 2

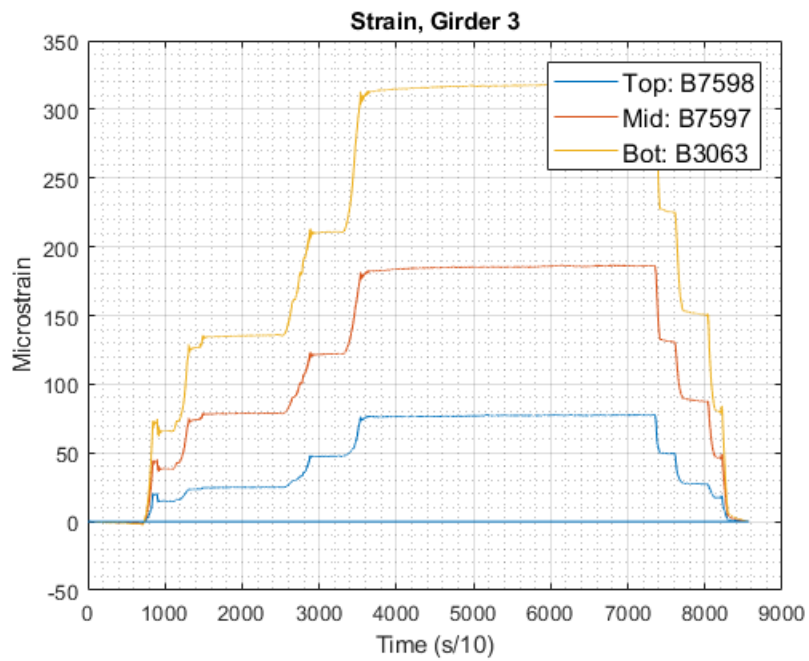


Figure A-34: MAX_2_1 Midspan Strains, Girder 3

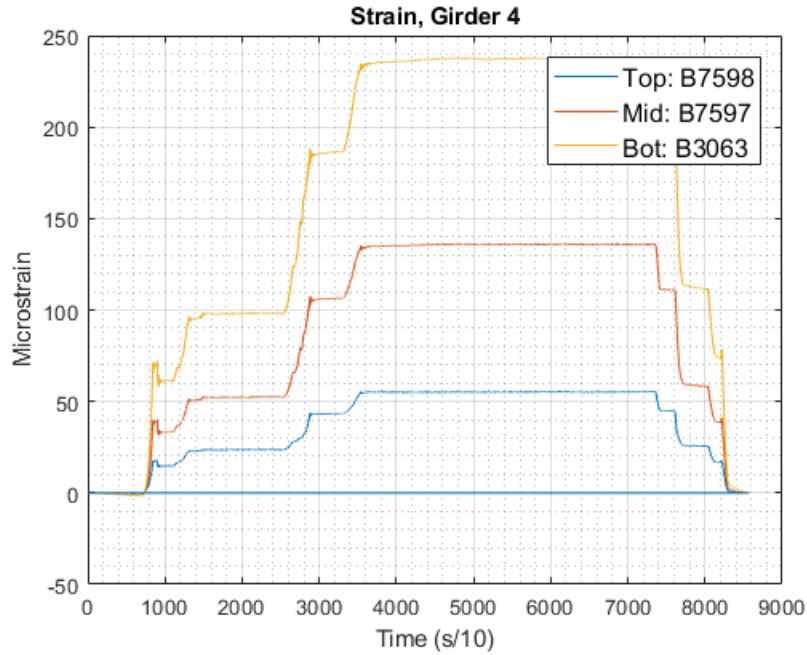


Figure A-35: MAX_2_1 Midspan Strains, Girder 4

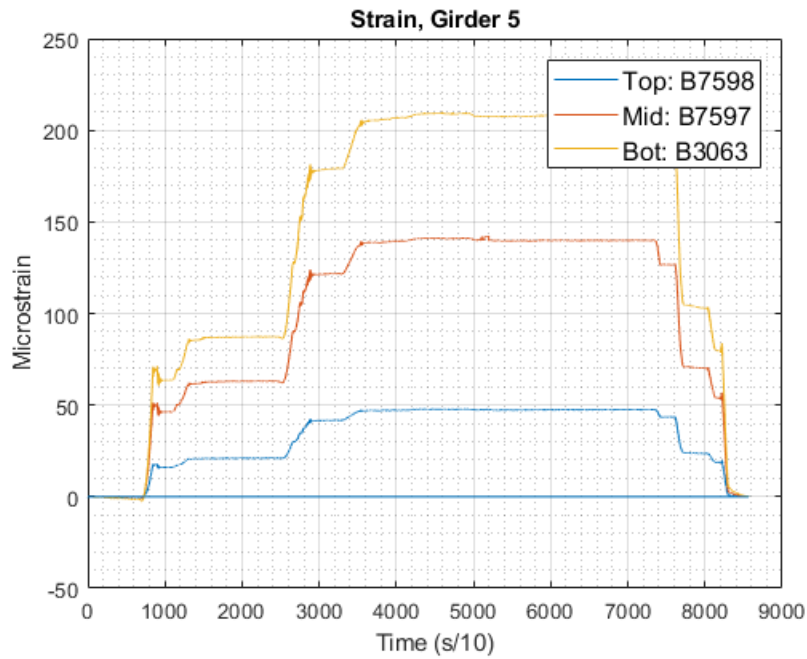


Figure A-36: MAX_2_1 Midspan Strains, Girder 5

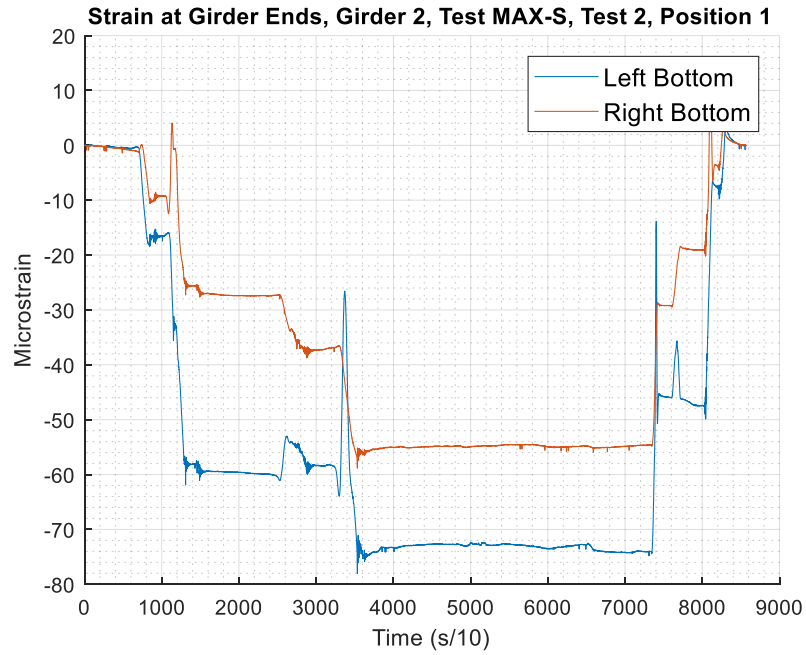


Figure A-37: MAX_2_1 Girder 2 End Strains

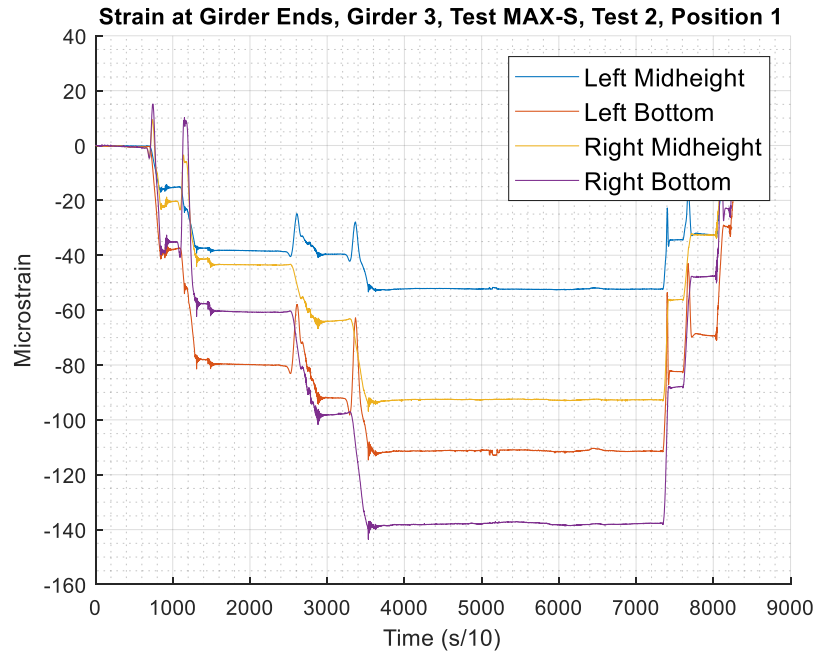


Figure A-38: MAX_2_1 Girder 3 End Strains

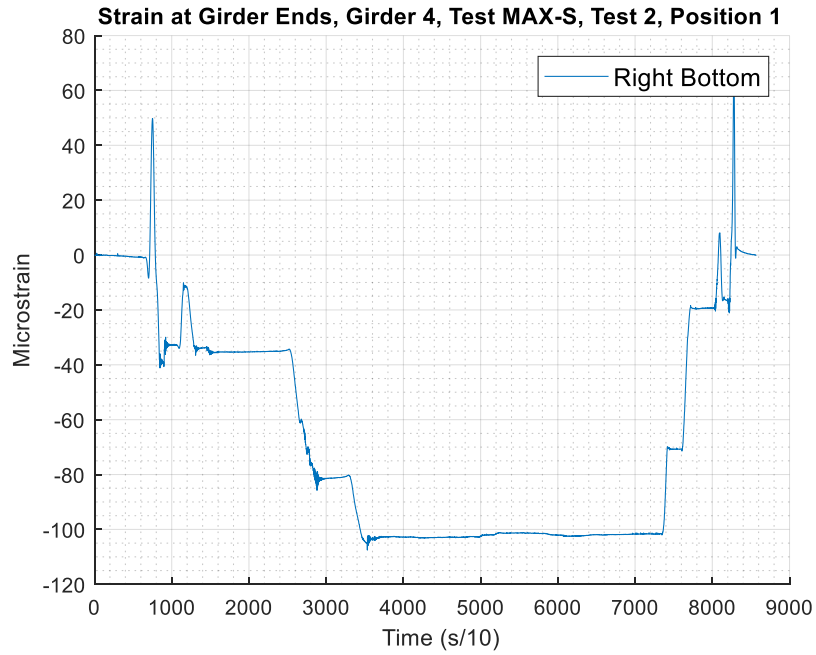


Figure A-39: MAX_2_1 Girder 4 End Strains

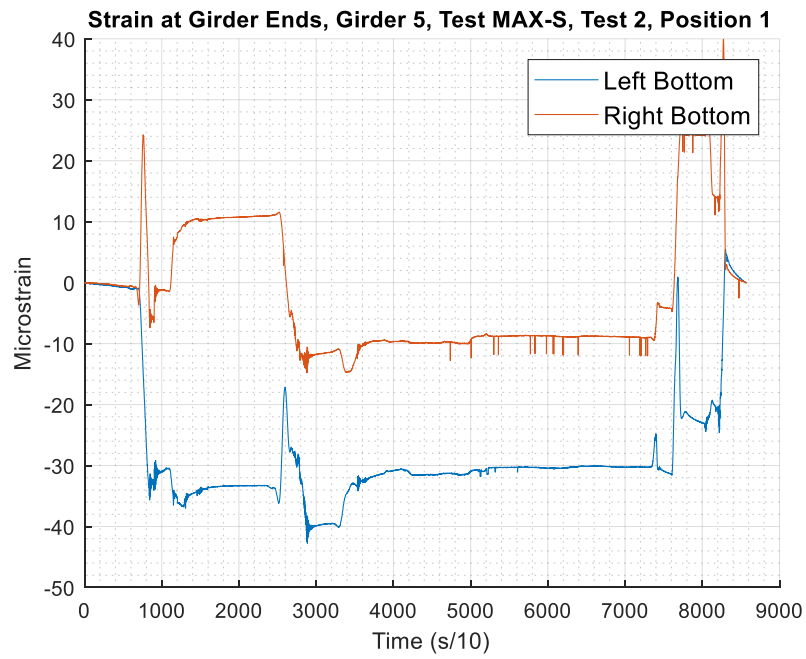


Figure A-40: MAX_2_1 Girder 5 End Strains

A.1.5 MAX_2_2

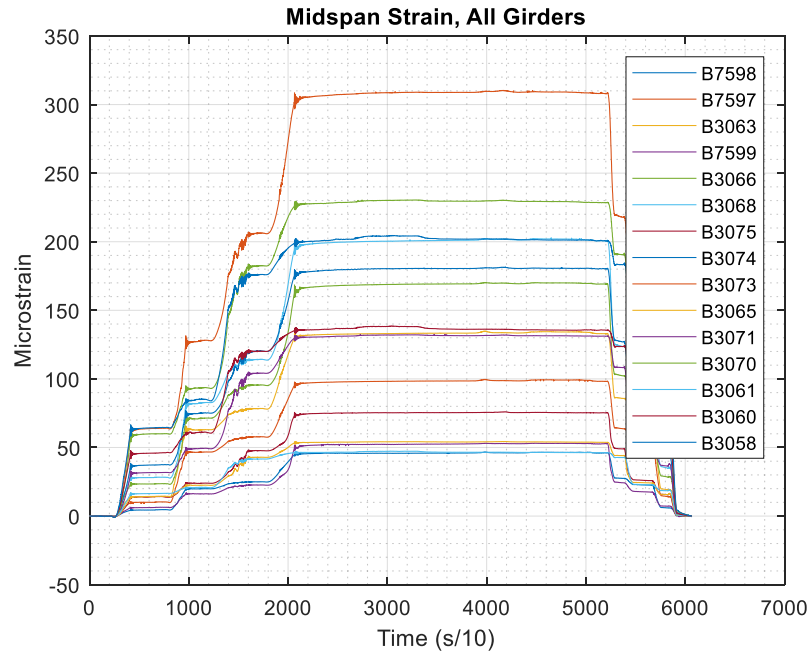


Figure A-41: MAX_2_2 All Midspan Strains

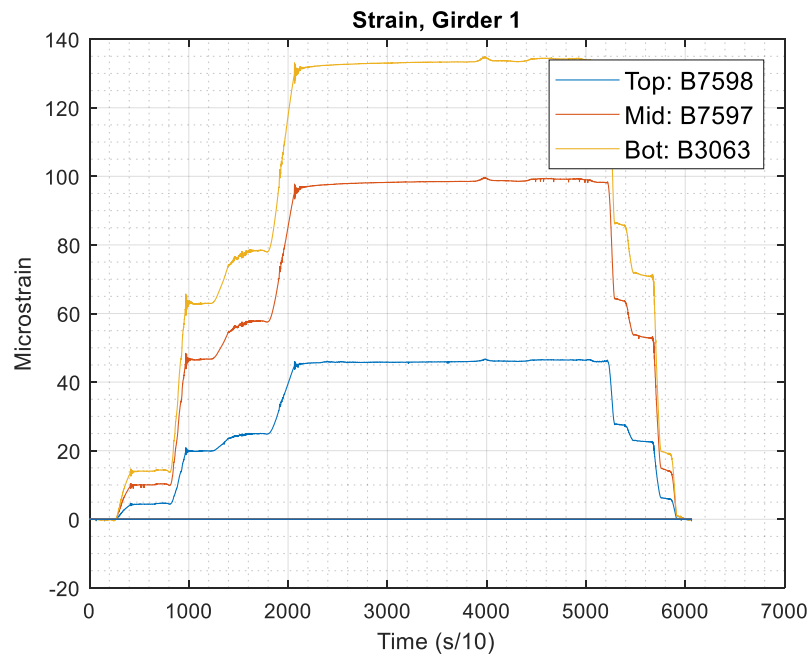


Figure A-42: MAX_2_2 Midspan Strains, Girder 1

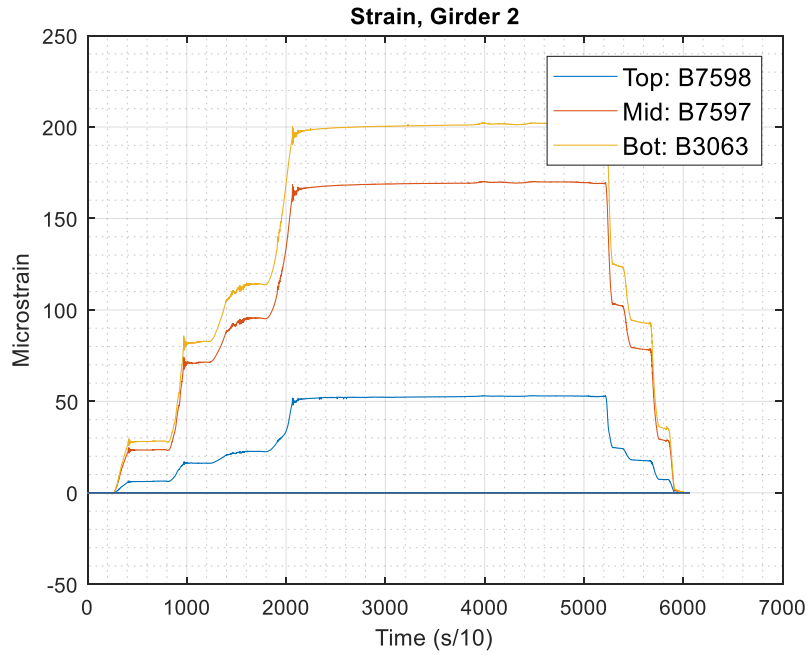


Figure A-43: MAX_2_2 Midspan Strains, Girder 2

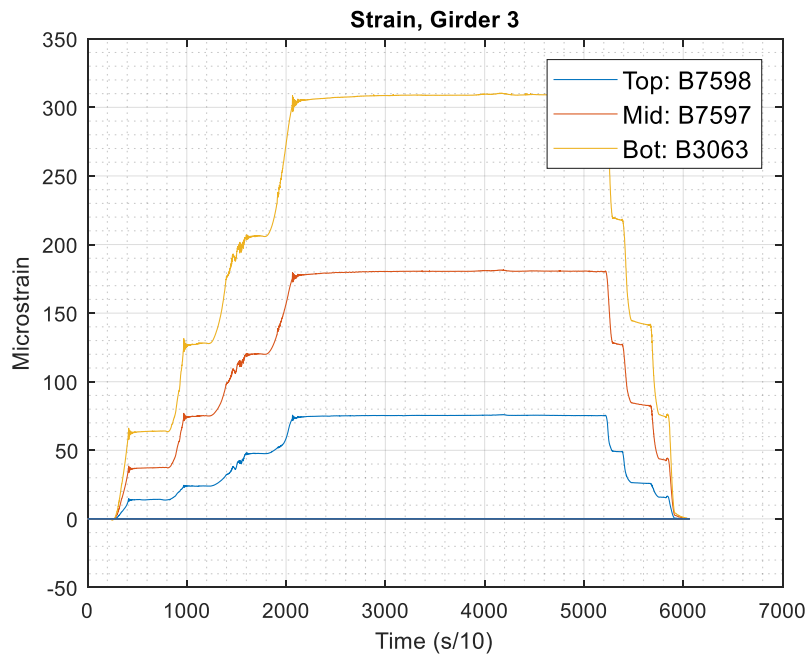


Figure A-44: MAX_2_2 Midspan Strains, Girder 3

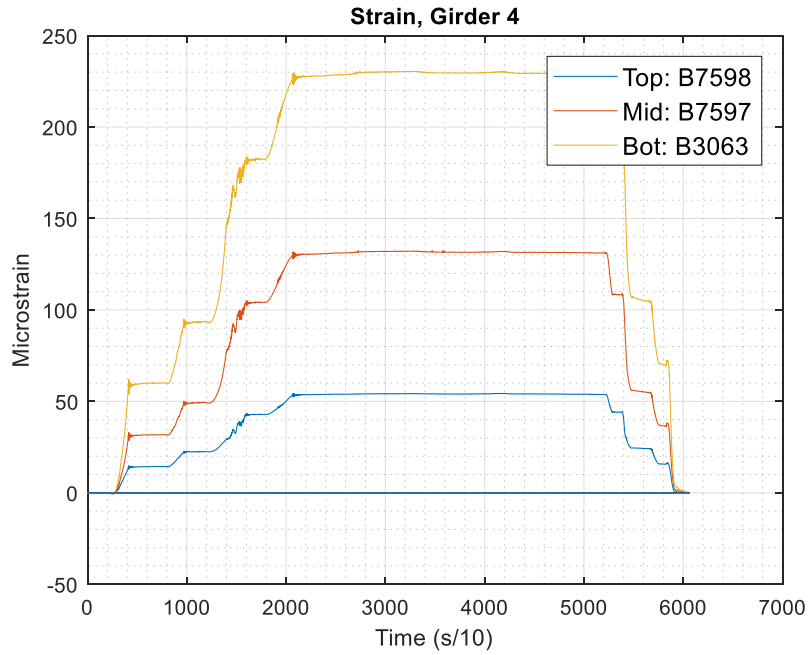


Figure A-45: MAX_2_2 Midspan Strains, Girder 4

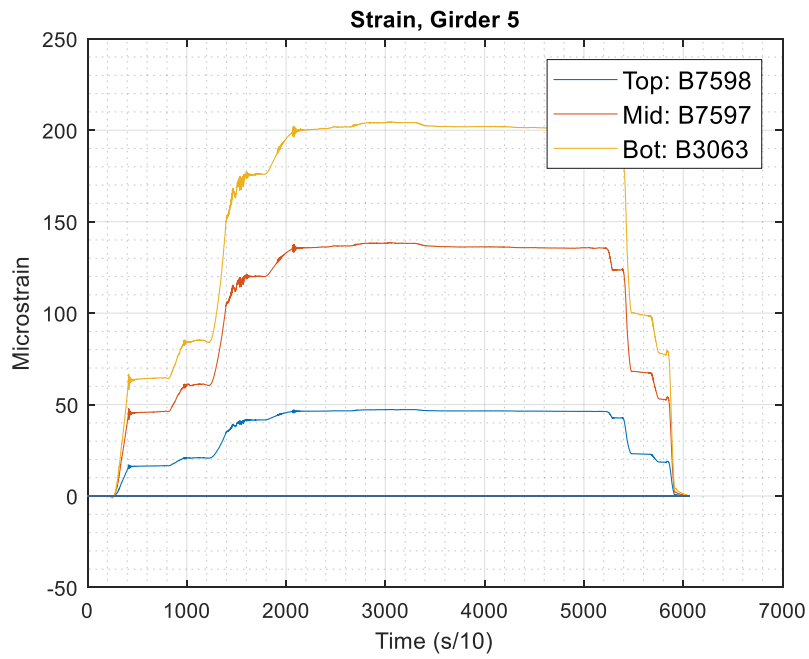


Figure A-46: MAX_2_2 Midspan Strains, Girder 5

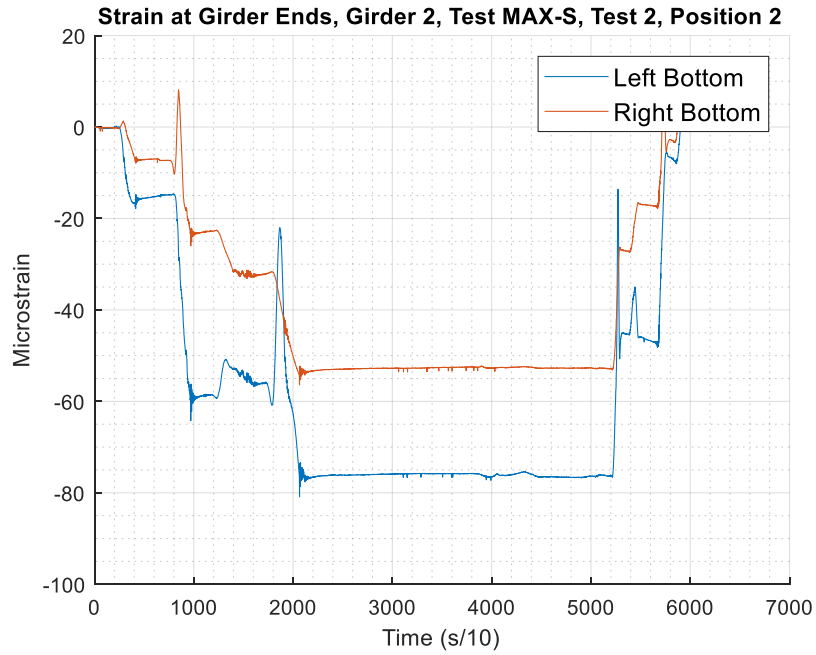


Figure A-47: MAX_2_2 Girder 2 End Strains



Figure A-48: MAX_2_2 Girder 3 End Strains

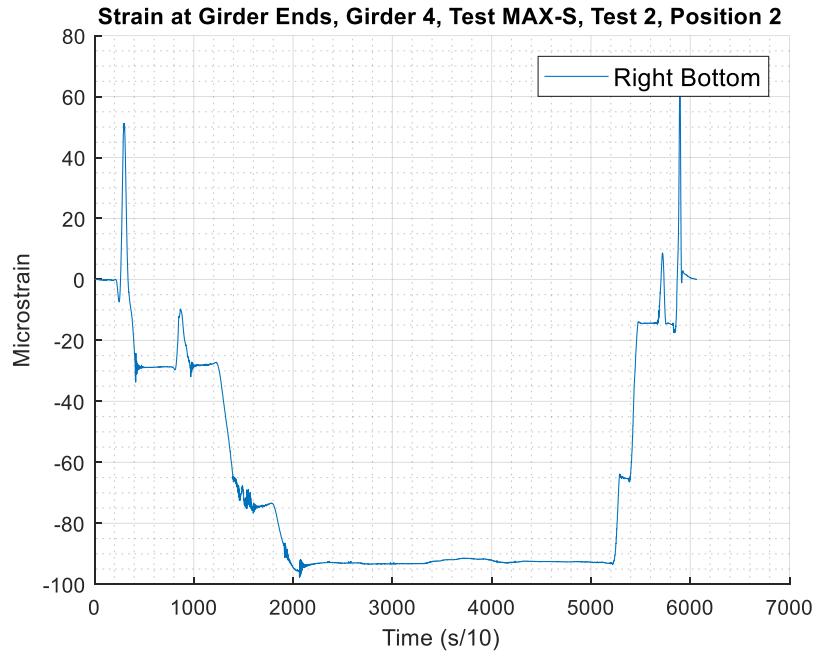


Figure A-59: MAX_2_2 Girder 4 End Strains

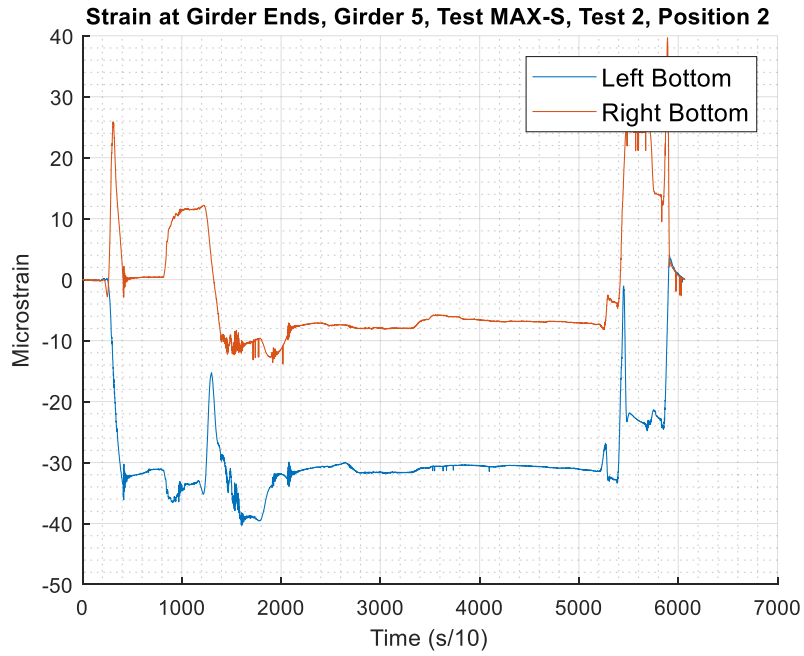


Figure A-50: MAX_2_2 Girder 5 End Strains

A.1.6 MAX_3_1

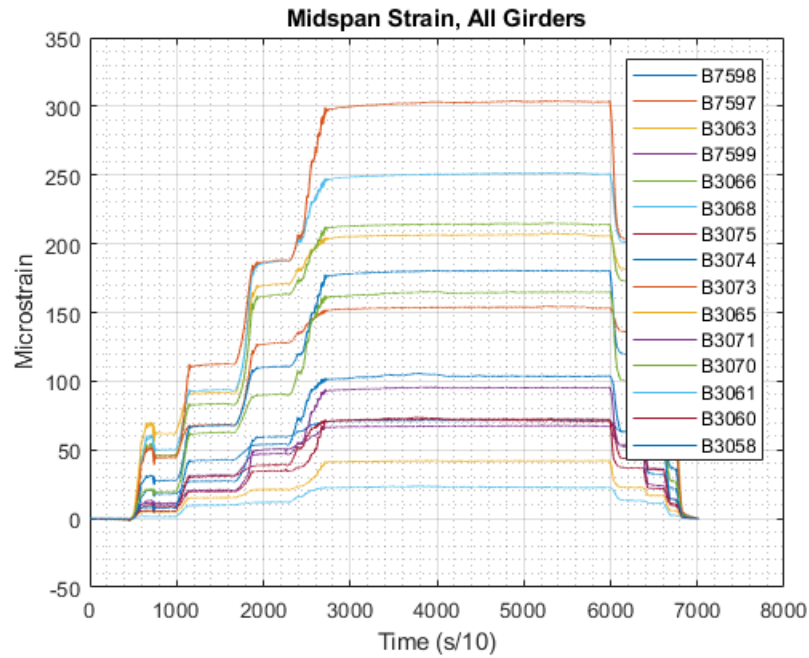


Figure A-51: MAX_3_1 All Midspan Strains

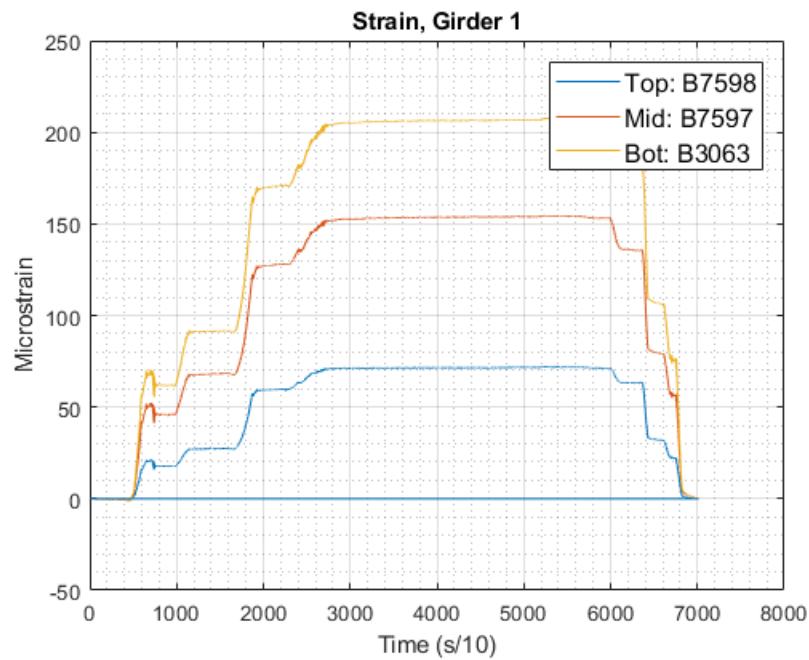


Figure A-52: MAX_3_1 Midspan Strains, Girder 1

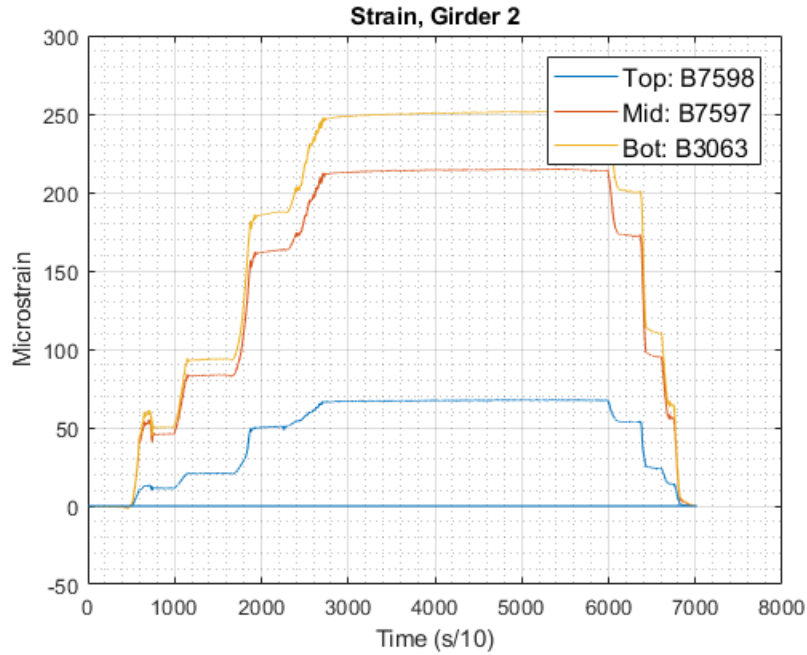


Figure A-53: MAX_3_1 Midspan Strains, Girder 2

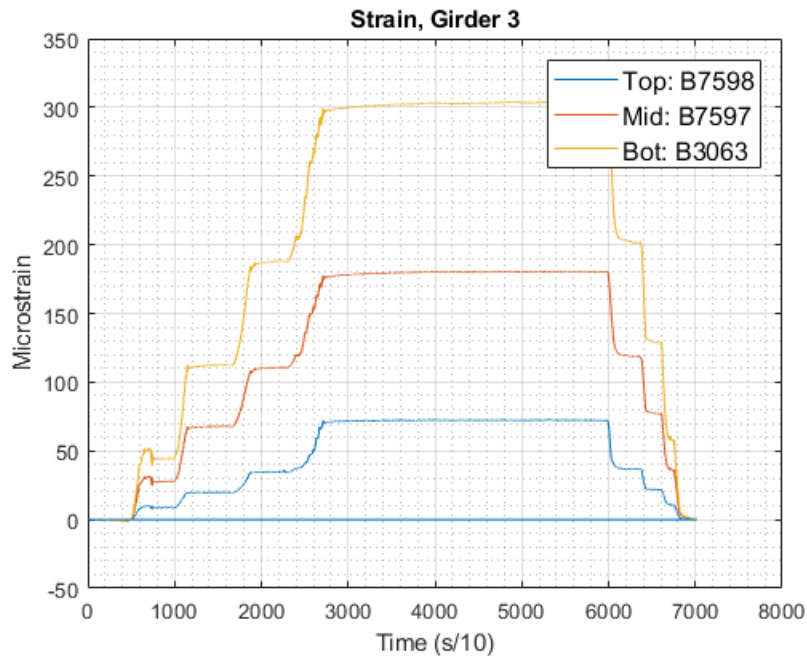


Figure A-54: MAX_3_1 Midspan Strains, Girder 3

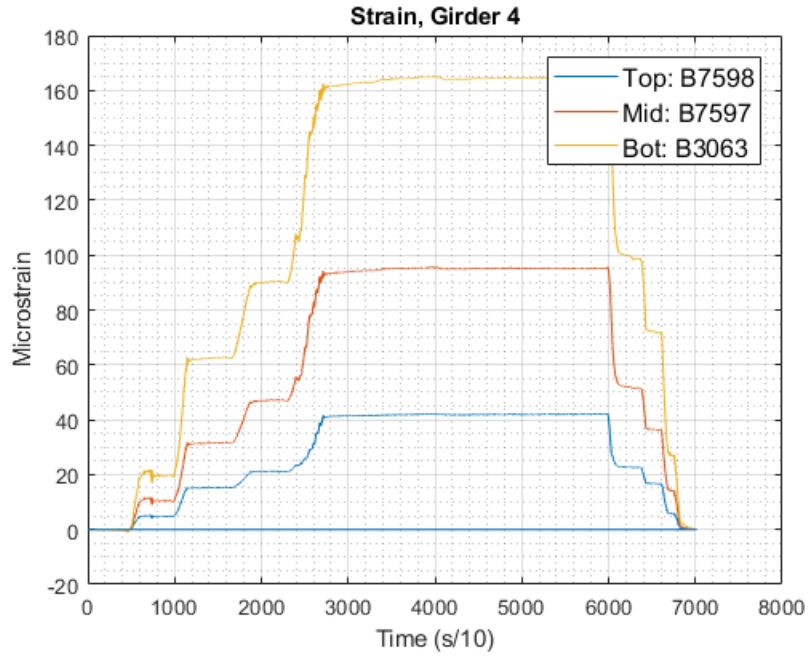


Figure A-55: MAX_3_1 Midspan Strains, Girder 4

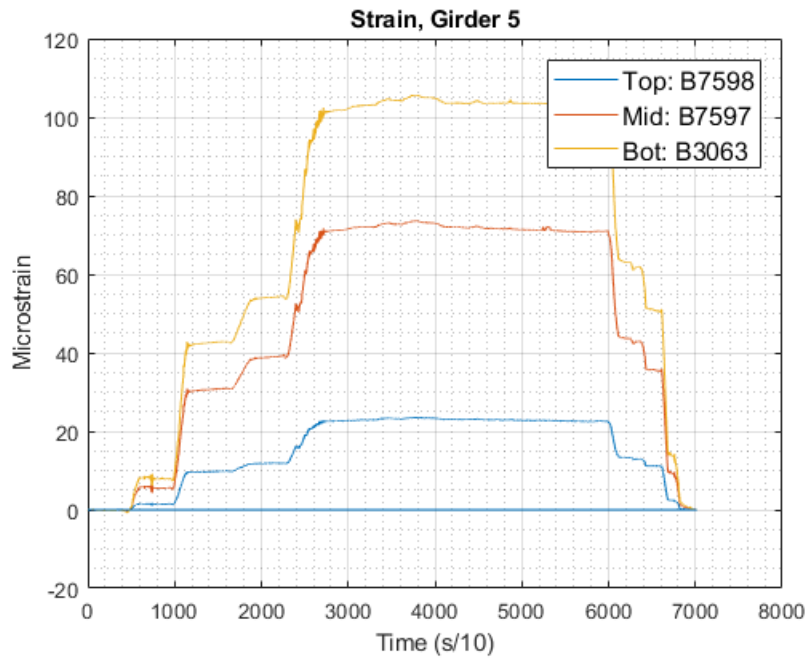


Figure A-56: MAX_3_1 Midspan Strains, Girder 5

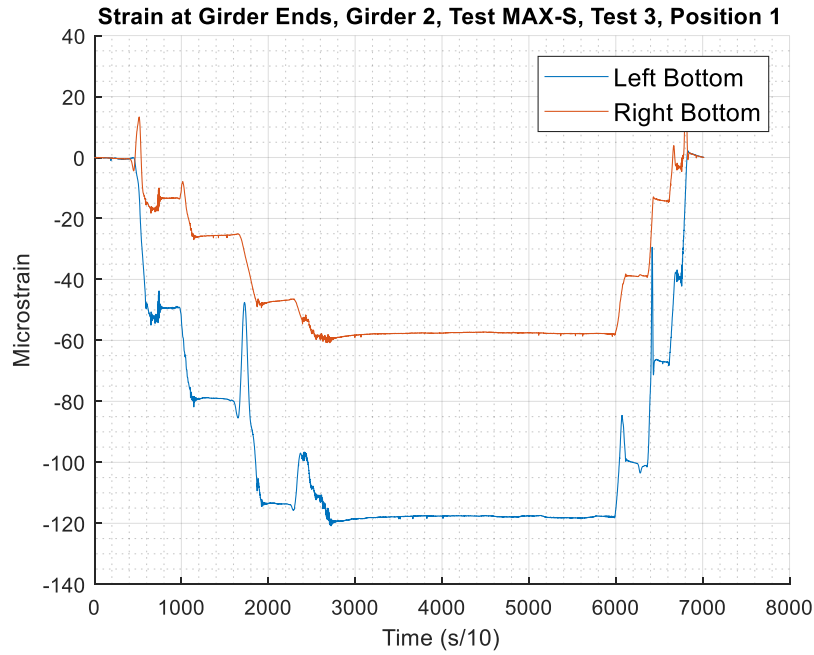


Figure A-57: MAX_3_1 Girder 2 End Strains

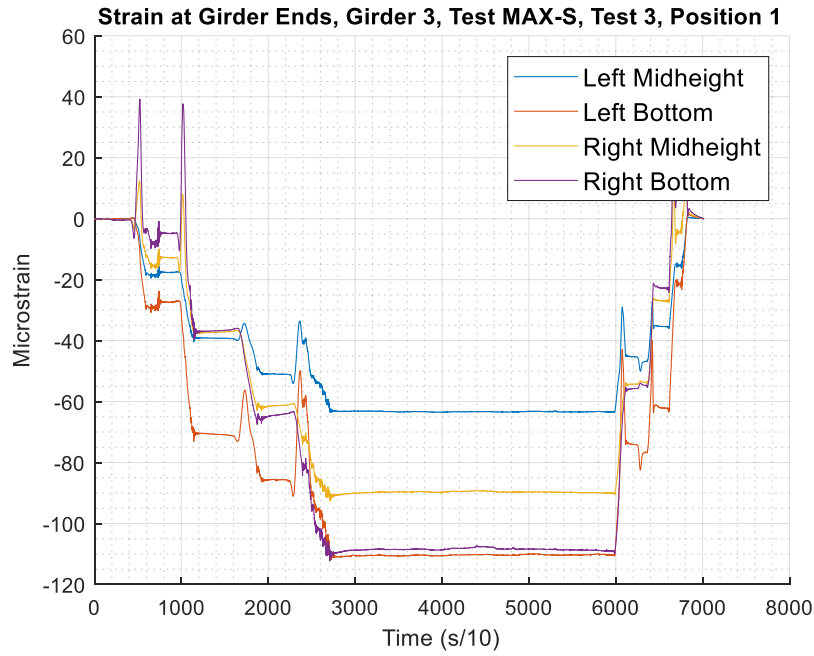


Figure A-58: MAX_3_1 Girder 3 End Strains

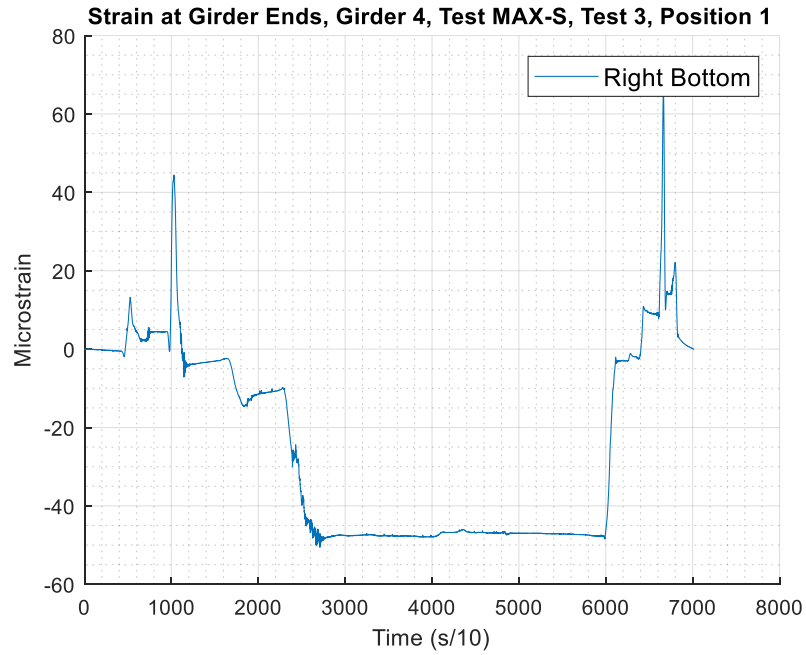


Figure A-59: MAX_3_1 Girder 4 End Strains

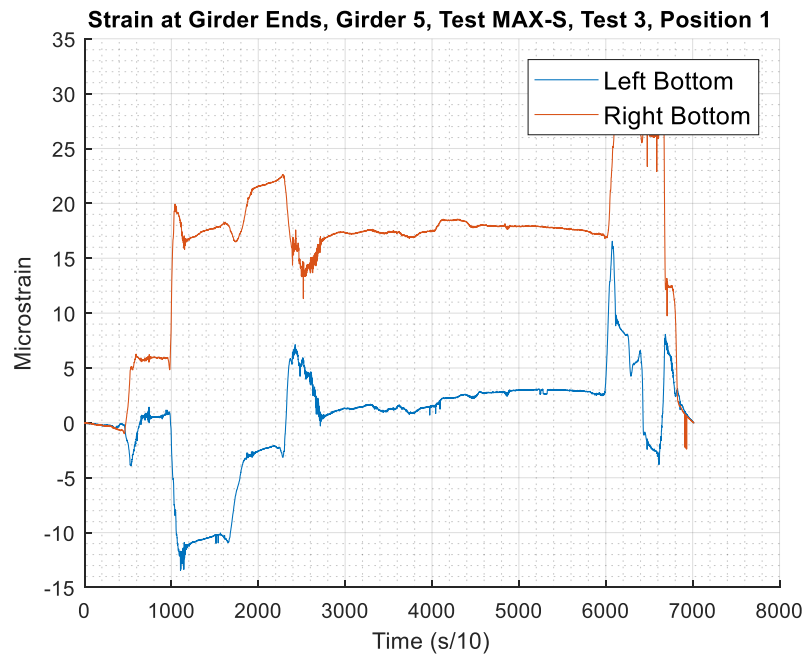


Figure A-60: MAX_3_1 Girder 5 End Strains

A.1.7 ALT_2_1

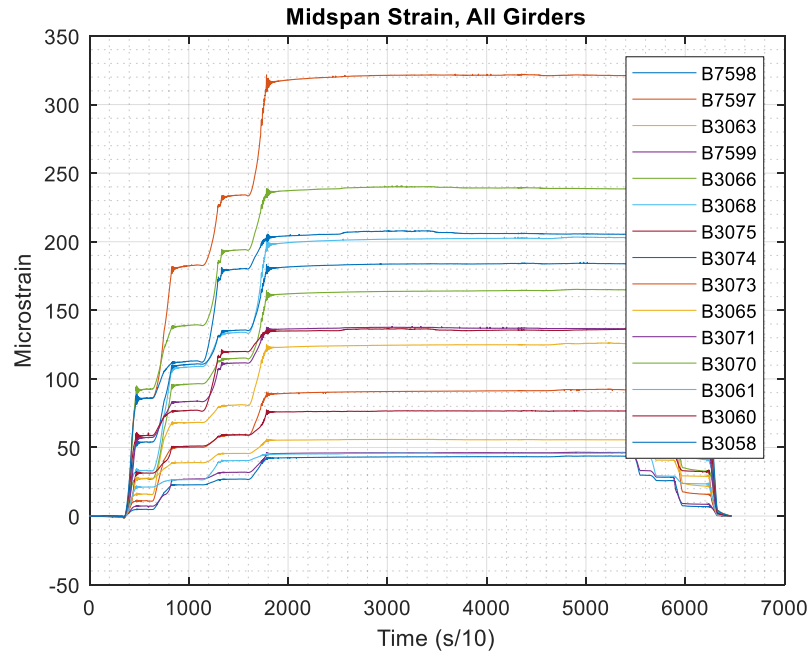


Figure A-61: ALT_2_1 All Midspan Strains

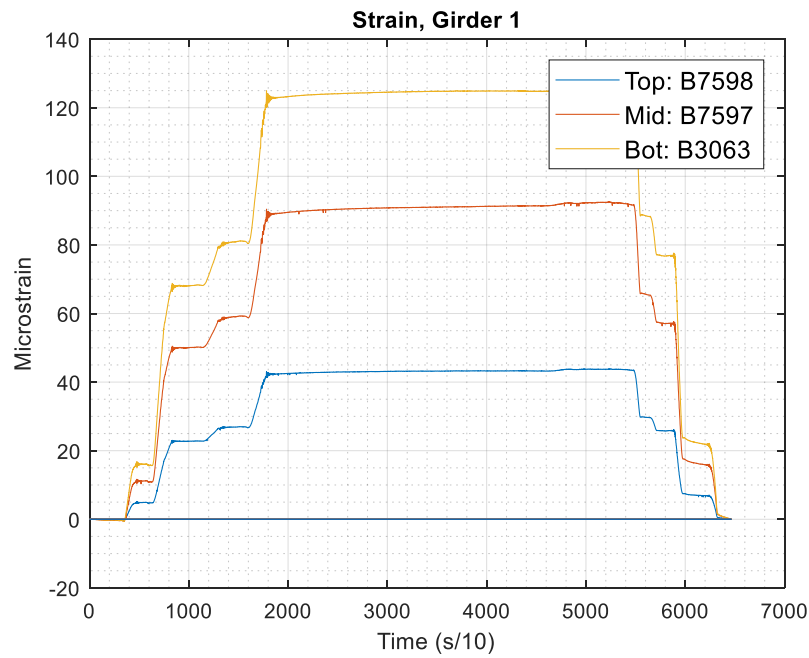


Figure A-62: ALT_2_1 Midspan Strains, Girder 1

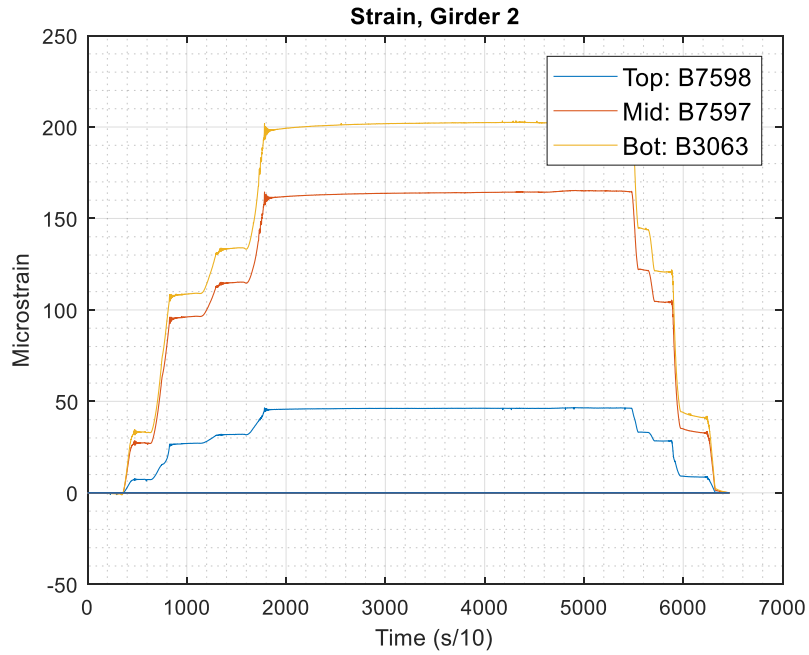


Figure A-63: ALT _2_1 Midspan Strains, Girder 2

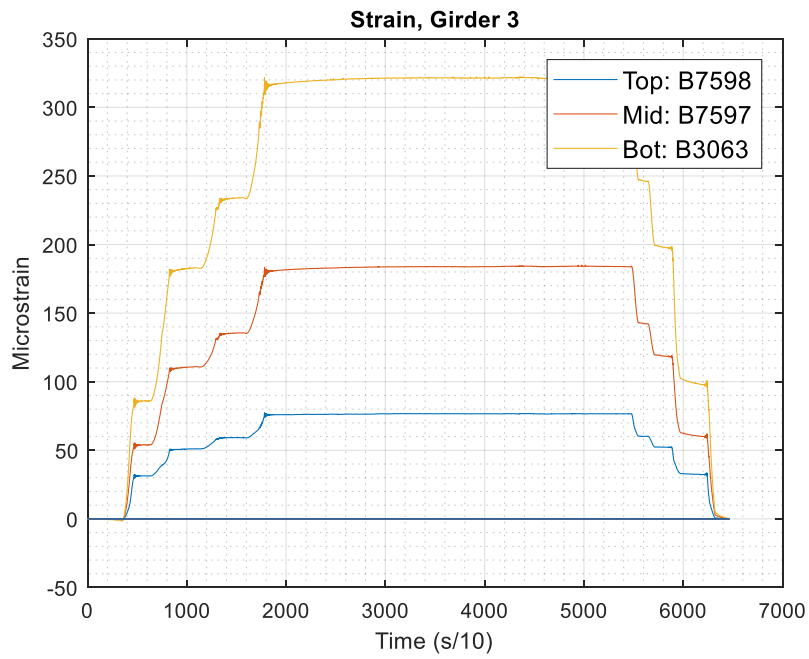


Figure A-64: ALT _2_1 Midspan Strains, Girder 3

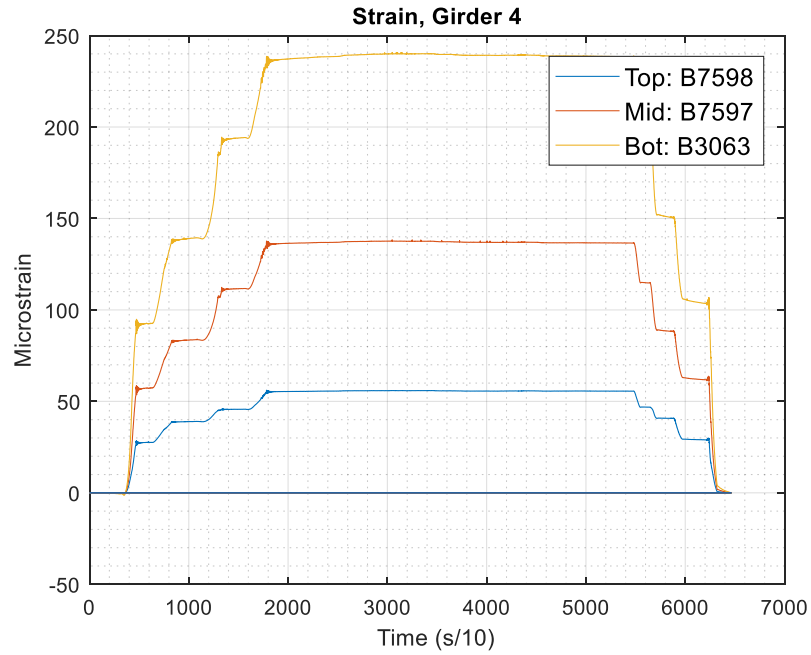


Figure A-65: ALT _2_1 Midspan Strains, Girder 4

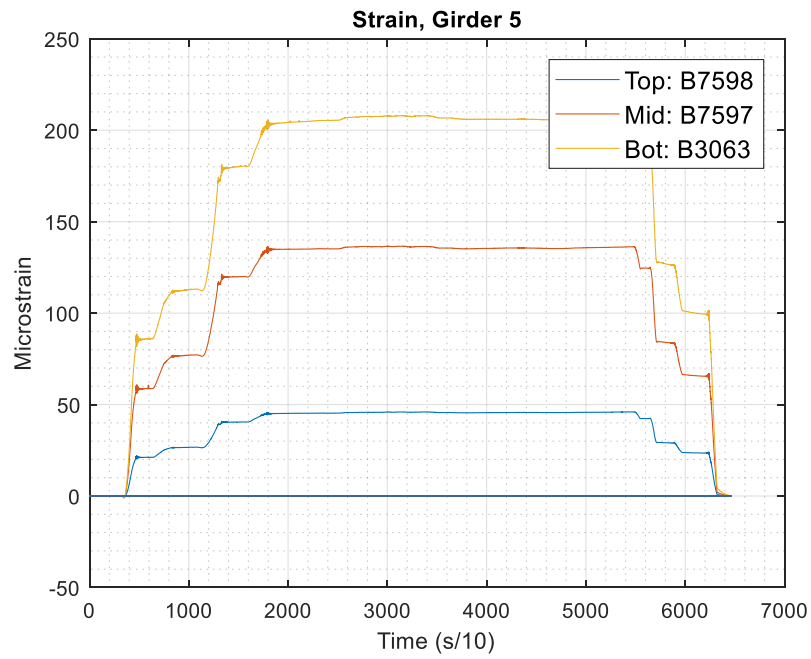


Figure A-66: ALT _2_1 Midspan Strains, Girder 5

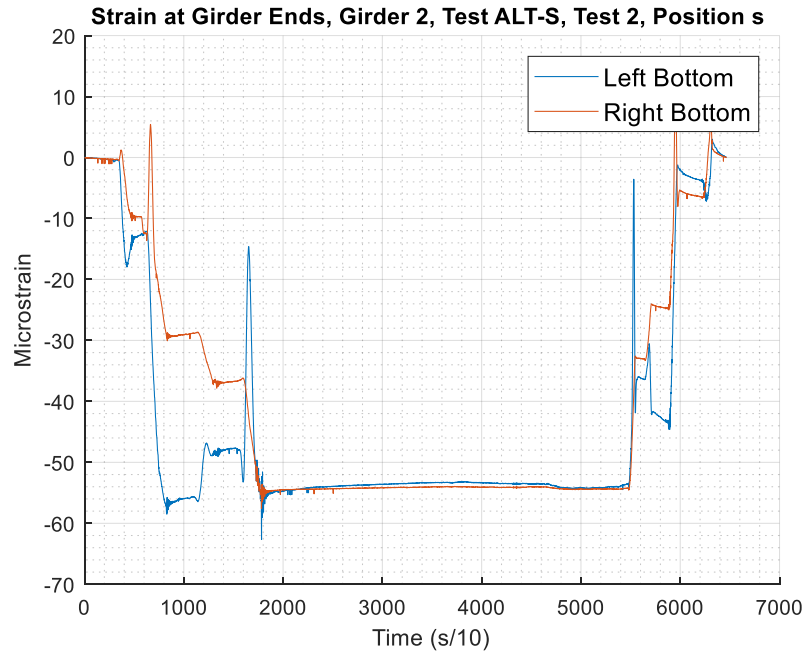


Figure A-67: ALT _2_1 Girder 2 End Strains

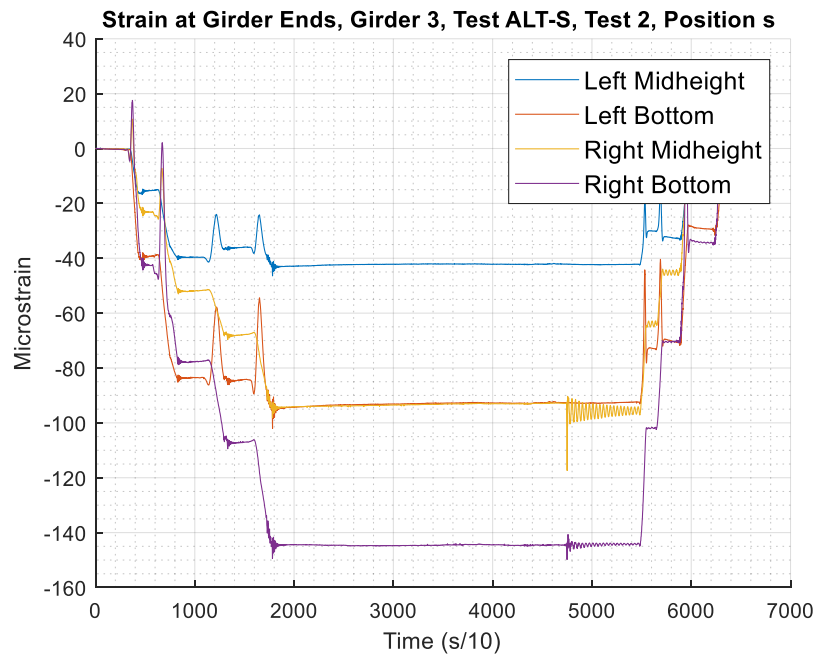


Figure A-68: ALT _2_1 Girder 3 End Strains

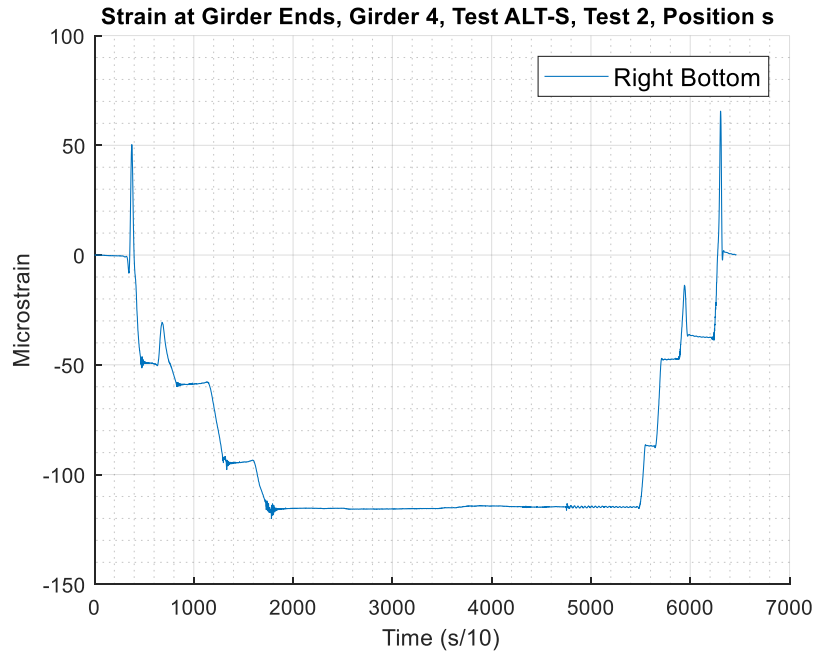


Figure A-69: ALT _2_1 Girder 4 End Strains

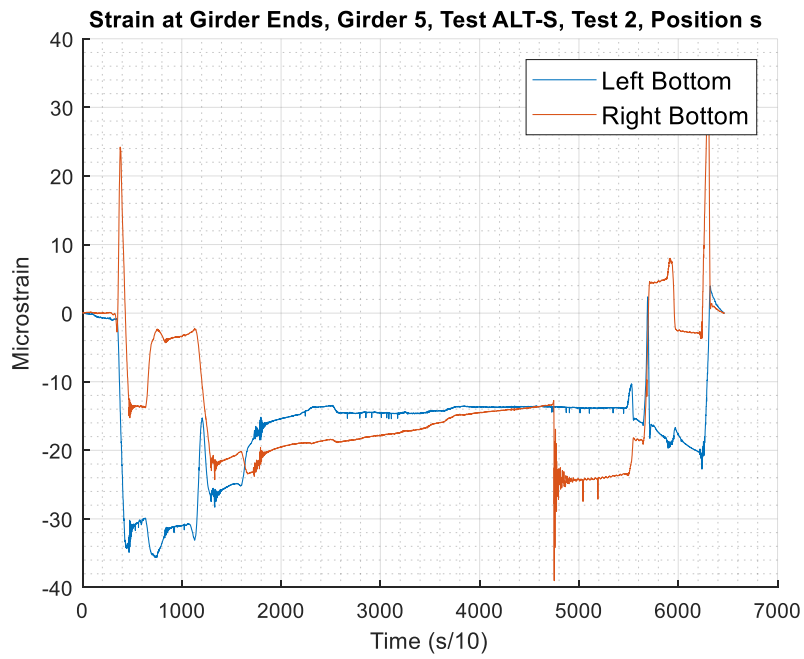


Figure A-70: ALT _2_1 Girder 5 End Strains

A.2 Concrete Cylinder Test Reports from the Hampden Grist Mill Bridge Deck Pour



Report of Concrete Compressive Strength

ASTM C-31/ C-39 / C-1231

Project Name: Hampden ME - Grist Mill Bridge - Concrete Testing

Project Number: 20-1142

Client: T. Buck Construction, Inc.

Report Date: 1/5/2021

General Contractor:

Client Contract Number:

Concrete Supplier: O.J. Folsom

PLACEMENT INFORMATION

Date Cast: 12/8/2020 Time Cast: 12:06 Date Received: 12/9/2020
 Placement Location: BRIDGE DECK

Placement Method: Pump
 Cylinders Made By: Brendan Auth

Placement Vol. (yd³): 115
 Aggregate Size (in): 3/4

INITIAL CURING CONDITIONS

Temperatures

Minimum (°F) 52 Maximum (°F) 66

DELIVERY INFORMATION

Admixtures: AIR / SUPER / 2% NCA

TEST RESULTS

Slump (in) (C-143):
 Air Content (%) (C-231) 8.5
 Air Temp (°F): 31
 Conc. Temp (°F) (C-1064): 60

Load Number: 68 Batch
 Mixer Number: 3 10:43
 Ticket Number 4380 Arrive
 11:30
 Cubic Yards: 10 Depart
 Design (psi): 4000 12:00

Cylinder Designation	Cylinder Weight (lbs)	Cylinder Diameter (in)	Cross Sectional Area(In ²)	Date Of Test	Cure Type	Cap Type	Age (days)	Fracture Type	Load (kips)	Strength (psi)
939-30A	8.00	3.99	12.50	12/15/2020	Lab	Unbonded	7	3	42.6	3410
939-30B	8.08	4.00	12.56	1/5/2021	Lab	Unbonded	28	4	77.0	6130
939-30C	8.03	4.00	12.55	1/5/2021	Lab	Unbonded	28	5	77.4	6170
939-30D	8.04	3.99	12.53	1/5/2021	Lab	Unbonded	28	5	73.7	5880
939-30E		3.99	12.49	12/10/2020	Field	Unbonded	2	5	20.8	1660
939-30F		3.99	12.50	12/10/2020	Field	Unbonded	2	5	21.3	1700
939-30G		3.99	12.51	12/10/2020	Field	Unbonded	2	4	32.2	2570
939-30H				Hold	Field					
939-30I				Hold	Field					

Fracture Types



Remarks:

Chris Ryan

Reviewed By

37 Liberty Drive, Bangor, ME 04401-5874 • Tel (207) 848-6029 • Fax (207) 848-2403 • www.swcole.com



Report of Concrete Compressive Strength

ASTM C-31/ C-39 / C-1231

Project Name: Hampden ME - Grist Mill Bridge - Concrete Testing

Project Number: 20-1142

Client: T. Buck Construction, Inc.

Report Date: 1/5/2021

General Contractor:

Client Contract Number:

Concrete Supplier: O.J. Folsom

PLACEMENT INFORMATION

Date Cast: 12/8/2020 Time Cast: 12:06 Date Received: 12/9/2020

Placement Location: BRIDGE DECK

Placement Method: Pump

Placement Vol. (yd³): 115

Cylinders Made By: Brendan Auth

Aggregate Size (in): 3/4

INITIAL CURING CONDITIONS

Temperatures

Minimum (°F) 52 Maximum (°F) 66

DELIVERY INFORMATION

Admixtures: AIR / SUPER / 2% NCA

TEST RESULTS

Slump (in) (C-143):

Load Number: 68 Batch

Air Content (%) (C-231) 8.5

Mixer Number: 3 10:43

Air Temp (°F): 31

Ticket Number 4380 Arrive

Conc. Temp (°F) (C-1064): 60

Cubic Yards: 10 Depart

Design (psi): 4000 12:00

Cylinder Designation	Cylinder Weight (lbs)	Cylinder Diameter (in)	Cross Sectional Area(In ²)	Date Of Test	Cure Type	Cap Type	Age (days)	Fracture Type	Load (kips)	Strength (psi)
939-30J				Hold	Field					
939-30K				Hold	Field					

Fracture Types



Remarks:

Reviewed By

37 Liberty Drive, Bangor, ME 04401-5874 • Tel (207) 848-6029 • Fax (207) 848-2403 • www.swcole.com



Report of Concrete Compressive Strength

ASTM C-31/ C-39 / C-1231

Project Name: Hampden ME - Grist Mill Bridge - Concrete Testing

Project Number: 20-1142

Client: T. Buck Construction, Inc.

Report Date: 1/5/2021

General Contractor:

Client Contract Number:

Concrete Supplier: O.J. Folsom

PLACEMENT INFORMATION

Date Cast: 12/8/2020 Time Cast: 2:30 Date Received: 12/9/2020

Placement Location: BRIDGE DECK

Placement Method: Pump

Placement Vol. (yd³): 115

Cylinders Made By: Brendan Auth

Aggregate Size (in): 3/4

INITIAL CURING CONDITIONS

Temperatures

Minimum (°F) 52 Maximum (°F) 66

DELIVERY INFORMATION

Admixtures: AIR / SUPER / 2% NCA

TEST RESULTS

Slump (in) (C-143): 6 3/4

Load Number: 11 Batch 1:27

Air Content (%) (C-231) 8.6

Mixer Number: 80 Arrive 2:06

Air Temp (°F): 31

Ticket Number 4397 Depart 2:30

Conc. Temp (°F) (C-1064): 61

Cubic Yards: 10 Design (psi): 4000

Cylinder Designation	Cylinder Weight (lbs)	Cylinder Diameter (in)	Cross Sectional Area(In) ²	Date Of Test	Cure Type	Cap Type	Age (days)	Fracture Type	Load (kips)	Strength (psi)
939-31A	8.15	3.99	12.48	12/15/2020	Lab	Unbonded	7	3	49.5	3970
939-31B	8.11	3.99	12.50	1/5/2021	Lab	Unbonded	28	4	87.4	6990
939-31C	8.14	3.99	12.52	1/5/2021	Lab	Unbonded	28	3	86.3	6900
939-31D	8.17	4.00	12.53	1/5/2021	Lab	Unbonded	28	5	98.3	7840
939-31E		3.98	12.47	12/11/2020	Field	Unbonded	3	4	38.8	3110
939-31F	8.07	3.99	12.49	12/14/2020	Lab	Unbonded	6		65.8	5270
939-31G				Hold	Lab					
939-31H				Hold	Lab					
939-31I				Hold	Lab					

Fracture Types



Remarks:

Chris Ryan

Reviewed By

37 Liberty Drive, Bangor, ME 04401-5874 • Tel (207) 848-6029 • Fax (207) 848-2403 • www.swcole.com



Report of Concrete Compressive Strength

ASTM C-31/ C-39 / C-1231

Project Name: Hampden ME - Grist Mill Bridge - Concrete Testing

Project Number: 20-1142

Client: T. Buck Construction, Inc.

Report Date: 1/5/2021

General Contractor:

Client Contract Number:

Concrete Supplier: O.J. Folsom

PLACEMENT INFORMATION

Date Cast: 12/8/2020 Time Cast: 2:30 Date Received: 12/9/2020
 Placement Location: BRIDGE DECK

Placement Method: Pump
 Cylinders Made By: Brendan Auth

Placement Vol. (yd³): 115
 Aggregate Size (in): 3/4

INITIAL CURING CONDITIONS

Temperatures

Minimum (°F) 52 Maximum (°F) 66

DELIVERY INFORMATION

Admixtures: AIR / SUPER / 2% NCA

TEST RESULTS

Slump (in) (C-143): 6 3/4
 Air Content (%) (C-231) 8.6
 Air Temp (°F): 31
 Conc. Temp (°F) (C-1064): 61

Load Number: 11 Batch 1:27
 Mixer Number: 80
 Ticket Number 4397 Arrive 2:06
 Cubic Yards: 10 Depart 2:30
 Design (psi): 4000

Cylinder Designation	Cylinder Weight (lbs)	Cylinder Diameter (in)	Cross Sectional Area(In ²)	Date Of Test	Cure Type	Cap Type	Age (days)	Fracture Type	Load (kips)	Strength (psi)
939-31J				Hold	Lab					
939-31K				Hold	Lab					

Fracture Types



Remarks:

Reviewed By _____

37 Liberty Drive, Bangor, ME 04401-5874 • Tel (207) 848-6029 • Fax (207) 848-2403 • www.swcole.com